This is to certify that the

dissertation entitled

Anodic Oxidation of Silicon In A Microwave Plasma Disk Reactor

presented by

Thaddeus Adam Roppel

has been accepted towards fulfillment
of the requirements for

Ph.D degree in Electrical Engineering

D. K. Reinhard
Major professor

Date Sept 10, 1986

ANODIC OXIDATION OF SILICON IN A MICROWAVE PLASMA DISK REACTOR

By

Thaddeus Adam Roppel

A DISSERTATION

Submitted to
Michigan State University
in partial fulfillment of the requirements
for the degree of

DOCTOR OF PHILOSOPHY

Department of Electrical Engineering and Systems Science

1986

ABSTRACT

ANODIC OXIDATION OF SILICON IN A MICROWAVE PLASMA DISK REACTOR

By

Thaddeus Adam Roppel

The growth of SiO_2 films on dc-biased Si substrates is investigated in a microwave plasma disk reactor (MPDR). Oxygen pressure in the reactor is varied in the range from 30 to 150 mTorr, microwave input power to the discharge is varied in the range from 80 to 140 W (f = 2.45 GHz, TE_{211} cavity mode), and anodization voltage is varied from 18 to 50 V. The oxide growth rate increases with anodization voltage, and exhibits a peak at approximately 70 mTorr oxygen pressure. The parabolic growth rate constant is found to be in the range from 4.2×10^3 $Å^2$/min to 8.1×10^4 $Å^2$/min for the range of parameters studied, which is comparable to the rates obtained in conventional thermal oxidation at temperatures in excess of 1000 ^oC. However, in the experiments reported here, the substrate temperature is estimated to be less than 300 ^oC for all the conditions studied, offering the possibility for substantial improvements in VLSI integrated circuits processing. In addition, the oxidation technology studied here is a vacuum process, and is therefore compatible with many other vacuum processes already in use or being developed for VLSI fabrication.

The electrical characteristics of the MPDR-grown oxide films are studied by making high-frequency capacitance-voltage (C-V) measurements and I-V measurements on aluminum-gate MOS test capacitors. MOS C-V measurements on plasma oxide samples annealed in forming gas (5% H_2, 95% N_2, 1 h) yield oxide fixed charge densities of 1×10^{11} cm^{-2} and minimum mid-gap interface trap densities of about 2×10^{10} $cm^{-2}eV^{-1}$. These values of Q_f and D_{it} are comparable to state-of-the-art thermal oxides.

A histogram of the dc breakdown fields measured on MPDR-grown oxide samples after annealing in forming gas has a peak in the range of 6 - 8 MV/cm, which is the same as typically measured for good quality thermal oxides.

Oxidation in the MPDR is modeled using a high-field discrete hopping model. This relatively simple model successfully predicts qualitatively the dependence of oxide thickness, anodization current, oxide voltage, and oxide electric field upon anodization voltage. Furthermore, the model predicts ranges of values for these quantities that are in good agreement with experimental results.

To Tammy

AND

To Richard and Lola Roppel, who taught me the beauty of knowledge.

ACKNOWLEDGMENTS

The author expresses deep appreciation to his dissertation advisor, Professor D. K. Reinhard, for invaluable direction and unrelenting committment to this project. In addition, Professor Jes Asmussen's constant stream of creative ideas and insights is gratefully acknowledged. Special thanks is due to Professor P. David Fisher as the source of the author's inspiration to take up the field of electrical engineering. Furthermore, the guidance provided by Professor Dennis Nyquist and Professor Thomas Pinnavaia is welcomed.

This work was supported in part by the Michigan State University Division of Engineering Research, and in part by the National Science Foundation Division of Chemical, Biochemical, and Thermal Engineering, under Grant Number CBT 8413596.

TABLE OF CONTENTS

LIST OF TABLES

LIST OF FIGURES

Chapter One

Introduction

1.1 Statement of the Problem

The processing of silicon has taken on great technological importance during the last several decades, owing to the nearly exclusive use of single-crystal silicon wafers as substrates in conventional integrated circuit fabrication.

One of the most important steps in integrated circuit fabrication is the formation of insulating films, which are used for transistor gate dielectrics, device isolation (both lateral and vertical), masking for diffusion and ion implantation, and passivation. On silicon substrates, insulating layers are readily formed by growing or depositing an amorphous layer of the native oxide, silicon dioxide (SiO_2). Silicon dioxide has high resistivity (10^{14} - 10^{16} Ω-cm), good interface characteristics with the Si crystal lattice, high dielectric strength (the breakdown field is

typically considerably greater than 10^6 MV/cm), and exhibits long term stability and resistance to devitrification.

The conventional technology for formation of SiO_2 films on Si substrates has been thermal oxidation, in which silicon wafers are selectively masked, if required, and then placed in an oxidation furnace at temperatures in the range from 900 ^oC to 1200 ^oC in a dry oxygen or steam ambient. SiO_2 films grown in this way have excellent properties for electronic device applications, due in large part to the many refinements of the technology which have occurred since its inception.

However, as integrated circuit devices become smaller (while, simultaneously, total circuit areas and substrate wafer diameters increase) there is considerable interest in developing fabrication sequences which consist entirely of low temperature processes. One reason for this is to reduce dopant impurity redistribution, which occurs at high temperatures, and places lower limits on critical dimensions of integrated circuit devices. Another high temperature problem is wafer warpage, which becomes a concern when small critical device dimensions are combined with large wafer diameters. A related problem is the thermally activated formation of stacking faults, discussed further in Section 2.5. Still another concern is lateral oxidation, or bird's-beak formation, which is also discussed in Section 2.5.

There are several low temperature oxidation technologies available (these are also described in Chapter Two), but because of the long-term dominance of thermal oxidation and the relatively recent requirement for alternative technologies, none of these has been refined enough to be considered as a substitute for thermal

oxidation in commercial integrated circuit fabrication. A likely scenario for the near future is that one or more of the available low temperature oxidation technologies will take up importance alongside thermal oxidation, and each will have its own niche of applicability in the overall fabrication sequence.

The study reported in this dissertation was undertaken to investigate a particular nonthermal oxidation technology: anodic oxidation in an oxygen microwave discharge. This study was intended to further the general understanding of plasma anodic oxidation of silicon, as well as to investigate the use of the recently developed microwave plasma disk reactor (MPDR) as a research tool. (The MPDR is described in Chapter Three.)

Specific goals for this study included observing the growth of SiO_2 films under well-defined experimental conditions, and investigating the effects of varying experimental parameters such as anodization voltage, discharge pressure, and microwave input power on oxide formation in the MPDR. An additional goal was to measure those characteristics of the oxide films which are important for electronic device applications. The final goal was to further the understanding of plasma oxidation kinetics by developing and testing a model of oxide growth in the MPDR.

1.2 Overview of the Experimental Work Reported in this Dissertation

In order to meet the specific goals stated above, several types of experiments were carried out. The bulk of the experimental work involved a set of oxidation experiments conducted using the MPDR. In

the oxidation experiments, oxide films were grown on silicon substrates under various conditions, and the oxide growth rate and oxide uniformity were correlated with experimental conditions. These experiments are reported in Chapter Four.

Also reported in Chapter Four are the results of two sets of experiments conducted using plasma probes to characterize oxygen discharges in the MPDR. A double Langmuir probe was employed in one set, while in the other set a large-area gold-coated (gilded) silicon probe was used.

Finally, characterization of the plasma-grown oxide films was accomplished by fabricating metal-oxide-semiconductor (MOS) test devices on the samples, and conducting standard tests to evaluate the properties of the bulk oxide and the oxide-silicon interface. The results of these tests are reported in Chapter Five.

1.3 Organization of this Dissertation

This dissertation is organized into seven chapters and one appendix.

A background and literature review are provided in Chapter Two. The emphasis is on plasma oxidation, but thermal oxidation, fundamental silicon chemistry, oxide characterization, and modeling are also discussed.

Chapter Three describes the MPDR and some of its applications, as well as the other experimental apparatus used in the oxidation studies. The experimental procedure for the oxidation experiments is

briefly described, although the bulk of this material is placed in the Appendix.

In Chapter Four, the results of the oxidation experiments are presented, as well as the results from two types of plasma probe experiments.

Oxide characterization results are included in Chapter Five. These include visual and microscopic observations of the oxide samples, and capacitance-voltage and current-voltage measurements on test devices fabricated on the plasma-grown oxides.

A model of plasma oxidation kinetics is investigated in Chapter Six, and the results are compared with the experimental oxidation data from Chapter Four.

Chapter Seven includes a summary, conclusions, and recommendations for future work.

The Appendix includes details of the experimental work which are not necessary for an appreciation of the results, but may be useful to other investigators in this area.

Chapter Two

Background and Review of the Literature

2.1 Introduction

The material in this chapter is intended to provide an overview of the topic of the oxidation of silicon, with emphasis given to applications in integrated circuit fabrication. A brief review of current silicon oxidation technology is provided in Section 2.2, followed by a summary of some fundamental concepts concerning the chemistry of silicon oxidation in Section 2.3. Characterization of oxide films is discussed in Section 2.4, and notation related to the silicon energy band structure and defect density is introduced. In addition, metal-oxide-semiconductor (MOS) capacitance-voltage (C-V) measurements are discussed. In Section 2.5, especially significant papers from the literature in the field of thermal oxidation are reviewed. This section is included in the background for two reasons. First, as the dominant oxidation technology in integrated circuit fabrication, thermal oxidation is the benchmark

against which any new form of oxidation must be compared. Secondly, many of the concepts that arise from a consideration of thermal oxidation are also important to plasma oxidation.

In Section 2.6 the literature in the field of plasma oxidation of silicon is reviewed; this forms the core of the literature review for the topic of this dissertation.

In Section 2.7, several models from the literature on anodic film formation are described; the emphasis is on providing a background for the modeling of plasma oxidation kinetics reported in Chapter Six.

2.2 Overview of Current Oxidation Technology [1,2]

The methods available for forming oxide films on silicon substrates include thermal oxidation, chemical vapor deposition (CVD), high pressure oxidation, liquid electrolytic anodization, and plasma anodization. The first two methods are widely used at present in commercial integrated circuit fabrication. Requirements for the quality of oxide films vary with the application, but in general it is desirable to form films which are stoichiometric, not excessively strained, and for which the interface with the underlying Si substrate has a low defect concentration. Other important requirements include freedom from mobile impurity contamination and low bulk defect concentration. These requirements are dictated by device design constraints (e.g., MOS field effect transistor (MOSFET) threshold voltage uniformity and low junction leakage currents for

bipolar junction transistors (BJT's)), which become more severe as devices are made smaller.

The most demanding application for oxidation is the formation of MOSFET gate oxides. For this purpose, thermal oxidation in dry O_2 is currently the only commonly used technique. Gate oxides are grown at 1100-1200 ^{o}C, and thicknesses range from 1000 Å to 100 Å; the latter value is state-of-the-art for VLSI processing. At the lower end of this range, it is difficult to control the growth process to produce uniformly thick oxide films. Techniques which have been investigated as alternatives to dry oxidation for forming gate oxides include rapid thermal oxidation (RTO) [3], in which the output of a high intensity quartz lamp is directed at a substrate for a carefully controlled duration, and laser-enhanced oxidation [4,5], in which a substrate is oxidized by localized heating with a laser beam. For non-gate oxides, thicker oxides layers are required and interface properties are less crucial. In these cases, thermal oxidation in steam is often used since the oxidation rate in steam is much greater than in dry oxygen. For example, growth of a 1.0 μm oxide layer at 1100 ^{o}C requires 2.2 h in steam, compared with 40 h in dry O_2.

Although thermal oxidation techniques are widely used in present integrated circuit fabrication processes, there are several problems associated with thermal oxidation which become increasingly limiting as device dimensions are scaled down. One of these is the so-called bird's beak effect [6], described as follows. In some applications, it is necessary to oxidize a substrate only in selected areas. Selective thermal oxidation is often conducted by depositing Si_3N_4 on a substrate as a mask layer, patterning the mask layer using plasma etching or wet etching, and then thermally oxidizing through the

patterned mask. However, because the growing oxide partially consumes the substrate, lateral oxidation occurs under the mask layer, inducing strain and deforming the mask. The profile of the resulting oxide which forms under the mask edges has the shape of a bird's head and beak, with the beak pointing away from the mask opening. In VLSI integrated circuits with linewidths of 1.0 μm or less, it is possible for bird's beak formation to consume a significant fraction of the usable area on a chip. Techniques have been developed to reduce bird's beak formation during semi-recessed oxidation (SEMIROX) and fully recessed oxidation (FULL ROX), which are used for lateral device isolation, but these techniques require additional processing complexity.

Another disadvantage associated with thermal oxidation is the formation of oxidation-induced stacking faults in the silicon near the oxide interface. Stacking faults are interruptions in the normal sequence of lattice planes in the silicon crystal which can serve as congregation sites for defect clusters. Stacking faults near the surface of a silicon substrate result in serious device degradation [2].

In addition, at the high temperatures used in thermal oxidation, redistribution of the substrate dopant profile occurs, which complicates the design of a fabrication process. Furthermore, any high temperature process induces mechanical stress in a substrate wafer, which can cause the wafer to warp. Both of these problems become more pronounced as device dimensions become smaller.

Despite the problems previously described, thermal oxidation is currently the mainstay in IC fabrication. However, formation of

oxide layers by CVD is also an important part of IC technology. Chemical vapor deposition of SiO_2 is possible from silane (SiH_4) at low temperatures (300-500 ^{o}C), or from tetraethylorthosilicate $(C_2H_5O)_4Si$ at higher temperatures (500-850 ^{o}C). CVD results in poorer interface properties than thermal oxidation, so it is not used for gate oxides, but it offers several advantages. Because the oxide is deposited, instead of grown, any material can be covered; this is particularly useful for masking and passivation applications. In addition, the substrate is not consumed, and dopant impurity redistribution is reduced compared with thermal oxidation.

Oxidation in high pressure oxygen or steam at reduced temperature (10 - 60 atm at 700 - 800 ^{o}C) has found some use in integrated circuit fabrication, because the oxidation rate increases approximately proportionally to pressure in the usual range of interest. For example, field oxides for integrated circuits (used to vertically separate metal interconnecting lines from underlying devices, thereby minimizing electric field interactions) are sometimes required to be more than one micrometer thick. Growth of the field oxide is the longest single step in integrated circuit fabrication, and, in addition, thermal oxides thicker than about 1 μm tend to crack and devitrify. High pressure steam oxidation has been used to alleviate these problems. An additional advantage resulting from the lower temperature is reduced impurity redistribution.

Liquid anodization is a room temperature process in which the silicon substrate is made the anode of an electrolytic cell. An oxide layer forms as current passes through the cell, carrying an oxidizing species through the existing oxide to the reaction interface. Interface properties can be made comparable to thermal

oxides by annealing. However, a serious drawback is that mobile ionic contamination is much higher in the best liquid anodic process than in the best thermal process. Consequently, this process is not presently used in conventional integrated circuit fabrication.

Plasma anodization is a low temperature, vacuum process. It is similar in concept to liquid electrolytic anodization, but the liquid electrolyte is replaced with ionized oxygen at low pressure. Oxidation rates comparable to steam thermal oxidation can be obtained with substrate temperatures below 600 ^{o}C. Plasma oxidation is not now used in standard integrated circuit fabrication processes. It has garnered considerable interest, however, as a VLSI oxidation technique since it is a nonthermal process. Plasma oxidation of silicon is the central topic of this dissertation, and the relevant literature is reviewed in Section 2.6.

For most oxidation techniques, some sort of annealing process is usually used after oxidation to improve the oxide and interface properties. The optimal choice of annealing time, temperature, and ambient gases are determined empirically for each process, as the underlying mechanisms are not well understood at present. The two principal types of annealing in use are referred to as post-metallization and post-oxidation annealing. In post-metallization annealing, an aluminum layer is evaporated on the oxide, and the oxide is annealed at about 400 ^{o}C in an ambient containing hydrogen. If the fabrication process does not call for aluminum evaporation following oxidation, high temperature post-oxidation annealing can be used, in which the oxide is exposed to hydrogen or an inert gas for about 30 min at 900 - 1000 ^{o}C. The quantitative effects of annealing are discussed in Section 2.4.

2.3 Oxidation of Silicon: Basic Processes

Fundamentally, the oxidation of crystalline silicon involves the breaking of existing Si-Si bonds and the formation of Si-O bonds. The activation energy for breaking a Si-Si bond is 1.83 eV. The Si-O bond is mainly covalent and therefore exhibits directionality. In SiO_2, the basic structural unit consists of a Si ion surrounded by four O ions to form a regular tetrahedron. In this structure, the Si-O bond length is 1.6 Å and the O-O intranuclear distance is 2.27 Å. The various phases of SiO_2 are formed as these tetrahedra are joined by oxygen bridges. SiO_2 has a number of crystalline phases, including quartz, and an amorphous (noncrystalline, or vitreous, or glassy) phase. It is the amorphous phase which forms during thermal oxidation, and X-ray diffraction studies have indicated that this is the case for plasma oxidation as well [7]. A number of defect types are known to occur in noncrystalline SiO_2 [8]. The presence of water in the oxidation ambient leads to reduction of the silicon by hydrogen, resulting in broken oxygen bridges and trivalent silicon. The presence of interstitial oxygen or oxygen ions is necessary for oxidation to progress, but it is a defect from the standpoint of lattice order. Trivalent Si acts as an electron donor in the oxide, giving up an electron to the conduction band, and interstitial O acts as an acceptor. Other defects include the presence of bridging oxygen vacancies, non-bridging oxygen, and univalent anions (e.g., OH^-) in the position of non-bridging oxygen.

The reactions by which the oxidation of silicon is usually described are

$$Si + O_2 \leftrightarrow SiO_2$$

for oxidation in dry oxygen, and

$$Si + 2H_2O \leftrightarrow SiO_2 + 2H_2$$

for oxidation in water vapor. However, there are numerous possible intermediate reactions which must be considered in order to develop a complete picture of the oxidation process [8,9]. For instance, as proposed in [8], thermal oxidation could progress by the following reactions:

$$\tfrac{1}{2}(O_2) \leftrightarrow (O_i)_{SiO_2} \leftrightarrow (O_i^- + h^+)_{SiO_2}$$

at the SiO_2-O_2 interface, and

$$(2O_i^- + 4h^+)_{SiO_2} + (Si)_{Si} \leftrightarrow SiO_2$$

at the Si-SiO_2 interface. In these equations, O_i is interstitial oxygen, h^+ is a hole, and the subscripts outside the parentheses indicate the phase. Other authors have suggested mechanisms for plasma oxidation which involve electron-ion or electron-neutral reactions at the oxide-plasma interface, leading to the formation of charged species which diffuse to the reaction interface [10-14]. For

both thermal oxidation and plasma oxidation, there is evidence to support the conclusion that Si does not migrate during oxide formation [15,16].

The structure which results from thermally oxidizing a Si substrate is speculated to consist of an interfacial region of single-crystal silicon followed by a nonstoichiometric monolayer of SiO_2, Si_2O_2, and Si_2O; this is followed by a strained region of SiO_2 roughly 10 to 40 Å deep, and this is followed by the remaining strain-free stoichiometric bulk SiO_2 film [2].

2.4 Characterization of SiO_2 Films and Interfaces

2.4.1 Overview

The methods used to characterize silicon dioxide films on silicon substrates can be divided into three broad categories: those which quantify the electronic properties, those which quantify the optical properties (e.g., refractive index and IR absorption measurements), and those which are concerned with physical properties of the system, such as strain, etch rate, and stoichiometry. In this study, the electronic properties are given primary importance. However, these categories are not independent of each other. For example, stress in a silicon substrate arising from the growth of an SiO_2 film on the surface modifies the semiconductor band structure, thereby affecting the conductivity, carrier mobility, and optical properties of the system [17].

One of the most important methods used to investigate the electronic properties of oxide films is the measurement of the electrical characteristics of metal-oxide-semiconductor (MOS) capacitors formed on the films. This topic is discussed in 2.4.2. The oxide property which is most influential in determining device performance is the density of electrically active defects, or traps, at the Si-SiO_2 interface. The measurement of interface state density on MOS devices is addressed in 2.4.3.

2.4.2 Electrical Characteristics of the MOS Capacitor Structure

After an oxide is formed on a semiconductor substrate, MOS capacitors can be formed by coating the oxide with a metallic layer, and then selectively removing the metal to leave contacts of the desired geometry. These contacts are usually referred to as gates, with reference to the FET, in which the gate is an MOS structure.

MOS capacitor measurements can be used to determine nearly all of the properties of interest regarding the oxide layer and its interfaces [2]. These include but are not limited to the following:

1. Oxide thickness
2. Oxide breakdown field
3. Si-SiO_2 interface trap level density as a function of energy in the bandgap
4. Oxide fixed charge density
5. Ionic drift and polarization effects in the oxide

6. Surface band bending and depletion layer width in the silicon as a function of gate bias
7. Dielectric constant of the oxide.

MOS capacitor test device measurements involve capacitance-voltage (C-V) characterization or current-voltage (I-V) characterization, possibly combined with optical and thermal excitation. The emphasis in the current discussion is on room temperature C-V characterization of MOS capacitors formed on the structure Al-SiO_2-(n-Si), without optical excitation. This corresponds to the structure and measuring conditions for the test devices used in this work to characterize the experimental plasma oxide samples. Characterization of the experimental plasma-grown oxides is discussed in Section 5.4. In the present discussion, typical values for important parameters are given based on the use of a thermally grown SiO_2 dielectric layer because of the large amount of data available from the literature for thermal oxides, but the general results are applicable to capacitors formed on either thermal or plasma-grown oxides.

Energy band diagrams for an ideal MOS capacitor subjected to several possible test conditions are shown in Figure 2.1. These will be discussed here with the aim of explaining qualitatively the characteristics of a typical measured C-V curve. In Section 5.4, a more extensive derivation of the MOS C-V characteristics is given.

In Figure 2.1(a), the MOS system is shown in equilibrium, and in this case the system is characterized by a single Fermi energy. In

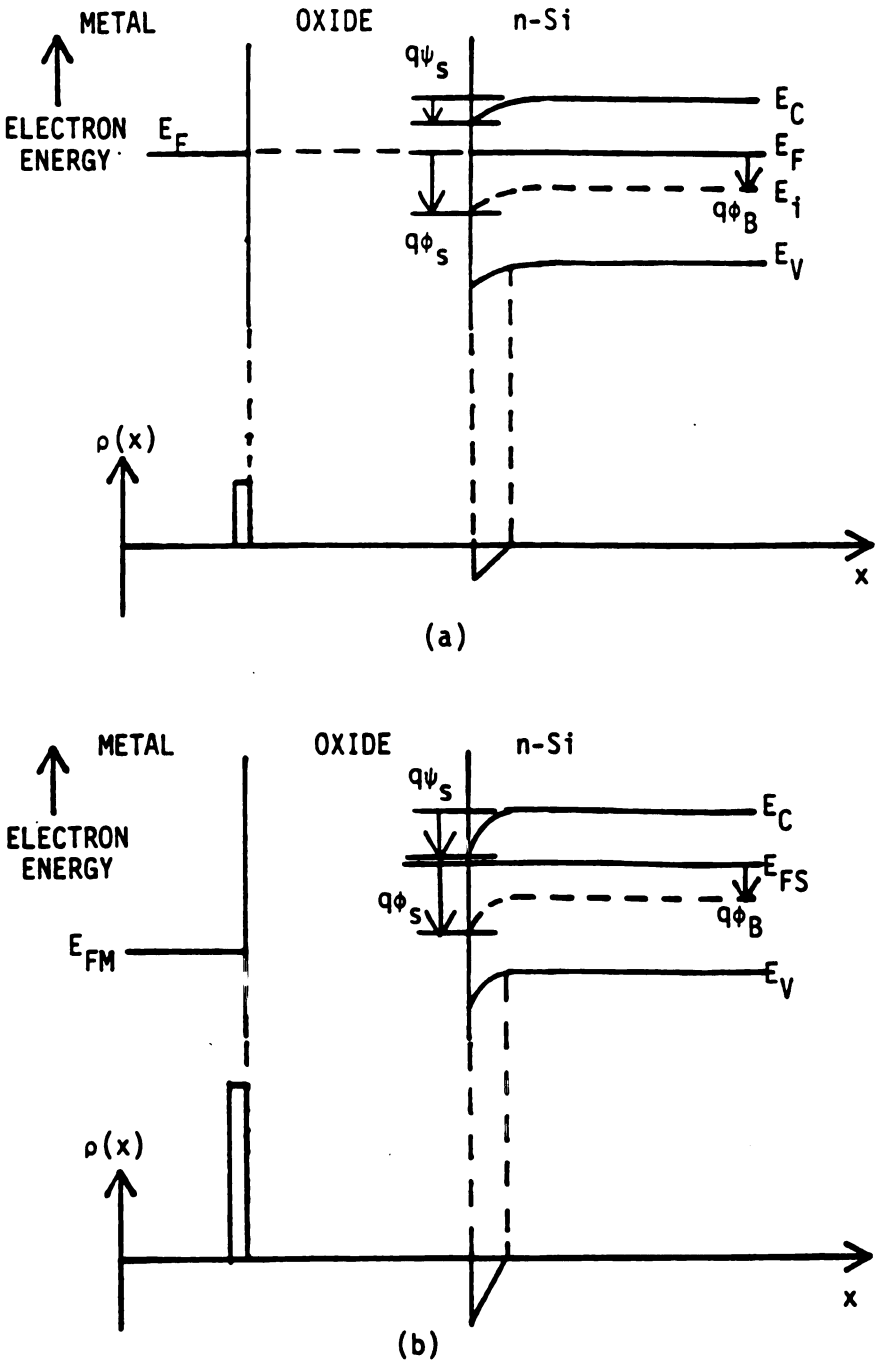

Figure 2.1. Energy band diagrams (arrows pointing down indicate positive values) and charge distribution for an MOS capacitor under various test conditions. (a) Equilibrium ($V_G = 0$). (b) Accumulation ($V_G > V_{FB}$).

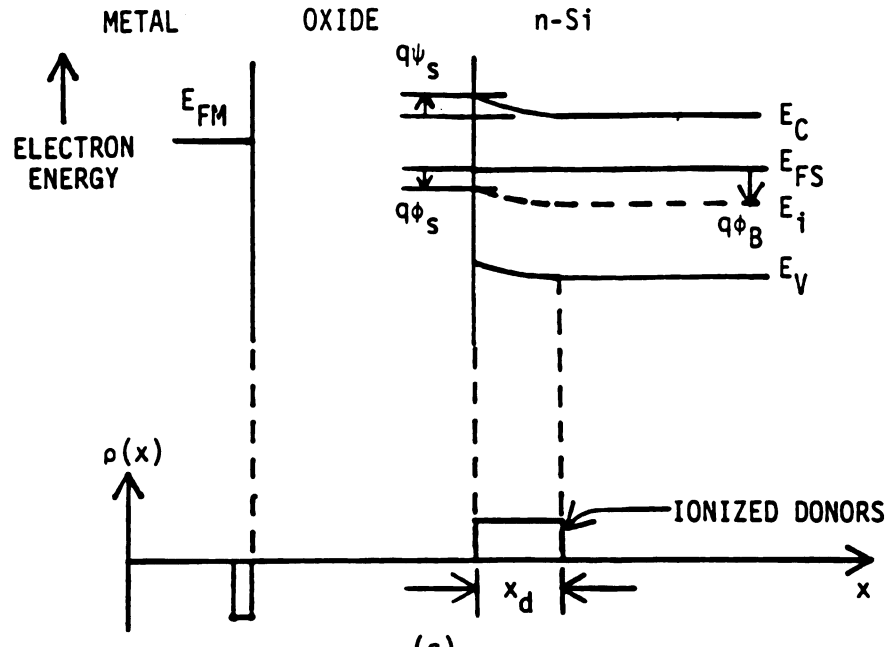

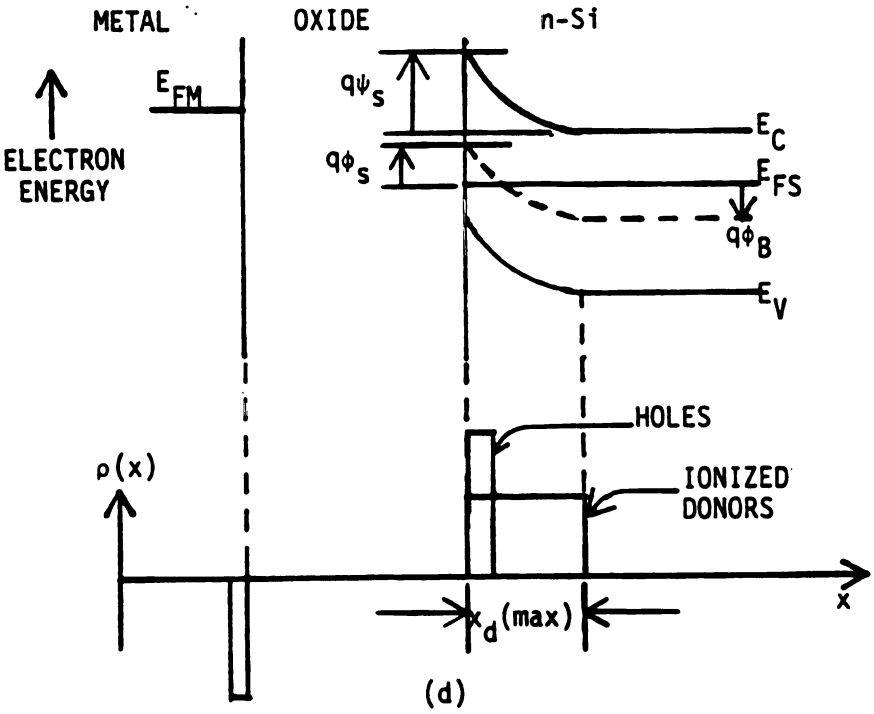

Figure 2.1 (continued). (c) Depletion ($V_T < V_G < V_{FB}$). (d) Strong inversion ($V_G < V_T$, $\phi_s = -\phi_B$).

the bulk n-type Si, the amount by which the Fermi energy is raised above the intrinsic level by the doping is defined as the bulk potential,

$$\phi_B = (k_B T/q)\ \ell n(N_D/n_i) \quad ,$$

where k_B is the Boltzmann constant, T is the absolute temperature of the system, q is the magnitude of the electronic charge, N_D is the number density of donor-type dopant impurity atoms in the silicon, which is assumed here to be constant throughout the silicon, and n_i is the intrinsic carrier concentration in the silicon at temperature T. If N_D is much greater than n_i, then in the intermediate range of temperatures (including room temperature) for which nearly all the donor impurity atoms are ionized, the electron concentration in the bulk, n, is approximately equal to N_D. The hole concentration in the bulk is given by $p = n_i^2/N_D$ under these conditions. The band bending ψ_s at the Si surface is non-zero due to the metal-semiconductor work function difference, ϕ_{MS}. If the metal is Al and the substrate is n-type Si, then

$$-q\psi_s = q\phi_{MS} \approx -0.55 \text{ eV} + k_B T\ \ell n\ \frac{N_D}{n_i} \quad . \qquad [2.1]$$

With $T = 300\ ^{o}K$ and $N_D = 10^{15}\ cm^{-3}$, Equation 2.1 yields $q\phi_{MS} = -0.26$ eV.

The application of an external bias voltage V_G on the metal relative to the substrate results in the non-equilibrium conditions

shown in Figure 2.1(b)-(d). A positive bias on the metal, as shown in (b), drives the Si surface into accumulation. In accumulation, the electron (majority carrier) concentration is increased from its equilibrium value at the Si surface, resulting in a highly conductive layer near the surface capable of responding to an applied gate signal with a time constant approaching the dielectric relaxation time in the Si (roughly 10^{-12} s). The increased electron concentration at the surface is represented by an increase in ψ_s .

If a negative bias is applied to the metal as shown in Figure 2.1(c) and (d), ψ_s is reduced. The gate voltage required to make $\psi_s = 0$ is called the flat-band voltage, denoted V_{FB}.

As V_G is made more negative, the depletion layer width increases, and the Si surface is first driven into depletion and then into inversion. The depletion layer width is given by

$$x_d = \left[\frac{2\epsilon_s|\psi_s|}{qN_D}\right]^{\frac{1}{2}} \qquad [2.2]$$

where ϵ_s is the permittivity of the silicon. In the depletion regime, the density of mobile charge near the Si surface is very low, and a space charge layer exists due to the presence of immobile ionized impurities. When $\psi_s = -\phi_B$, the silicon surface is intrinsic (i.e., since $E_{fs} = E_i$, then $n_s = p_s = n_i$, where n_s and p_s are the surface electron and hole concentrations). The latter condition defines the onset of weak inversion. The onset of strong inversion is defined to occur when $\psi_s = -2\phi_B$. Under this condition, a layer of inversion charge is generated near the surface in the silicon in

which the minority carrier (hole) concentration p_s is equal to the majority carrier concentration in the bulk, which is many orders of magnitude greater than n_s. The value of V_G required to achieve strong inversion is called the threshold voltage, V_T.

In practical C-V measurements, the capacitance of an MOS structure is measured as an externally applied gate voltage is varied. Typical high- and low-frequency C-V curves for n-Si are shown in Figure 2.2. In practice, such curves are generated by using a capacitance bridge provided with the capability of adding a variable dc gate bias to the ac measuring signal.

The general form of these curves is explained in the next several paragraphs. In any bias regime, the total capacitance per unit area C′ is the series combination of the oxide capacitance C'_{ox} and the silicon capacitance, C'_s. (These quantities are written with primes to indicate normalization with respect to gate area.) In accumulation, the silicon capacitance is so large that it can be neglected, and the total capacitance of the system is the oxide capacitance,

$$C'_{ox} = \epsilon_{ox}/x_{ox} \qquad [2.3]$$

where ϵ_{ox} is the permittivity of the oxide, and x_{ox} is the oxide

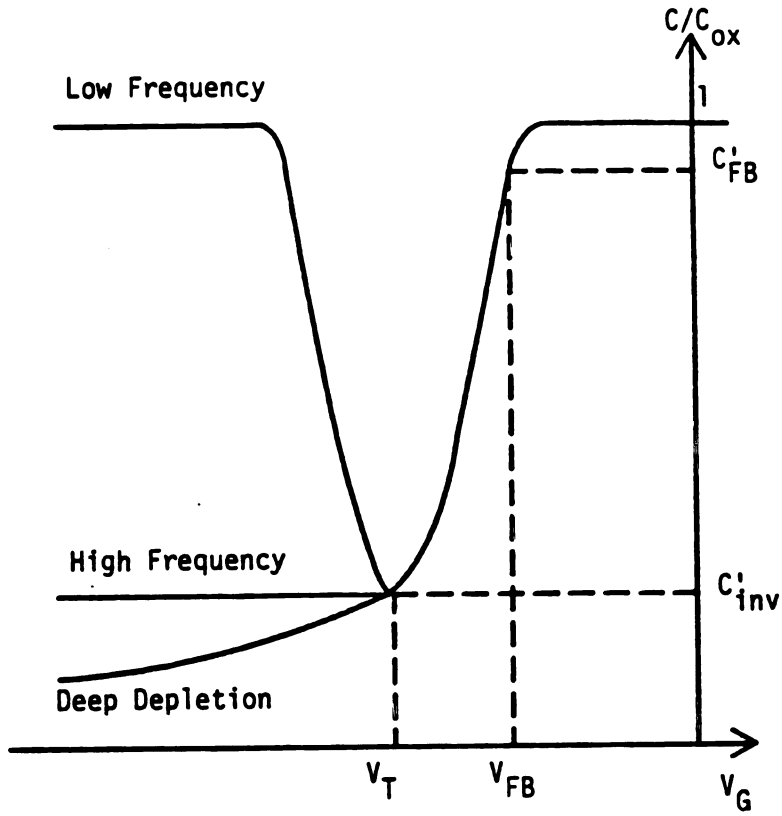

Figure 2.2 Typical high- and low-frequency capacitance-voltage (C-V) curves for MOS capacitors on n-type silicon. The curves are the same in accumulation-depletion, but are differentiated in inversion by minority carrier response.

layer thickness. According to Equation 2.3, the oxide thickness can be determined directly from measurement of the capacitance in accumulation if the oxide permittivity is known.

At the flatband voltage, the silicon capacitance is ϵ_s/L_D where L_D is the extrinsic Debye length, given by

$$L_D = \left[\frac{\epsilon_s k_B T}{q^2 N_D}\right]^{\frac{1}{2}} . \qquad [2.4]$$

In depletion, the silicon capacitance is due to the depletion layer, so that

$$C_s' = \epsilon_s/x_d . \qquad [2.5]$$

In strong inversion the band bending is pinned by the formation of a layer of inversion charge (holes), resulting in a maximum depletion layer width

$$x_{dmax} = \left[\frac{4\epsilon_s \phi_B}{qN_D}\right]^{\frac{1}{2}} . \qquad [2.6]$$

At measuring frequencies high enough to neglect minority carrier response (greater than about 1000 Hz), the capacitance in inversion is

$$C_{inv} = \left[\frac{x_{ox}}{\epsilon_{ox}} + \frac{x_{dmax}}{\epsilon_s}\right]^{-1}. \qquad [2.7]$$

At measuring frequencies low enough for minority carriers to respond (less than about 10 Hz), the capacitance rises quickly to C_{ox} because C_s is shunted by the inversion layer charge. During a high frequency measurement, if the gate bias in inversion is varied rapidly enough so that the minority carriers cannot fully respond, the deep depletion behavior shown in Figure 2.2 results.

The C-V characteristics of practical MOS systems are modified from those described above by the presence of charged defects and mobile charge in the oxide-semiconductor system arising from four sources [18], which are described in the following paragraphs.

(1) Electron and hole energy levels, variously called interface states or traps, or fast states, exist in the Si bandgap at the Si-SiO_2 interface due mainly to the existence of mismatched bonds and the interruption of the silicon lattice. The charge trapped in these states is referred to as interface trapped charge, and is denoted Q_{it}. The energy levels associated with interface traps are distributed throughout the silicon energy gap and the energy density of interface traps, D_{it}, is characteristically minimum near the middle of the gap. The value of Q_{it} and the minimum value of D_{it} are highly dependent upon oxide growth conditions and annealing. Typical values

of D_{it} for as-grown dry thermal oxides on (100)-oriented Si substrates are on the order of 10^{12} $cm^{-2}eV^{-1}$. Annealing by one of the methods mentioned in Section 2.2 reduces D_{it} to about 10^{10} $cm^{-2}eV^{-1}$. For steam thermal oxides, D_{it} can be reduced from as-grown values of about 10^{11} $cm^{-2}eV^{-1}$ to the order of 10^{10} $cm^{-2}eV^{-1}$ after annealing. Interface states are discussed further in Paragraph 2.4.3.

(2) Charge sites occur in the strained SiO_2 region near the interface due to the presence of excess silicon and oxygen (discussed further in Section 2.3). These sites do not exchange charge with the silicon, and are referred to as fixed charged, Q_f. The polarity of the fixed charge is always found to be positive, and the magnitude of Q_f is dependent on growth conditions and annealing. The best values obtained are on the order of $q\times10^{10}$ C/cm^2.

(3) In the bulk oxide, occasional defects give rise to hole and electron traps. Charge trapped in these states is referred to as oxide trapped charge, Q_{ot}. Because of the deep potential wells associated with these localized traps in the oxide, Q_{ot} is usually only significant when sources of energy are available which can liberate charge carriers from these traps, such as during ultraviolet irradiation or under high electric field conditions.

(4) The fourth type of oxide charge, designated ρ_M, is due to mobile ionic contamination. The most prevalent contaminant is Na^+, which is highly mobile in SiO_2 and is easily incorporated from processing chemicals, metal films, and human contact. Other possible ionic contaminants include Li^+ and K^+. These contaminants are not exchanged with the Si or the metal, and they can drift in the oxide under the influence of an applied gate bias, potentially causing inconsistent device behavior.

The presence of oxide charge which is not exchanged with the Si (Q_f, Q_{ot}, ρ_M) causes a modification of the ideal C-V characteristics which can be represented, for slowly varying gate bias, by a simple translation of the C-V curve along the gate-bias axis. This shift, denoted ΔV, is illustrated in Figure 2.3. The amount of the shift may be calculated as follows [18]:

$$\Delta V = \frac{-qQ'_f}{C'_{ox}} - \frac{1}{C'_{ox}} \left\{ \int_0^{x_{ox}} (x/x_{ox})(\rho_{ot}(x) + \rho_M(x))\, dx \right\} . \qquad [2.8]$$

In the expression above, ρ_{ot} is the volume density of oxide trapped charge, and Q'_f is the oxide fixed charge density per unit gate area.

The presence of interface traps requires an additional correction to the C-V curve, which is the addition of a bias-dependent capacitance, C_{it}, calculated from D_{it}. It can be shown that this correction leads to a stretching out of the C-V curve along the gate-bias axis. C-V curve stretchout is illustrated in Figure 2.3. A more detailed discussion of D_{it} and C-V curve stretchout is provided in Section 5.4.

2.4.3 Measurements of Interface Properties

A fundamental property of the Si-SiO_2 system is the existence of charged energy states at the interface. These states are sometimes referred to as fast states, because they can exchange charge (capture and emit holes and electrons) with the semiconductor, with time

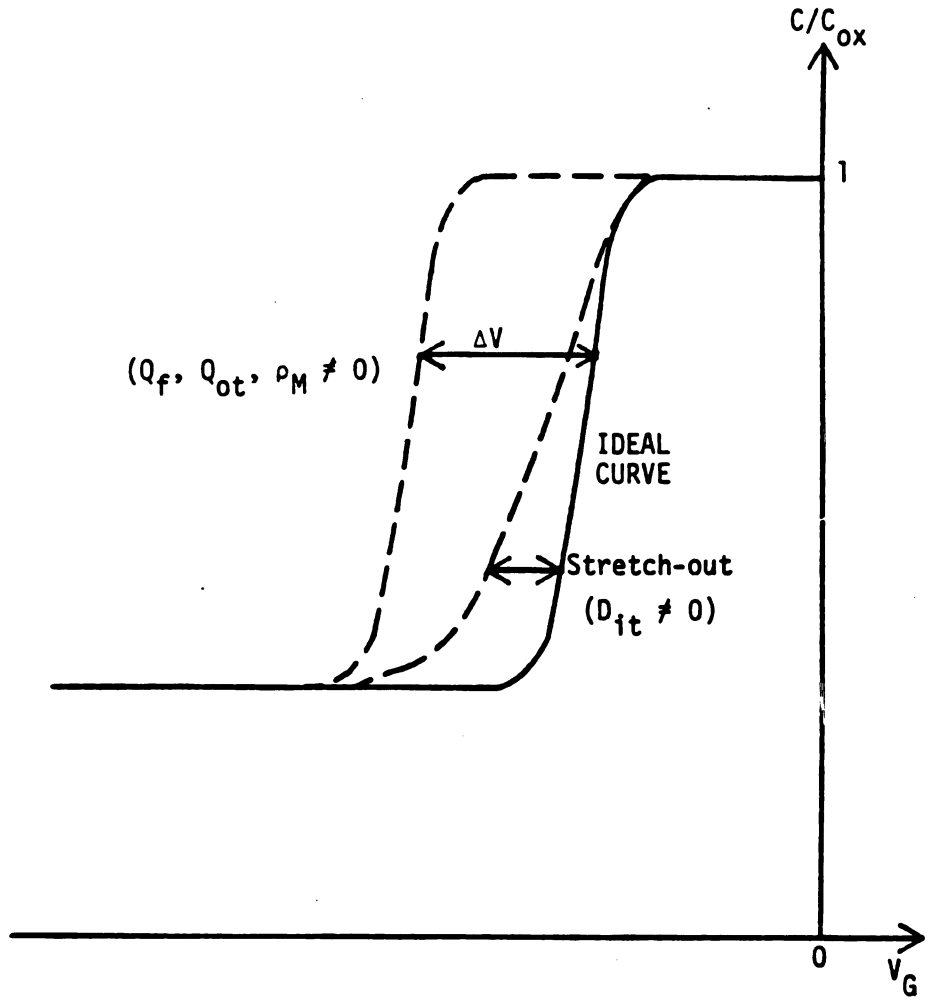

Figure 2.3 Typical high-frequency C-V curves for an MOS capacitor on n-type silicon, showing the effects of interface trap stretchout, and translation along the gate-bias axis due to fixed charges. For the ideal curve, $V_{FB} < 0$ due to the metal-semiconductor work function difference, ϕ_{MS}.

constants ranging from 10^{-8} to 10^{-1} s. Because of this rapid charge exchange, these states act as traps for carriers near the silicon surface, and thus they affect all of the important electronic properties of devices. The electronic properties of an interface can be characterized by the number density, time constants, and type (acceptor or donor) of interface traps as a function of energy.

In a seminal paper on the properties of the MOS capacitor (which was then referred to as the MOS diode), Terman [19] developed a theoretical model for the MOS capacitor with interface states, and described a method for extracting interface state density and time constant data from high-frequency C-V measurements on MOS capacitors. This method is described briefly here, and is presented in more detail, with an example, in Chapter 5. First, on the basis of the theoretical model, an ideal C-V curve is generated for the desired substrate doping and oxide thickness. Then the measured high-frequency C-V data are compared with the ideal curve. Bias-dependent shift, or dispersion, observed in the measured curve is attributed to interface states. By measuring the amount of dispersion present at a given capacitance and relating the capacitance to the silicon surface potential (which is related, in turn, to the position of the Fermi level in the silicon bandgap), the total interface state density at the energy corresponding to the position of the Fermi level can be calculated. If this is done at each value of capacitance on the measured C-V curve, interface trap density can be plotted as a function of energy in the silicon bandgap. In addition, by measuring C-V curves at frequencies ranging from very low (< 1 Hz) to very high (> 10 MHz), information about interface trap time constants can be deduced.

Alternative methods for measuring D_{it} have been developed. For example, in a method described by Berglund [20], capacitance is measured as a function of voltage at a frequency so low that ideally all interface traps respond to the measuring signal. Interface trap stretchout of the C-V curve is still present, but an additional capacitance, C_{it}, due to interface traps is also measured at each value of gate bias. The value of C_{it} can be computed from the measured low-frequency capacitance if the oxide capacitance and the silicon capacitance are known, and D_{it} can be computed from C_{it}.

Nicollian and Goetzberger [21] developed the theory and technique for extracting interface state properties from measurement of the equivalent parallel conductance of an MOS capacitor as a function of frequency. Although considerably more involved than capacitance techniques, conductance techniques offer higher resolution and more accuracy because in an MOS structure the conductance is entirely due to interface traps, whereas interface trap capacitance must be extracted from a model involving the silicon capacitance and the oxide capacitance.

2.5 Thermal Oxidation of Silicon

Thermal oxidation of silicon has been studied extensively for more than twenty-five years, owing to the crucial role played by this technology in the fabrication of integrated circuits and other electronic devices.

Identifying the oxidants and the actual reactions which take place during thermal oxidation of silicon has been the subject of a

considerable amount of investigation aimed at improving oxide quality and rendering the oxidation process more compatible with other steps in the IC fabrication sequence.

In general, thermal oxidation occurs as an oxidant species enters the existing oxide layer and is transported by diffusion to the Si surface, where an oxidation reaction occurs. Jorgensen [22] found that the oxidation rate was affected by a dc electric field applied to the oxidizing substrate. If the field was oriented to attract negatively charged species to the silicon surface, the oxidation rate increased. If the polarity was reversed, the oxidation rate decreased, and with a field of sufficient magnitude, oxidation ceased. Jorgensen concluded that a negative oxygen ion was the principal oxidant species involved in thermal oxidation.

However, evidence for the role of molecular O_2 or water vapor as the diffusing species during thermal oxidation was provided by the experiments of Deal [23] and Deal and Grove [24]. In these experiments, the oxidation rate in O_2 was proportional to the partial pressure of O_2, and in steam the oxidation rate was proportional to the partial pressure of water vapor. Raleigh [25] proposed that the Jorgensen results could be reconciled with those of Deal and Grove by considering that in the presence of a sufficiently high electric field, anodization occured at the Si-oxide interface and electrolysis occured at the gas-oxide interface.

Tiller [26,9] considered the oxidation problem from a detailed thermodynamic point of view. He concluded that (i) diffusion of neutral oxygen through SiO_2 could not be responsible for the observed parabolic rate constant; the diffusion of ionized oxygen was a more likely candidate. (ii) However, this diffusion was probably not

totally rate-controlling, and a likely possibility was that the observed parabolic growth characteristics arose as a consequence of vacancy and interstital transport of O^- ions in the Si. (iii) Processing alterations which would possibly lead to enhanced oxidation rates included: applying a negative surface charge to the SiO_2/gas interface; producing dissociation in the gas phase so that the surface saw O rather than O_2, leading to a higher population of O^- in the oxide; and enhancing the available vacancy source strength in the Si at the oxidizing interface by application of an electric field prior to oxidation, so that excess vacancies would migrate to the appropriate side of the substrate. Tiller noted that the microwave plasma oxidation studies of Ligenza [27] (described in Section 2.6) probably encompassed the first two of these processing alterations.

The basis for much of the practical work in the area of thermal oxidation of silicon is the model due to Deal and Grove, which was published in 1965 [24]. Although this model and the underlying theory are now understood to be incomplete, much of the data generated by Deal and Grove is still used in practice, and the relatively simple expressions developed in the theory are useful over a wide range of conditions encountered in practical applications. Because of its technical importance and the fundamental insights into the oxidation process which it offers, the Deal-Grove model for thermal oxidation is discussed here.

The Deal-Grove model is illustrated schematically in Figure 2.4. A substrate is immersed in an oxidizing ambient, either O_2 or steam, at a temperature T. The substrate is assumed to have an initial oxide layer of thickness x_i at t=0. The flux of oxidant (assumed to

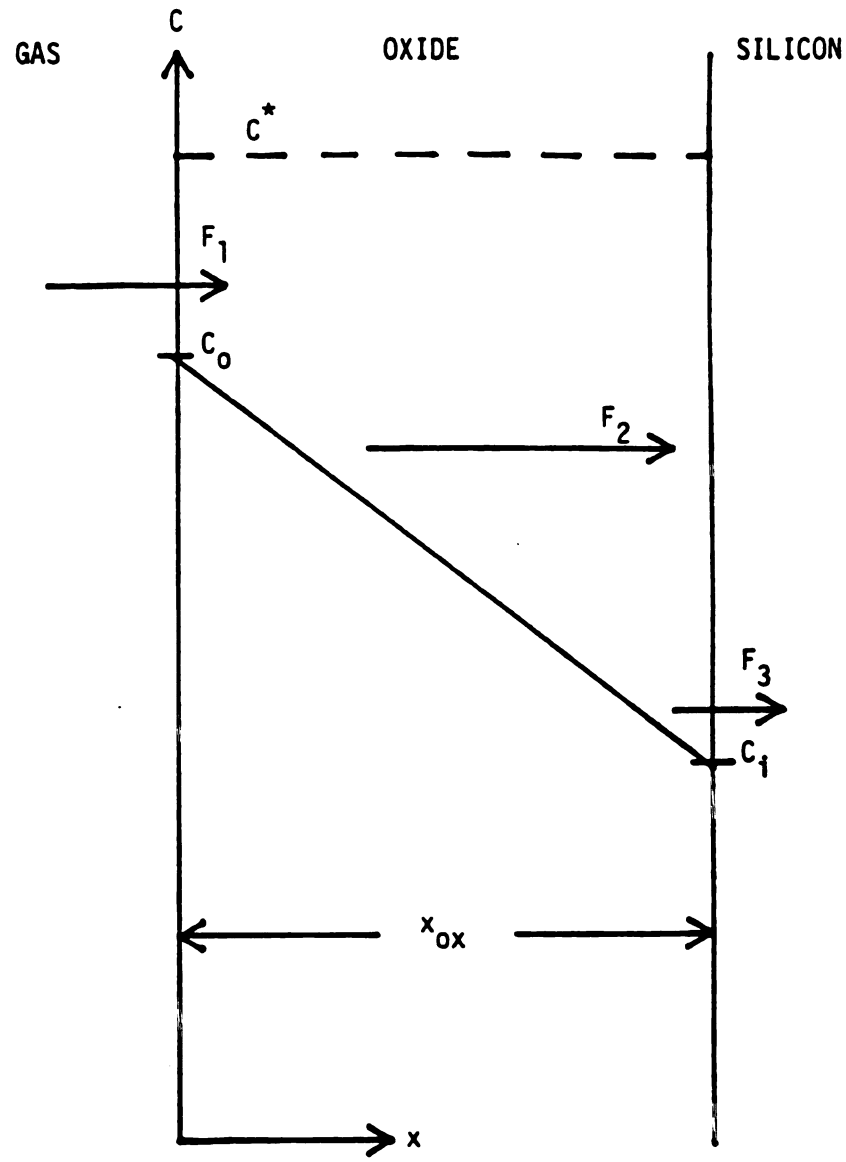

Figure 2.4 Deal-Grove model for thermal oxidation of silicon. C^* is the equilibrium gas concentration in the oxide, C_o is the surface oxidant concentration, and C_i is the oxidant concentration at the interface. F_1, F_2, and F_3 are the oxidant fluxes, which are equal in steady state.

be molecular O_2 or H_2O) from the gas phase into the oxide, F_1, is driven by the departure of the surface concentration of oxidant, C_0, from its equilibrium value in the oxide, C^*, such that

$$F_1 = h\,(C^* - C_0)\ .$$

The quantity h is the gas-phase mass transfer coefficient, which has units of velocity. The oxidant flux through the oxide layer obeys Fick's laws. In steady state, this leads to

$$F_2 = \frac{D\,(C_0 - C_i)}{x_{ox}}\ .$$

Here D is a diffusion coefficient, C_i is the oxidant concentration at the Si-oxide interface, and x_{ox} is the oxide layer thickness. The flux representing the oxidation reaction at the Si-oxide interface is assumed to be proportional to C_i, such that

$$F_3 = k_s C_i\ ,$$

where k_s is the chemical surface-reaction rate constant for the

oxidation reaction. In steady state, $F_1 = F_2 = F_3$, leading to a differential equation for x_{ox} which is solved by

$$x_{ox} = \frac{A}{2}\left\{\left[1 + \frac{4B}{A^2}(t + \tau)\right]^{\frac{1}{2}} - 1\right\} \qquad [2.9]$$

where

$$A = 2D\left(\frac{1}{k_s} + \frac{1}{h}\right)$$

$$B = \frac{2DC^*}{N_1}$$

$$\tau = \frac{(x_i^2 + Ax_i)}{B} \quad .$$

and N_1 is the number density of oxidant molecules incorporated into the oxide ($N_1 = 2.2\times10^{22}$ cm^{-3} for O_2, 4.4×10^{22} cm^{-3} for H_2O).

Two important limiting cases arise from consideration of Equation 2.9. For large values of the parameter $k_s x_{ox}/D$, the growth is diffusion-limited. The value of B becomes large and Equation 2.9 is approximated by

$$x_{ox}^2 = Bt \quad . \qquad [2.10]$$

This so-called parabolic growth approximation generally applies for growth of thick oxides in steam, and for long growth times. B is referred to as the parabolic rate constant.

The other limiting case occurs for small values of $k_s x_{ox}/D$. The growth in this case is limited by the oxidation reaction rate at the Si-SiO_2 interface, and Equation 2.9 is approximated by

$$x_{ox} = \frac{B}{A} (t + \tau) \ . \qquad [2.11]$$

The growth rate in this case is constant, and B/A is called the linear rate constant. This approximation is usually valid for thin oxides and short growth times.

A large amount of data is available for thermal oxidation of silicon, and the Deal-Grove model has been found to be valid for oxide thicknesses above about 300 Å, oxidant partial pressures of 1 atm or less, and temperatures above 800 °C. In most cases of practical interest, the oxide growth occurs under conditions intermediate to the limiting cases discussed above, and is therfore described as linear-parabolic. Also, the data indicate the existence of a behavioral regime not predicted by the Deal-Grove model. For oxidation in dry O_2, a rapid initial growth phase is observed before the onset of the linear growth given by Equation 2.11. The linear growth curve for dry thermal oxidation is always found to extrapolate to 230 ± 30 Å at t = 0, independently of temperature.

Over the range of validity of the Deal-Grove model, B is directly proportional to oxidant partial pressure, and A is independent of pressure. B increases exponentially with temperature. For dry oxidation the activation energy is very nearly equal to that for the diffusivity of O_2 in fused silica, and for steam oxidation the activation energy is close to that for the diffusivity of H_2O in

fused silica [2], which led Deal and Grove to conjecture that molecular transport through the oxide was important for thermal oxidation.

The linear rate constant for thermal oxidation is also dependent upon the crystal orientation of the silicon surface. This effect is due to the variation of available Si-Si bond density with surface orientation, combined with the effects of steric hindrance (limitations on bond formation due to the physical configuration of the reactants and their geometrical relationship to each other). The linear oxidation rate increases approximately in a ratio of 1:2:3 for (100), (110), and (111) oriented silicon [1].

Table 2.1 lists the values of the linear and parabolic rate constants for thermal oxidation under various conditions. The values in this table are used for reference in the discussion of the plasma oxidation literature in Section 2.6, and in the presentation of original results in Chapter 4. In order to prevent confusion, it is noted here that in the plasma oxidation literature the parabolic rate constant for oxidation is often denoted by k, rather than B.

Table 2.1. Rate constants for thermal oxidation under various conditions.

	Linear rate constant, B/A μm/h [Å/min]		Parabolic rate constant, B $\mu m^2/h$ [$Å^2$/min]	
T (^oC)	1000	1200	1000	1200
Dry O_2	6.5×10^{-2} [1.1×10^{1}]	1.0×10^{0} [1.7×10^{2}]	1.0×10^{-2} [1.7×10^{4}]	4.5×10^{-2} [7.5×10^{4}]
Steam	1.4×10^{0} [2.3×10^{2}]	1.2×10^{1} [2.1×10^{3}]	3.7×10^{-1} [6.2×10^{5}]	9.0×10^{-1} [1.5×10^{6}]

2.6 Plasma Oxidation of Silicon

2.6.1 Overview

The principal concerns of early studies in plasma oxidation were related to feasibility. It was especially important to demonstrate that suitable growth rates could be obtained at low temperatures with reasonable plasma input power levels. Later reports are concerned to a greater extent with oxide quality improvement, understanding plasma oxidation kinetics, and processing of larger substrate areas.

The works reviewed below include studies of oxidation and anodization of silicon in dc, rf, and microwave oxygen discharges. It will be noted that the conclusions of various investigators are not always in agreement. A partial explanation of this fact is that the results are not always readily compared because of the variety of experimental configurations employed, and the widely differing growth conditions. However, an attempt is made in this review to extract significant points of comparison and disagreement.

The literature is reviewed in approximate chronological order, first for studies of oxide growth characteristics and then for studies of oxide quality. A summary of the review is provided in 2.6.3.

2.6.2 Review of the Literature

Many of the important features of the formation of oxide films in a plasma were first observed by Miles and Smith in their study of the oxidation of aluminum in a dc discharge [28]. However, the earliest study of plasma oxidation of silicon was published in 1965 by Ligenza [27]. Ligenza hypothesized, based on the results of Jorgensen [22], that negative oxygen ions were the important oxidant species in plasma oxidation. Accordingly, the substrates were biased at a positive potential. The plasma was sustained by a 300 W, 2.45 GHz source resulting in a plasma density of about 10^{13} electrons/cm^3 and a neutral gas temperature less than 450 °C. The substrates in these studies were 1.1 cm^2 silicon wafers. Oxides up to 6000 Å thick were grown in one hour; this was comparable to the rate attainable by steam thermal oxidation at 1100 °C. Parabolic growth was observed for dc biases in the range of 30 to 90 V, with a bias-dependent rate constant on the order of 10^5 Å^2/min. This large growth rate was attributed to the diffusion-limited transport of negative oxygen ions through the oxide, driven by the exceedingly large concentration gradient of these plasma-generated ions across the oxide.

In a similar set of experiments, Kraitchman [12] grew 2000 Å oxides in 5 min and 6000 Å oxides in one hour. The oxidations were conducted in a 600 W, 2.45 GHz oxygen discharge. Large growth rates were obtained even on unbiased silicon samples. A parabolic rate constant of 1.9×10^5 Å^2/min was reported for unbiased samples; the rate constant increased to 3.6×10^5 for a constant 50 V bias, and further to 5.5×10^5 for a constant 280 mA/cm^2 bias (which required a

final bias potential of about 300 V). However, the observed growth was not strictly parabolic. In order to explain the growth data, a constant rate of oxide removal due to sputtering was assumed. The sputtering rate deduced from the growth curves increased with increasing bias from 22 Å/min to 35 Å/min . The growth law arising from the combination of sputtering and oxide formation predicted the existence of a bias-dependent limiting thickness, which was greater than 4000 Å in every case. Kraitchman argued against the role of negative oxygen ions that had been proposed by Jorgensen and Ligenza. The rationale provided for this was that for zero or small positive biases, the silicon substrate (anode) and the cathode, both immersed in the microwave plasma, approximated an ideal double-probe system, and therefore both would assume a negative potential with respect to the plasma. Furthermore, practically all the negative ions would be produced with only a few electron volts of thermal energy, which was insufficient to overcome this sheath potential barrier. For larger bias values in the range from 50 V to 300 V, Kraitchman considered that ideal probe theory was no longer applicable, and postulated that a large negative ion flux would indeed be drawn to the anode, with the effect of imparting energy to the samples and promoting formation of the as-yet undetermined mobile oxygen species that was principally responsible for the oxidation.

It should be noted, however, that most subsequent investigations have led to the conclusion that negatively charged oxygen ions do play an important role in plasma oxidation.

Several investigators have studied oxidation in a dc discharge [14,29,30]. In [14], Ligenza and Kuhn reported the growth of oxide films up to 900 Å thick in ten minutes on substrates maintained at

225 ^{o}C. A constant current bias of 35 mA/cm^{2} was applied to these samples, while the plasma was maintained by 400 W of dc power (4 A at 100 V). The anodization potential increased nearly linearly from 15 to 60 V above the plasma floating potential as the oxide thickness increased; this was taken to indicate that the oxide grew linearly over the ten minute period. The oxidation mechanism proposed was the shallow implantation of O_2 in the existing oxide, followed by conversion to interstitial O^- and subsequent transport to the Si surface. This involvement of O^- is in agreement with Tiller's hypothesis [9] for thermal oxidation. However, in a report of experiments designed specifically to identify the oxidizing species in dc and microwave plasma oxidation, Moruzzi, et al. [13] concluded that ions of the form O_x^- were the most likely candidates. In these experiments, apparatus similar to that of Ligenza was used. Microwave input power was varied between 100 and 200 W, and data was generated regarding the variation of oxide growth rate with gas pressure, time, and temperature. Over the entire range of conditions studied, the growth was found to be parabolic, with a maximum parabolic rate constant of 2.7×10^{5} Å^{2}/min achieved with 200 W microwave input power and 100 V bias at 0.1 Torr. The substrate temperature under these conditions was 525 ^{o}C. In order to identify the oxidizing ion species, experiments were carried out in which the sample wafer was perforated with a 100 μm aperature, allowing a sample of the charged particles arriving at the anode to pass into a second vacuum chamber containing a mass spectrometer. Microwave discharges and dc glow discharges were studied. In a microwave discharge the negative ions were found to be predominantly O^-, while in a dc discharge almost equal amounts of O_1^-, O_2^-, and O_3^- were observed. In order to further test the hypothesis

that O^- was the active species in microwave plasma oxidation, two investigations were conducted. In the first, H_2 was added to the oxygen flow at a concentration of 1 percent. The effect of the hydrogen was to dramatically reduce the O^- concentration in the plasma through the scavenging reaction

$$O^- + H_2 \rightarrow H_2O + e.$$

The oxidation rate was found to be very low for such mixtures, even though the mean electron energy in the plasma was known to be nearly equal to that for pure oxygen, lending support to the O^- hypothesis. In the second investigation, a small amount of N_2O was added to the oxygen. This increased the negative ion concentration and changed the ion species to O_2^- via the reactions

$$O^- + N_2O \rightarrow NO^- + NO$$

and

$$NO^- + O_2 \rightarrow O_2^- + NO.$$

Again, the oxidation rate was low, which led to the conclusion that O_2^- was not the ionic species responsible for oxidation. These results were complicated by the observation that at a pressure of 1 Torr the oxidation rate was reduced to about one-third of its value at 0.1 Torr, even though the O^- signal measured by the mass spectrometer was nearly unchanged. The possible explanations given for this included the existence of an excited neutral species in the discharge with a rate of formation similar to that of O^-, which was

actually responsible for the oxidation, or the occurrence of oxidation due to electron attachment to absorbed oxygen, or some other complex surface reaction.

Further evidence for the role of negative ions in plasma oxidation was provided by the work reported in [29]. In these experiments, negative oxygen ions were selectively prevented from reaching the substrate by the application of an rf bias, and under this condition oxidation was observed to cease.

Ray and Reisman [31] and Ho and Sugano [7] separately reported oxidation in 1 kW, low frequency RF plasmas. It is interesting to compare and contrast their results, since unbiased samples were used in [31] while constant current biasing was used in [7].

In [7], the frequency was 420 kHz and the pressure was 0.2 Torr. Parabolic rate constants up to 1.5×10^6 $Å^2$/min were achieved when the samples were located near the power input coil, where the plasma density was measured to be about $1 \times 10^{12} cm^{-3}$. The highest growth rates were achieved when the substrate temperature was maintained at 600 ^oC by an external heater. When a constant bias current density of 30 mA/cm^2 was applied, the resulting external bias potential increased from near zero to over 200 V as the oxide grew. Higher bias current densities resulted in higher oxidation rates. The plasma density 20 cm from the power input coil was measured to be $5 \times 10^{10} cm^{-3}$. When the samples were mounted in this position, the oxidation rate was very low, even though the substrate temperature was maintained at 600 ^oC. (The effect of plasma density on oxidation rate was investigated in detail in [32].)

In [31], the source frequency was 3 MHz and the pressure was varied from 2 to 60 mTorr. As previously mentioned only unbiased

samples were studied. As in [7], oxidation was only observed when the samples were close (2 cm) to the power input coils. Interestingly, however, at a substrate temperature of 540 ^{o}C oxidation rates equal to those reported in [7] were observed on these unbiased samples, but only on the side of the samples facing away from the plasma (the back side). Oxidation was observed on the front side, but at a rate 4 to 5 times lower. On each side, the oxidation appeared to occur in two stages. During the first stage the growth was linear. During the second stage, which began at about 1500 Å on the back side, the growth was parabolic. Ho and Sugano obtained similar results on samples biased with constant current, and concluded that, in contrast to the constant-voltage results of Ligenza and Kraitchman, the oxidation during the initial stage was not due principally to oxidant diffusion, rather it was due to field-induced ionic drift in the oxide. Observed deviations from linear growth during the initial stage were attributed to oxide space charge effects. For constant current bias, Ho and Sugano found that a minimum oxide electric field was required for oxidation to proceed. The value of this field was found to be about 1.5 MV/cm and was slightly dependent upon the bias current density. Ray and Reisman found no dependence of growth rate upon the crystal orientation of the sample surface, in contrast to the case for thermal oxidation (Section 2.5). This was construed to indicate that the growth process was mass-transport limited, rather than interface reaction rate limited. Ho and Sugano concluded, based upon O^{18} tracer experiments, that oxidation occurred both at the plasma-oxide interface and at the oxide-silicon interface, and suggested that the dominant oxidation mechanism was the motion of Si and O ions and/or their

vacancies across the oxide in opposite directions under the influence of the oxide field.

In a later paper, Perriere et al. [16] presented results of more O^{18} tracing experiments. Oxygen transport in growing oxide films was studied in a 300 W, 300 MHz oxygen discharge. The samples were biased with a constant current, and the sample temperature was varied between 25 ^{o}C and 600 ^{o}C. The results of this study indicated that oxygen order was preserved during the oxidation (i.e., the most recently formed oxide was farthest from the Si-SiO_2 interface), and this was explained by short-range field-assisted migration of oxygen ions via interstitialcy or vacancy mechanisms. It was specifically noted in this report that the long-range migration of part of the oxygen found by Ho and Sugano, as indicated by new oxide formation at the silicon interface, was not observed. The authors also concluded that only oxygen, not silicon, migrated during the oxidation.

The oxidation of unbiased samples at low pressure was studied by Bardos, et al. [33,34]. In these experiments, low pressure oxidation was successfully carried out in a magneto-active plasma. The plasma was sustained by a 3 kW pulsed power source operating at 2.35 GHz, which delivered 100 W average power. A static magnetic field near electron-cyclotron resonance (ECR) was applied to the plasma in order to increase the plasma density. The maximum plasma density attained was 2×10^{13} electrons/cm^3. Oxide thickness and plasma density were measured versus pressure for a fixed magnetic field strength and oxidation time. The plasma density was nearly constant over the pressure range studied, but the growth rate exhibited strong peaks at 3×10^{-4} Torr and at 0.3 Torr, with a maximum parabolic rate constant of about 7×10^{4} $Å^2$/min. Oxide thickness and plasma density were

measured as the ratio of the electron-cyclotron frequency, ω_{ce}, to the source frequency, ω, was varied in the range from 0.8 to 1.6 by changing the magnetic field strength. The oxidation rate was found to increase with plasma density in the range 2×10^{12} to 4×10^{12} electrons/cm^3. An important result of these magneto-active plasma experiments was the observation of the oxide damage produced by fast electrons. In a subsequent paper [35], this was explored further, and it was concluded that if electron energies in the plasma did not exceed 30 eV, oxide defects and heating of the silicon during oxidation could be avoided. Based on further experiments in the magneto-active plasma environment, Musil, et al. [36], concluded that a minimum plasma density exists, below which oxidation ceases. This was explained with reference to the plasma floating potential, which was found to be large and negative for densities below about 5×10^{12} cm^{-3}, but saturated at about -10 V for higher densities. Oxidation was observed at densities greater than this saturation point, but not below it. The conclusion was that in order for oxidation to proceed, the plasma floating potential must be close to or greater than the substrate potential.

Work on unbiased samples in magneto-active plasmas was summarized in [32], and additional results were presented. The dependence of oxidation rate upon plasma density was found to be linear. It was concluded that CW microwave sources are more suitable for oxidation in a magneto-active plasma than are pulsed power sources, because CW sources do not excite fast electrons at ECR.

Up to this point in the review, the reported characteristics of oxide growth have been considered. In most of the oxidation experiments reviewed here, oxide quality also was investigated. Various

techniques were used, the most common of which was C-V characterization of MOS capacitors formed on the plasma-grown oxides.

Kraitchman [12] compared the properties of oxide films grown in a microwave plasma with the properties of oxides formed by other low temperature processes, and with the properties of thermal oxides. The flatband voltage of MOS capacitors on the plasma oxides was equal to that obtained on thermal oxides used for comparison, indicating that the oxide fixed charge density was the same for each. The plasma oxide capacitors were subjected to bias-temperature stressing at 200 ^{o}C. The flat-band potential shifted in the negative direction with the application of a negative bias, and shifted in the positive direction with a positive bias. The polarities of these shifts were opposite to those that would arise from the migration of mobile ions, either positive or negative, in the oxide. Instead, these shifts might have been due to charge injection during the stress cycle, similar effects having been observed in anodic oxides and in some thermal oxides. It was concluded that the plasma oxides were comparatively free of mobile ionic impurities. Other oxide properties investigated included etching rate, refractive index, resistivity, breakdown field, dielectric constant, and infrared absorption. In the categories investigated, the plasma oxides were comparable to thermal oxides of the time, and were comparable to or better than pyrolytic (CVD) or anodic oxides. In this study, values of interface trap density were not determined.

Ray and Reisman [31] reported a mid-gap D_{it} value of 3×10^{12} $cm^{-2}ev^{-1}$ for as-grown RF-plasma oxides grown on unbiased substrates. As previously noted in Section 2.4, present-day (1986) thermal oxides have as-grown D_{it} values in the range of 10^{11} to

10^{12} $cm^{-2}ev^{-1}$. After a postmetal anneal at 450 °C in forming gas (5 percent H_2 and 95 percent N_2), D_{it} for the plasma oxides was reduced to 6×10^{10} $cm^{-2}ev^{-1}$, and after a subsequent 20 min anneal at 1000 °C in Ar, D_{it} was reduced further to 2×10^{10} $cm^{-2}ev^{-1}$. Present-day thermal oxides have D_{it} values on the order of 10^{10} $cm^{-2}eV^{-1}$ after annealing. The plasma oxides studied by Ray and Reisman had substantially larger values of D_{it} than annealed thermal oxides unless they were subjected to a high temperature anneal, thus partly negating the advantages of low-temperature processing. As-grown plasma oxides exhibited breakdown fields around 4 MV/cm. The breakdown field was unaffected by the high temperature Ar anneal described above, however a 15 min anneal at 1000 °C in dry O_2 raised the breakdown field to around 8 MV/cm. The breakdown field for thermal oxides used for comparison was 10 MV/cm. The refractive index and etch rate of the plasma oxides were similar to those of thermal oxides. Calculations of oxide stress, unique to the plasma oxidation literature reviewed here, were made based upon the film thickness, the substrate thickness, and measurements of the radius of curvature of the substrate. These calculations yielded values of $1.5\text{-}1.6\times10^{9}$ dynes/cm^2 for the plasma oxides, compared with $3.1\text{-}3.4\times10^{9}$ dynes/cm^2 for thermal oxides. This difference in stress was explained as arising mainly from the difference in growth temperatures (500 °C for the plasma oxides, 1000 °C for the thermal oxides) and subsequent cooling to room temperature. Microscopic examination of the silicon surface, after etching the plasma-grown oxides, revealed that oxidation-induced stacking faults were absent.

Ho and Sugano [7] measured mid-gap D_{it} values on the order of 10^{12} $cm^{-2}ev^{-1}$ for as-grown plasma oxide samples. These large values

were significantly reduced to the order of 10^{10} $cm^{-2}ev^{-1}$ by a low-temperature post-metal anneal. This value is substantially lower than reported in [31]. and is unique in the literature in that a D_{it} value comparable to thermal oxides was obtained for plasma oxides that were subjected only to low temperature processing. The breakdown field of the plasma oxides was reported to be as high as 7×10^6 V/cm. The etching rate of these oxides was reported to be the same as that measured by Kraitchman in [12]. The structure of the plasma oxides was investigated by electron diffraction and by electron spin resonance (ESR). The electron diffraction pattern revealed that the oxide was amorphous. ESR indicated the presence of a defect center within 100 Å of the Si-SiO_2 interface. The signal corresponding to this defect center disappeared after a 1 h, 450 °C anneal in forming gas, but reappeared after subsequent annealing under the same conditions in argon. In order to explain this effect, it was suggested that the defect centers were bleached by hydrogen atoms that diffused to the interface. Impurity redistribution on these samples was probed by forming Schottky diodes on both n-(boron) and p-type (phosphorus) substrates after etching, and then measuring the C-V characteristics. No redistribution of either boron or phosphorus was measurable.

The characteristics of plasma oxides grown in a magneto-active plasma were investigated in [32] and [35]. In [32], the oxides were grown in a plasma excited at ECR by a CW source, thus fast electron damage was avoided. The value of Q_f calculated from the flatband voltage was 9.5×10^{11} cm^{-2}, and the breakdown strength was 10^6 V/cm. The data presented showed very little C-V curve hysteresis, indicating that the density of mobile ions in the oxide was low. Samples

were also grown in plasmas with $\omega_{ce}/\omega > 1$. Oxidation was faster than at ECR because the plasma density was greater. However, the electrical properties were found to be very poor; this was attributed to fast electron damage. In [35], values of N_{it} exceeding 10^{13} cm^{-3} were reported for such samples, and breakdown fields were typically less than 0.1 MV/cm.

Ligenza and Kuhn investigated the properties of oxides grown in dc discharges [14]. The MOS characteristics of as-grown oxides were dominated by fast interface traps, but after annealing in H_2 for 6 h at 350 ^{o}C, D_{it} was reduced to 1 to 3×10^{11} $cm^{-2}ev^{-1}$. The C-V characteristics showed no hysteresis. The bulk properties of these oxides, even in the as-grown state, were claimed to be equal to those of the best thermal oxides.

The bird's beak effect described in Section 2.2 was investigated in [31] and [7], and was found to be completely absent on plasma-grown masked oxides. In [31], 3800 Å oxides were grown using 2000 Å of MgO as a mask. In [7], Al_2O_3 was used as the mask material. In both cases, after the mask was removed, the oxide surface was examined by SEM. The absence of the bird's beak structure on plasma oxides is explained in [7]: in the plasma anodization process the lateral oxide field strength is small compared with the vertical oxide field strength, so that the lateral oxidation rate is much smaller than the vertical oxidation rate.

Some variations on the basic plasma oxidation process have recently been reported. For example, enhancement of the oxidation rate and improved oxide quality have been demonstrated using calcia-stabilized zirconia (CSZ) overlay films [37]. The observed effects were attributed to the ionic filtering action of the CSZ film, in

conjuction with the protection from oxide surface damage and contamination which it offered.

As another example, enhancement of the oxidation rate at very low substrate temperature (50 ^{o}C) was observed upon the addition of a small amount (0.5%) of F to an oxygen discharge [38]. This was attributed to a catalytic reaction involving F at the interface, leading to enhancement of the interfacial reaction rate by reduction of the activation energy for Si-O bond formation.

As a final example, oxide formation has been demonstrated in microwave stream transport system [11,39]. In this system, plasma is formed in a reaction chamber and guided to the substrate surface by a confining magnetic field. The substrate is not exposed directly to the plasma, resulting in a cleaner processing environment. In these studies, oxide thicknesses of 230 Å were formed in 1 h, with $D_{it} = 7 \times 10^{10}$ $cm^{-2}eV^{-1}$.

Several workers have fabricated FET's using plasma-grown oxides for gate dielectrics [40-42]. In the earlier work, a high temperature (1000 ^{o}C) annealing step was required to achieve acceptable device performance. However, in the most recent work [42] (1986), the maximum processing temperature was 850 ^{o}C which is generally considered to be in the moderate range of processing temperatures.

2.6.3 Summary

The typical growth rate for SiO_2 formed in an oxygen discharge is roughly 1000 Å/h. Oxides can be formed in dc, rf, or microwave

discharges, but microwave discharges offer the highest plasma densities, a property which is desirable for the formation of high quality oxide films at low substrate temperatures.

Plasma oxidation most probably occurs to the drift and diffusion of O^-, $O^=$, and possibly other energetic or activated negatively charged and neutral species through the oxide to the reaction interface. The growth data are often fit by curves representing linear-parabolic kinetics, although there is no comprehensive model for plasma oxidation, including oxide field and space charge effects, upon which to base such a fit.

Except for one case, [7], interface state properties of low-temperature plasma-grown oxide films are not as good as state-of-the-art thermally grown oxides. However, plasma-grown oxides show the absence of stacking faults as well as the the birds-beak effect, result in negligible impurity redistribution, and can be formed at high growth rates.

2.7 Modeling of Plasma Oxidation Kinetics

A number of authors have reported growth rate coefficients for plasma oxidation of Si and GaAs based upon simple linear-parabolic kinetics [27,31,12,13,43]. Logarithmic growth was reported in [44] for plasma anodization in a dc discharge. The effect of re-sputtering the growing oxide at a constant rate was included in [12]. However, in most reports, modeling was not the major concern and the issue of growth kinetics was purposely over-simplified. However, a few authors have specifically addressed modeling of anodic film growth, and their work is reviewed below. In addition, Chapter Six

includes a derivation of the high field discrete hopping model which is discussed briefly here.

Cabrera and Mott [45] modeled anodic oxide film formation by considering the forward and reverse currents that would flow due to ionic hopping in the film in the presence of discrete energy barriers (e.g., hopping between vacancies or interstitial sites), including potentially rate-limiting barriers at the oxide interfaces. Based on this model, Cabrera and Mott were able to predict qualitatively the observed parabolic growth of oxides on some metals, and also the initial linear growth stage often observed for thin oxide films.

Fromhold and Cook [46] derived an expression for the steady-state current produced by a large, homogeneous electric field in the presence of a concentration gradient, based on the discrete-hopping model. However, at the time of this derivation (1966) there were insufficient experimental data with which to compare the numerical results of this development.

However, Fromhold and Kruger [47] (1973) showed that the growth rates predicted by the formulation in [46] were, in many cases of interest (e.g., in the presence of a large externally applied field), orders of magnitude greater than those actually observed, and they presented an improved model for anodic oxidation which included retardation effects due to space charge in the oxide. Space charge effects were included by numerically solving a discrete version of the discrete hopping model simultaneously with Poisson's equation, while imposing boundary values at both reaction interfaces and requiring continuity of current throughout the oxide film. (This is discussed in more detail in Chapter Six.) Two important process-

related parameters which were used in this model were the ion concentration at the oxide surface, and a transport coefficient, called the migration coefficient, which incorporated the effects of ion transport in the oxide by diffusion and an electric field. Families of growth curves and space charge concentration profiles were computed, and the results were compared with the homogeneous electric field case. The major conclusions were that (i) the kinetic growth curves were severely rate-limited by relatively moderate space charge concentrations, (ii) space charge caused the growth kinetics to have an increased limiting-thickness character, (iii) total space charge in the anodic film increased with increasing current levels, and, for a given current level, the space charge became more confined to the interfaces as film thickness increased, and (iv) the growth could not be described accurately by a linear relationship between the logarithm of anodization current and any one of the following: thickness, reciprocal thickness, or logarithm of the thickness. The significance of the latter conclusion was to suggest that to fit empirical data by curves representing these simple relationships (as is often done in the literature) might result in obscuring a more complicated underlying growth mechanism.

This work was extended by consideration of the special case of anodization under conditions of high space charge in very large electric fields applied to thick films [48]. The conclusion, based on numerical computation, was that space charge retardation of growth became more pronounced under these conditions. As a specific example, for a 10,000 Å film with an anodization voltage of 100 V, the required growth time was 1000 times longer with space charge effects than in the homogeneous field case. An additional finding of this

analysis was that film thickness grown in a given time varied approximately linearly with anodization voltage.

In [49], an analytical version of the space-charge modified discrete-hopping model is used to fit data obtained for rf-plasma anodized samples. Some additional experimental confirmation of the numerical results reviewed above was presented in [50]. The particular system investigated was GaAs anodization in an oxygen plasma. The ion flux in the oxide was modeled as described in [48]. The electron current in the oxide was deduced by measuring simultaneously the oxide thickness and the total bias current at a constant voltage, and subtracting the indicated ion current (proportional to growth rate) from the total current. A plot of electron current vs. mean oxide field was generated, indicating the existence of two distinct electric field regimes. For lower values of electric field, in this case below about 4 MV/cm, electron current increased sharply with field, and the current depended upon sample temperature. For higher values of electric field, the current saturated, and was independent of sample temperature. The behavior in the lower field regime was attributed to an oxide limited conduction mechanism, whereas the saturation effect was attributed to a plasma-limited charge supply. The model-generated growth curves were fit to the experimental data by adjusting the values assumed for the ion migration coefficient and the ion surface concentration. Data were generated in the temperature range from 50 ^{o}C to 200 ^{o}C for film thicknesses up to 4000 Å. Values of migration coefficent were in the range 10^{-10} $cm^{-2}s^{-1}$ to 10^{-13} $cm^{-2}s^{-1}$, considerably higher than typical diffusion coefficients, which indicated the effect of field-assisted transport. Ion surface concentrations were on the order of 10^{18} cm^{3}. The migration

coefficient decreased linearly with reciprocal temperature, and oxide voltage was observed to increase linearly with film thickness for constant current anodizations.

A numerical model based on the discrete hopping model, including space charge, is investigated in Chapter Six, and the results are compared with the experimental results from the plasma oxidation experiments described in Chapter Three and Chapter Four, and with the predictions of the Deal-Grove linear-parabolic model.

Chapter Three

Microwave Plasma Oxidation of Silicon: Experimental Method

3.1 Introduction

This chapter describes the experimental techniques and apparatus which were used in an investigation of the oxidation of silicon in a microwave oxygen discharge. In these experiments, the formation of silicon dioxide layers on Si substrates was observed under a variety of conditions, with the objectives of (a) investigating the characteristics of oxide growth in a microwave plasma disk reactor (MPDR), and (b) correlating the growth with the particular experimental parameters selected for study. The MPDR is described in Section 3.2. Additional apparatus is described briefly in Section 3.3. Section 3.4 addresses the selection of the experimental pararameters and their ranges, and the experimental procedure is discussed in Section 3.5.

3.2 The Microwave Plasma Disk Reactor (MPDR)

The microwave plasma disk reactor concept was first described by Asmussen, et al., in [51], and subsequently in [52-53]. It embodied a significant modification of the coaxial discharge apparatus such as that described in [54], whereby the cylindrical coaxial discharge tube was truncated to the shape of a disk in order to confine the plasma near the work surface. A principal advantage of the plasma disk reactor in surface processing applications is that the plasma is confined closely to the substrate being treated, so that large surface areas can be processed while the total plasma volume required to be generated is small. This feature is in marked contrast with the microwave plasma oxidation studies of Ligenza [27] and Kraitchman [12] discussed in Section 2.6. An advantage common to all microwave discharge apparatus is that higher plasma density is achieved over a wider range of pressure than for dc or rf discharges, and a wide variety of neutral, excited, and ionized atoms and molecules are produced. This can be attributed to the higher ionization efficiencies characteristic of microwave discharges [55]. High plasma density is usually desirable in materials processing applications because this leads to a higher concentration of active species at the work surface. Another important advantage of the MPDR is that the microwave power applicator is a continuously tunable resonant cavity structure, so that operation with nearly zero reflected power is possible under a wide range of loads imposed by the plasma and the substrate, and the reactor can operate at lower pressures than other structures. In addition, the cavity can be operated in a single transverse electric (TE) or transverse

magnetic (TM) mode, which may have practical utility. For example, operation in a TE mode, in which the microwave electric field is parallel to the substrate surface, might reduce substrate surface damage due to hot electrons from the plasma. Single mode operation is a feature which has not been reported in previous investigations of microwave plasma oxidation.

A principal objective of this research was to investigate the results of applying the microwave plasma disk reactor concept to surface processing of semiconductors. A description of the MPDR is included in 3.2.1. Paragraph 3.2.2 covers the fundamental principles of operation of the MPDR, and 3.3.3 briefly describes other applications of the disk reactor concept. More information on the MPDR and on some of its applications is available in [51-54] and [56-62].

3.2.1 Description of the MPDR

A schematic cross-section of the MPDR in two different configurations is shown in Figure 3.1. A detail view of the MPDR baseplate used in the oxidation experiments is shown in Figure 3.2. Referring to Figure 3.1, the outermost part of the reactor was a microwave resonant cavity, formed by hollow brass cylinder (a), baseplate (b), and movable sliding short (c). Inside the resonant cavity was a plasma confinement region (d), bounded by quartz housing (e), annular ring (f), baseplate (b), and perforated plate, or grid (g). Microwave power was coupled to the cavity by adjustable probe (h) which was connected to a power source by coaxial cable or

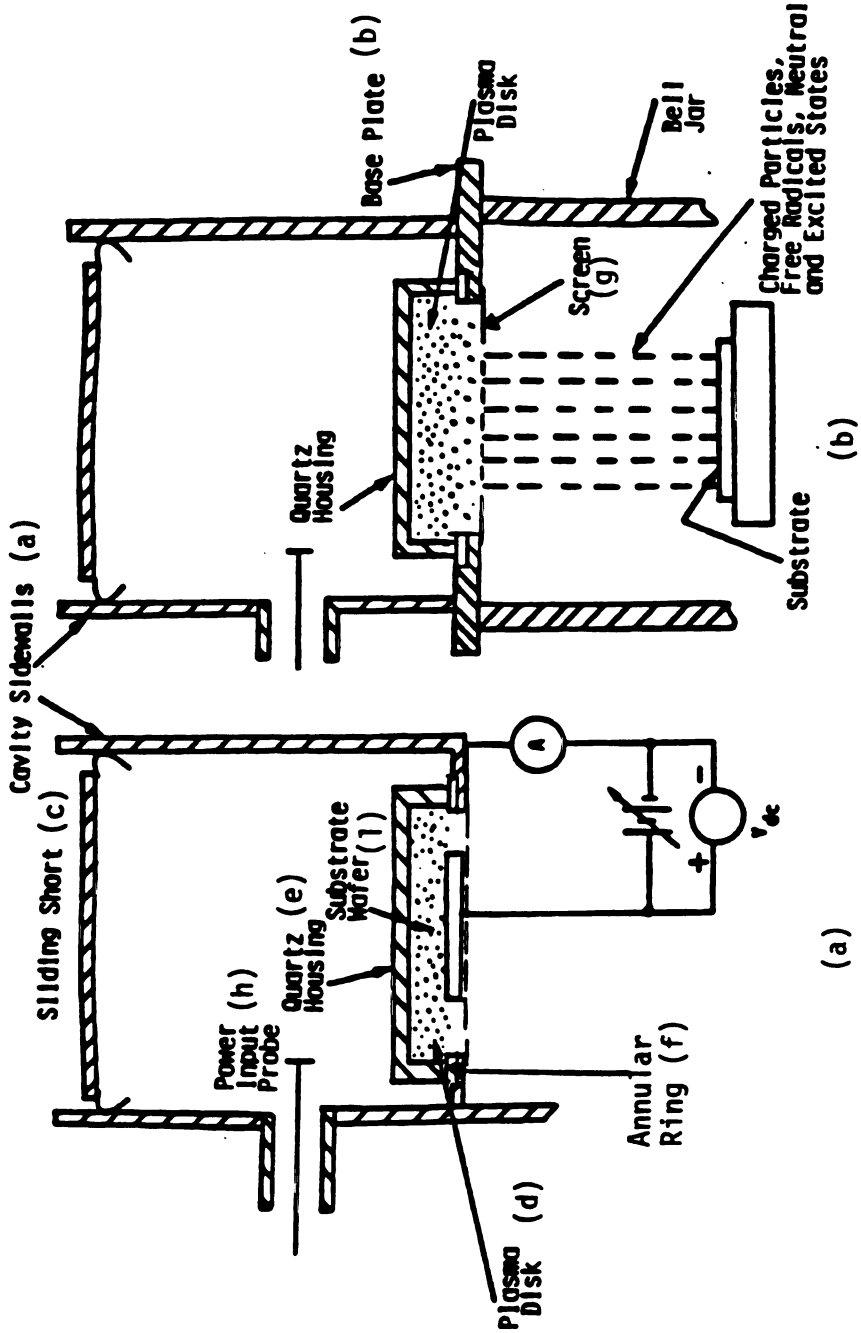

Figure 3.1. Schematic cross-section of the MPDR in two configurations. (a) Substrate is in the discharge enclosure. (b) Substrate is below the baseplate, downstream in the gas flow.

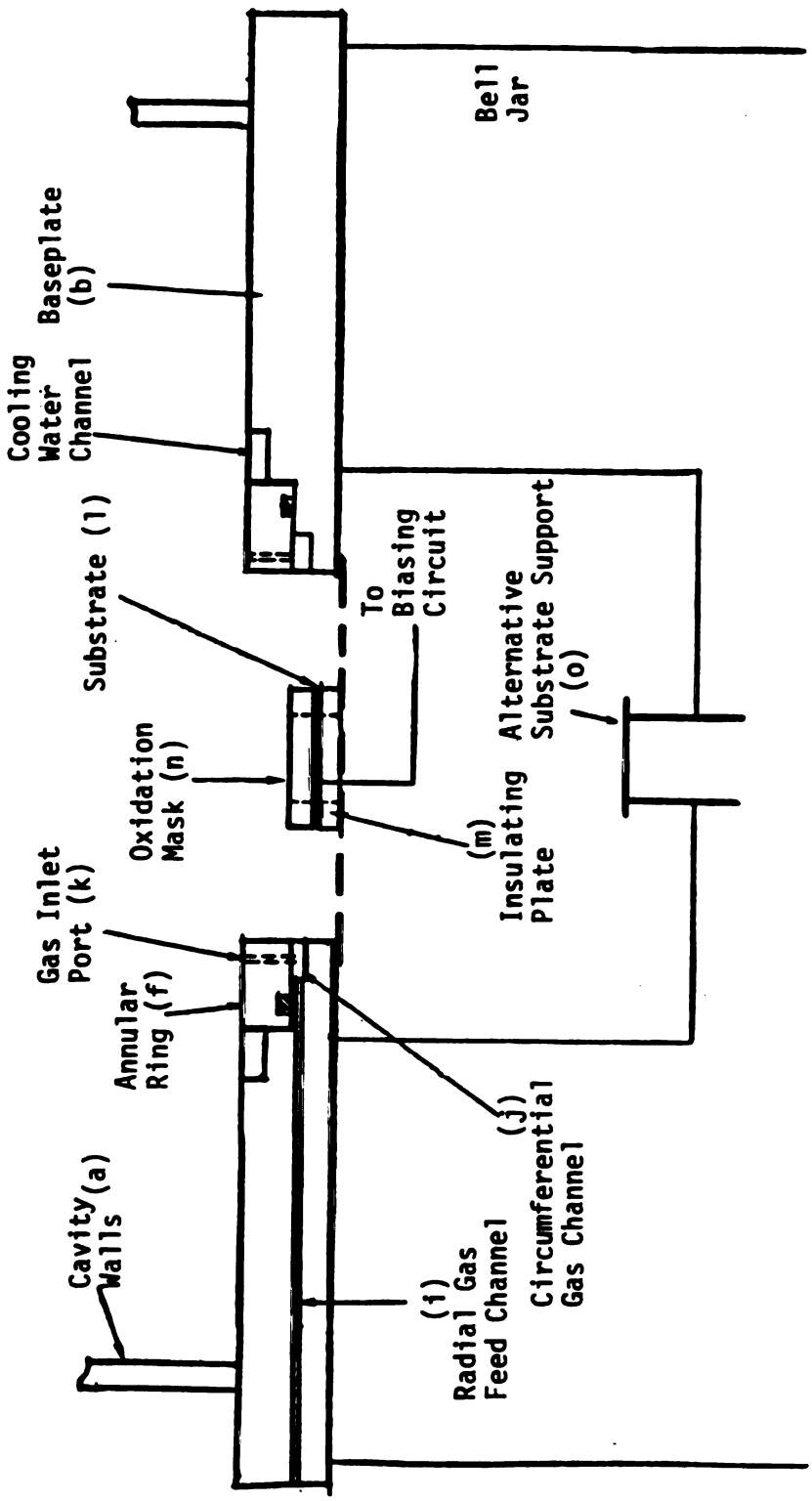

Figure 3.2. Detail of the MPDR baseplate and substrate mounting. Quartz housing (e in Figure 3.1), which seats on the annular ring, is omitted for clarity.

flexible waveguide. Details of the gas supply system and sample mounting are shown in Figure 3.2. Gas for the discharge was supplied through radial channel (i), bored into the baseplate, which connected with a circumferential channel (j) in the baseplate. Gas was admitted from channel (j) to the discharge region through eight symmetrically placed vertical holes (k) in annular ring (f). In most experiments, a sample (l) was mounted in the discharge chamber, insulated from the baseplate by a quartz plate (m), and masked by another quartz plate (n). Alternatively, a sample could be mounted below the baseplate on support (o).

The MPDR used in the plasma oxidation experiments was scaled for operation at 2.45 GHz, and it was constructed in such a way that the only materials exposed to the plasma were stainless steel and quartz. The plasma confinement region used in the oxidation experiments was 10 cm in diameter and 1.5 cm high, however, the annular ring (f) is replacable, which would allow quartz confinements of different diameters to be accomodated in future experiments.

3.2.2 Principles of Operation

In the MPDR, application of microwave power to the resonant cavity structure resulted in ignition of a discharge in the region enclosed by the quartz housing and the baseplate. The discharge was confined to this region, except for a low density tail extending a short distance below the baseplate grid. Samples to be oxidized were placed either in the discharge zone, or downstream, below the grid.

For a detailed derivation of the electromagnetic fields in an empty cylindrical cavity, the reader is referred to [63]. Plots of

the field patterns associated with the 30 lowest order empty cylindrical cavity resonances are available in [64]. A tabulation of the lower order resonant modes which can be generated at 2.45 GHz in an empty cavity of the size used in the MPDR oxidation experiments is available in [65]. Measurements utilizing a sweep oscillator / cavity wavemeter setup confirmed the existence of these modes in the particular MPDR used in the oxidation experiments, and also yielded the cavity length and probe insertion data necessary to couple power to these modes. The presence of a plasma in a cavity alters the empty cavity fields and changes the tuning lengths; in practice these tuning lengths were determined empirically for the conditions of interest (i.e., see Figure A.3 in the Appendix).

In a microwave discharge, gas breakdown is initiated by ionization of some gas molecules by stray free electrons which have been accelerated by the electric field. Ionization of a gas is most easily accomplished (i.e., requires minimum electric field strength) at a particular combination of pressure and field oscillation frequency which depends primarily upon the characteristic diffusion length for electrons in the gas [55]. In a resonant cavity, local maxima in the electric field strength result in breakdown at lower input power levels than would otherwise be required.

In order to ignite a discharge in the MPDR, the cavity length was adjusted by moving the sliding short (c in Figure 3.1) to a previously determined optimum discharge ignition position (specific values are provided in the Appendix), and the power input probe was adjusted to optimally couple to the cavity electric field. In practice, the probe position was determined by minimizing the

reflected power level. Further detailed description of the discharge ignition and tuning process may be found in [65].

An important parameter used in determining the efficiency of a resonant cavity is the quality factor, Q, which is proportional to the ratio of time-averaged stored energy in the cavity to the power dissipated in the cavity. The cavity Q determines the maximum electric field strength in the cavity at resonance, and thus the minimum power at which a discharge can be ignited in a particular gas. Once a plasma is established in a resonant cavity, it alters the field distribution and reduces the cavity Q, since the plasma is a lossy, conductive medium. Some specific data is provided in [51] for an MPDR similar to the one used in the oxidation experiments operating in the TE_{211} cavity mode. The effect of igniting a discharge in the cavity was to shorten the electrical length of the cavity, thus the real length had to be increased in order to maintain matched operation.

3.2.3 Other Applications of the MPDR

General applications which have been investigated or proposed for large-area plasma sources such as the MPDR include ion propulsion for space vehicles [51], and industrial materials processing such as ion beam milling, ion beam etching, and plasma assisted CVD, all of which are of interest for IC processing [66,67]. Some specific applications for which the MPDR has been investigated are described here.

The performance of the MPDR as a general purpose ion source was investigated in [52], [56], and [59]. The MPDR was found to overcome problems encountered with other sources, such as low efficiency, low current density, short cathode lifetime, discharge matching, and stability. In this application, an ion beam was extracted from the microwave discharge generated in the MPDR by an accelerating grid placed below the baseplate. In a related investigation, a static magnetic field, produced by high strength rare-earth magnets, was added to the MPDR ion source and improvements in discharge breakdown, stability, and uniformity were observed [57],[61].

Another application investigated for the MPDR was its use as an ion source for ion engine [51],[52],[59]. In an ion engine, propulsion is generated by accelerating charged particles from an ion source with an electric field. The charged species are ions of a fuel gas, such as H_2, generated in a dc, rf, or microwave discharge. Potential advantages offered by the MPDR as the ion source in this application include improvement of overall system efficiency, higher ion beam densities, and longer engine life due to the absence of metal electrodes in the discharge region.

A wide range of applications for the MPDR occurs in integrated circuits processing, particularly for VLSI, where plasma processing is becoming the rule rather than the exception. For example, an investigation of plasma etching is being conducted using the MPDR [68]. Etching of Al, Si, SiO_2, and Si_3N_4 is being considered. The MPDR is expected to be used in this application to combine ion milling and reactive ion beam etching to achieve highly anisotropic etching rates, resulting in finer pattern definition. Also, it is

anticipated that the MPDR can be used for plasma assisted CVD of films such as Si and SiO_2 with applications for solar cells, microwave devices, and optical fibers, among others.

3.3 Additional Apparatus Used in the Oxidation Experiments

In addition to the MPDR, described in the previous section, the plasma oxidation experiments reported in this work required the use of a vacuum pumping station, a gas flow system, a microwave power source and transmission system, and various measurement equipment.

This additional equipment and the method of its use was, for the most part, of a fairly conventional nature. Therefore, details of the experimental apparatus and drawings of each of the major systems have been placed in the Appendix.

3.4 Experimental Parameters

This section offers a discussion of the experimental variables investigated in the oxidation experiments. These variables included microwave input power, cavity resonant mode, substrate bias, plasma pressure, oxygen flow rate, substrate mounting configuration, oxidation time, and substrate temperature. The range of study selected for each parameter is explained, and general observations are made regarding the effects of each parameter on oxide formation in the MPDR. A summary of this discussion is provided in Table 3.1.

Table 3.1. Ranges of the parameters investigated in the MPDR oxidation experiments.

Parameter Investigated	Range of Values	Comments
Microwave power	80-140 W	typically 100 W
Cavity resonant mode	TE_{211}	
Substrate bias:		
anodization potential	18-50 V	maintained constant
anodization current	10-150 mA/cm^2	maximum at t=0, monotonically decaying
Oxygen pressure	30-150 mTorr	measured downstream from plasma, constant during growth
Oxygen flow rate	5-100 sccm	adjusted for desired pressure
Substrate mounting	inside discharge zone	minimal surface damage
	15 cm below baseplate grid	streaks, lines on oxide surface-particle bombardment?
Oxidation time	18-105 min	typically 60 min
Substrate temperature	200-300 ^{o}C	estimated (see text)

3.4.1 Microwave Input Power

In the literature, microwave plasma oxidation is reported in discharges sustained at power levels ranging from about 100 W [11] to 7 kW [69]. As discussed in Section 3.2, one advantage of the MPDR is the high plasma density achieved with relatively low input power. Because of this, power levels on the lower end of this range were sufficient to generate the high plasma densities needed for oxidation. In the experiments reported here, the maximum power investigated was 140 W, which was determined by the capabilities of the power source used. Preliminary observations indicated that a stable plasma could not be sustained at power levels much lower than 80 W for the pressure range of interest, so 80 W was the minimum power investigated. Since the discharge volume was 118 cm^3, the range of power density was 0.68 W/cm^3 to 1.19 W/cm^3. In Table 3.2, this range is compared with the values of power density for some other plasma oxidation systems discussed in the literature. It might be noted here that the plasma disk diameter (about 10 cm) was considerably greater than the diameter of a sample used in the oxidation experiments (1.27 cm), and as a consequence only a fraction of the power input to the plasma was actually used to process the sample.

3.4.2 Cavity Resonant Mode

The cavity mode was considered to be an important parameter because of the possible relationship between plasma uniformity and

Table 3.2. A comparison of the values of power density in various plasma oxidation experiments.

Ref.	Input Power (W)	Excitation Frequency (MHz)	Plasma Volume (cm^3)	Power Density (W/cm^2)
[11]	1.4×10^2	2.45 GHz	1.07×10^3	0.13
[12]	6.0×10^2	2.45 GHz	1.90×10^1	31.6
[27]	3.0×10^2	2.45 GHz	3.98×10^1	7.54
[49]	1.2×10^4	1.0 MHz	1.96×10^3	6.11
[69]	4.5×10^3	0.5 MHz	5.03×10^3	0.89
[70]	1.5×10^2	2.45 GHz	9.54×10^2	0.16
This work	8.0×10^1-1.5×10^2	2.45 GHz	1.18×10^2	0.68-1.19

oxide uniformity, and because of the possibility of limiting substrate surface damage by advantageously controlling the microwave electric field direction.

In preliminary investigations, it was found that oxygen discharges were readily sustained in the TE_{211}, TE_{011}, and TM_{011} cavity modes.

In the TE_{211} mode the plasma ignited easily, remained stable over a wide range of power and pressure, and coupled well to the source (the reflected power was small). At intermediate pressures (80-150 mTorr), the TE_{211} mode discharge showed four well-defined, symmetric lobes characteristic of the electric field pattern for this mode. At lower pressures, the lobes became diffuse, the center of the discharge region filled in, and the plasma appeared to be of nearly uniform brightness.

In the TE_{011} mode, a discharge of more uniform appearance was generated over the range of pressure studied. However, the minimum reflected power was considerably higher than for the TE_{211} mode. In this mode, significant heating of sample mounted in the MPDR discharge region was observed prior to the ignition of a discharge. In the TE_{011} mode, the electric field lines in the plane of the sample are closed circles, and thus Joule heating could arise from induced currents in the substrate. Using this mode, silicon samples have been heated to more than 900 ^{o}C (cherry red) in just a few minutes with an input power of 100 W. The substrate temperature was dependent upon gas flow rate; at higher flow rates (>100 sccm) the sample was cooled below incandescence. This heating effect might be beneficial in some applications, but it was undesirable for these

oxidation studies since thermal oxidation becomes significant at substrate temperatures above about 800 ^{o}C.

The TM_{011} mode also produced a highly uniform discharge. However, in the TM_{011} mode, the cavity length required for resonance resulted in a separation between the sliding short finger stock and the power input probe in the MPDR of only about 3 mm for optimal coupling. An advantage of the short cavity length was the reduction of wall losses and an increase in the maximum electric field strength in the cavity. However, at higher power levels this mode was not useful because spontaneous arcs formed between the probe and finger stock which caused rapid metal erosion and plasma instabilities.

Based on these considerations, all of the oxidation experiments reported in this work were conducted in the TE_{211} mode of the MPDR. The ideal field patterns associated with this mode are shown in Figure 3.3. Since the plasma is confined by the lines of magnetic field, the TE_{211} discharge appears as four distinct lobes surrounding a darker center. Some measurements of the azimuthal and longtitudinal variation of electric field strength in a cylindrical cavity similar to the one used in these experiments is available in [51].

3.4.3 Substrate Bias

The substrate bias in an anodization experiment is typically maintained either at a constant current, with voltage as the dependent quantity, or at a constant voltage with the current dependent. The observed growth kinetics are different for these

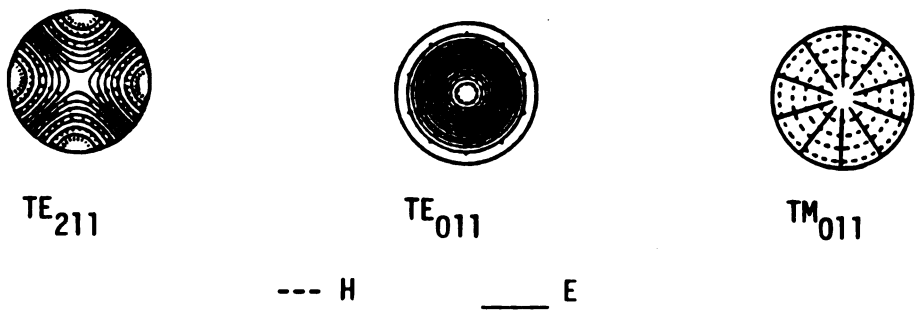

Figure 3.3. Ideal field patterns in a constant z plane of a cylindrical resonant cavity for three modes investigated in the MPDR. The density of the field lines is approximately proportional to the field strength. A discharge formed in the cavity follows the magnetic field lines, and the plasma density is greatest at locations of maximum E-field strength.

cases, as discussed further in [10]. Constant current anodization was initially considered for the MPDR experiments. However, constant bias current resulted in a steadily increasing substrate voltage, which also appeared across the space between the substrate back contact and the grounded baseplate grid (see Figure 3.2). This space was filled with the discharge gas, and a dc arc was occasionally observed to form in this space at bias voltages greater than 40 V, the precise value depending upon the pressure. Once formed, this dc discharge prevented accurate measurement of the substrate bias voltage and current. In addition, it rapidly eroded the bias contact and the bias wire, effectively destroying the sample if allowed to persist. Therefore, constant current bias was not used; constant voltage anodization was studied instead.

An additional concern related to biasing was possible sputtering of the materials exposed to the plasma [7,10,12]. Sputtering could lead to contamination of the growing oxide, and could cause the growth process to be obscured by etching and deposition. In preliminary experiments with silicon samples in the MPDR, depostion of Si compounds was observed on the quartz housing at biases above about 50 V. At higher potentials, sparks were observed near the stainless steel walls of the enclosure. Therefore, the maximum anodization potential studied in these experiments was 50 V.

Oxide formation has been observed on unbiased samples in microwave plasmas [27,33], and there are no reports in the literature indicating a specific value of negative bias at which oxidation is observed to cease. However, preliminary experiments in the MPDR indicated that oxides grown at bias voltages below about 20 V were usually thinner than 500 Å, the minimum thickness which could

accurately be measured with the facilities available. Therefore, substrate bias voltage was varied in the range of approximately 20 to 50 V.

3.4.4 Oxygen Plasma Pressure

Microwave plasma oxidation has been reported in the literature in the pressure range extending from 5×10^{-5} Torr [36] to 1.5 Torr [27]. Langmuir probe studies conducted in the MPDR by Dahimene [71] indicated that below about 30 mTorr the MPDR plasma density decreased rapidly with decreasing pressure. In addition, preliminary investigations of oxygen plasmas in the empty MPDR showed that it was difficult to sustain a stable, single-mode plasma below about 30 mTorr with the microwave power levels under consideration. Therefore, the minimum pressure investigated was 30 mTorr. In the excitation mode chosen for this work, the plasma was increasingly constrained to the walls of the enclosure as the pressure increased, and as a result the plasma density decreased in the central region of the discharge. This was confirmed by Langmuir probe data (discussed in Section 4.2) and it was consistent with the observed decrease in luminesence of the plasma as the pressure increased. Based on probe data and on visual observations of the discharge, 150 mTorr was chosen as a convenient upper cutoff pressure which was well outside the regime of large plasma density. It should be noted here, however, that higher density, uniform discharges can be generated in the MPDR at higher pressures if the input microwave power is increased.

3.4.5 Oxygen Flow Rate

The MPDR oxidation reactor was designed as a continuous flow system. High purity (99.993%) oxygen was metered to the plasma confinement region by an automatic flow control system, which could be set to provide constant pressure, constant flow, or manual flow control. Preliminary observations indicated that varying the flow at a fixed pressure (by varying the pumping speed) did not significantly affect the oxidation rate of a substrate over a wide range of flow and pressure. It might be expected that flow rate would not be important, to a first approximation, unless it became so low that the discharge was starved of the primary oxidant species. The flow rate at which this would occur was estimated by calculating the total ion flux needed to form an SiO_2 film at a specified rate. For the highest growth rate observed in the MPDR, 2500 Å in 1 h, this calculation yielded a required average O_2 molecular flux of 1.6×10^{22} $cm^{-2}s^{-1}$. For the substrate area used, 1.27 cm^2, the flow rate required to give this molecular flux was calculated to be 5.0×10^{-4} sccm. The actual flow rates measured during the oxidation experiments were in the range 5 to 100 sccm, so oxygen starvation was not a concern.

The actual flow rate used in a particular experiment was a function of the desired system pressure, the pumping speed of the vacuum pump, and the overall flow conductance of the flow system.

3.4.6 Sample Mounting Configuration

In the MPDR used in the oxidation experiments, provision was made for mounting samples either inside the discharge zone or outside, downstream from the discharge. Preliminary experiments showed that oxidation occured in either configuration, but that the oxide film quality on the downstream samples was poorer. The downstream samples showed visual evidence of streaking and apparent bombardment by large particulates (this is discussed further in Chapter Five). Therefore, most of the work reported here involved samples processed inside the discharge zone. However, during preliminary experiments in the downstream mode, a previously unreported phenomenon was observed. Under certain conditions, a secondary discharge was observed to form directly over the sample surface. The shape and intensity of this secondary discharge were coupled to the power density and pressure of the primary discharge, and also depended upon the substrate bias potential. The system operated in a dual plasma mode with a downstream hybrid plasma derived from the microwave disk plasma. The hybrid plasma was not completely a microwave plasma, rather it was a hybrid of a microwave plasma and a dc discharge since it contained species from both. This observation was pursued further in [62].

3.4.7 Anodization Time

Values of the parabolic rate constant for microwave plasma oxidation reported in the literature range from 8×10^3 Å^2/min [13] to 4×10^5 Å^2/min [27]. The corresponding range of oxide thicknesses that would be grown in one hour is approximately 1000 Å to 5000 Å. The minimum oxide thickness readily observed visually is about 500 Å, and the simple interferometry measurements available for analysis of the results reported here became imprecise below this thickness as well. Based in part upon the above data, an oxidation time of 1 h was chosen for most of the oxidation experiments.

3.4.8 Substrate Temperature

There is experimental evidence that oxidation rate increases with substrate temperature in several types of plasma reactors [7,11,13]. The substrate temperature was not investigated as an independent parameter in the oxidation experiments reported here. However, the temperature of the quartz housing in the MPDR used for the oxidation experiments was measured after several 1 h experiments, and the maximum wall temperature was 125 °C. Temperature measurements were made in a similar MPDR [71], and the temperature measured in the discharge region at the position normally occupied by a substrate was about 100 °C above that of the quartz housing. Based on these measurements, it was estimated that the substrate temperatures in the oxidation experiments ranged from 200 °C to 300 °C.

3.5 Oxidation Experiments: Experimental Procedure

Plasma oxide samples were prepared in the MPDR as anodization voltage, oxygen pressure, and microwave power were independently varied, and substrate bias current was recorded as a function of time for each experiment. After each experiment, visual and microscope observations were made, with special attention given to oxide color, uniformity, and surface degradation.

Details of the experimental procedure including substrate preparation, formation of a discharge, in-progress monitoring of the experiments, and a list of samples are given in the Appendix. However, for convenience a brief synopsis of the experimental procedure is given here.

A typical experimental substrate was a 0.254 mm thick planar n-type silicon slice, with dimensions 17.8 mm × 17.8 mm. A bias wire was attached to the substrate, and this assembly was mounted in the MPDR discharge chamber on a quartz plate so that the substrate was insulated from the MPDR baseplate. A quartz mask was placed over the substrate, which was provided with a 12.7 mm diameter circular hole to expose the substrate to the plasma.

After mounting a sample, an oxygen discharge was ignited in the MPDR, and the desired experimental conditions were maintained for the duration of the experiment (usually 60 min). At the termination of the experiment, the oxidized substrate was removed for observation and characterization, as described in Chapter Five.

Chapter Four

Experimental Characterization of Oxide Growth

4.1 Introduction

In this chapter, results of an experimental investigation of the growth of SiO_2 films in the microwave plasma disk reactor are presented and discussed. In order to make the desired correlation between plasma conditions and oxide growth, it was necessary to make a set of measurements characterizing discharges in the reactor. These measurements are reported first, in Section 4.2, since the results are used in the following sections. In Section 4.3, data are presented regarding the variation of oxide growth rate with anodization potential, oxygen pressure, and microwave power. The oxide voltage and oxide electric field are considered in Section 4.4. A method is developed to calculate estimated upper and lower bounds on the oxide field, and the variation of these quantities with voltage, pressure, and power are investigated. The major conclusions from this chapter are summarized in Section 4.5.

4.2 Plasma Probe Measurements

One of the goals of this research was to correlate oxide growth with plasma conditions. Important measurements included plasma density, n_e, and oxide surface potential, V_s. Plasma density is a measure of the degree of ionization in a discharge, and is therefore important in determining the availability of reactive species. For constant voltage anodization, the oxide surface potential determines the oxide electric field, which in turn affects transport processes in the oxide. This is discussed further in Section 4.4.

A series of double Langmuir probe measurements, discussed in 4.2.1, provided data for calculating n_e as a function of pressure and microwave input power. The large-area gilded probe measurements reported in 4.2.2 provided insight into the effects of a large area substrate on the plasma characteristics, and allowed the oxide surface potential and oxide electric field to be deduced for a sample subjected to a given set of plasma conditions. These data were also used in a model-based investigation of growth kinetics reported in Chapter Six.

4.2.1 Double Langmuir Probe Measurements

The electron density, n_e, and electron temperature, T_e, in a discharge can be deduced from the dc I-V characteristics of a double Langmuir probe immersed in the discharge [72,65]. A double Langmuir probe consists of two electrodes mounted in a fixed relationship to each other, connected by a variable voltage supply, with appropriate

each other, connected by a variable voltage supply, with appropriate instrumentation for measuring the probe current and differential voltage when the probe is immersed in a plasma. Briefly described, the principle of this measurement is that the variation of probe current with probe voltage depends upon the difference between the probe voltage and the plasma potential, which in turn is related to n_e and T_e, as well as to the ion or neutral gas temperature. In a double probe experiment, both probes are electrically isolated from the plasma enclosure, so the measured I-V characteristic depends only upon the plasma conditions, and not directly upon probe location with respect to any conducting walls. Also, the measurement is a local one in the sense that the probe field and current are confined to the plasma region in the immediate vicinity of the probes. A general discussion of plasma probe theory is available in [73].

A diagram of the experimental set-up for the double Langmuir probe measurements reported here is provided in Figure 4.1. Also shown in this Figure is a drawing of the double probe, with dimensions. The probe used in these experiments consisted of two tungsten wires encased in glass, except for the tips. The wires were round in cross section, with a diameter of 0.25 mm. The wires were spaced 3 mm apart, and the exposed tips were 3.56 mm long. The total exposed surface area per probe was 2.8×10^{-2} cm^2.

The double probe measurements were made in oxygen discharges formed in an empty reactor (i.e., without a sample in place). The double Langmuir probe I-V characteristics of a discharge in the MPDR were measured, for a given combination of microwave power and plasma pressure, by sweeping the probe voltage across its range (typically -40 V to +40 V) while recording the probe current and voltage. In

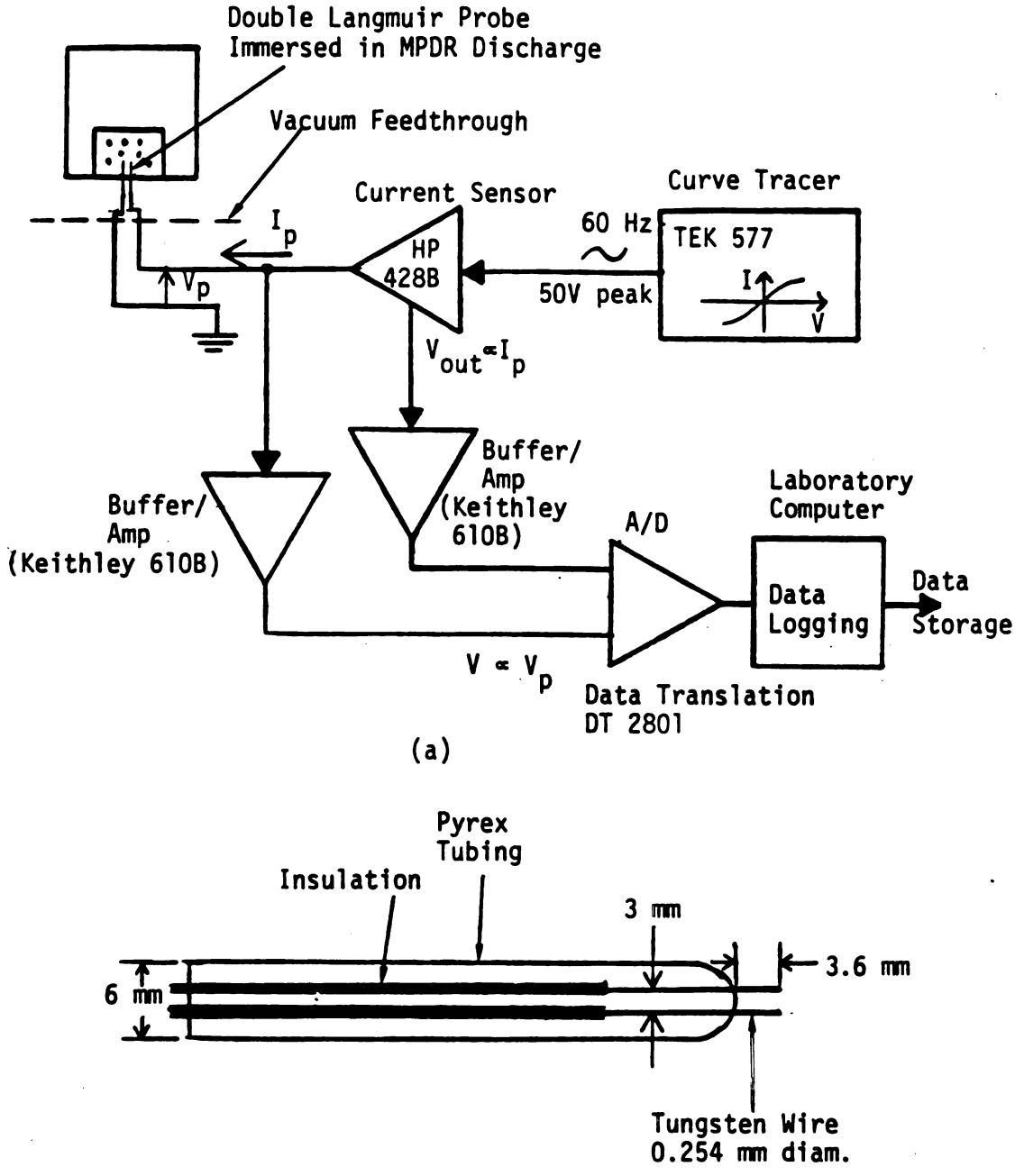

Figure 4.1. (a) Instrumentation used in the double Langmuir probe measurements. A similar set-up was used for the gilded probe measurements. (b) Details of the double Langmuir probe used in this work.

order to ensure that the plasma conditions did not vary during an I-V sweep, the sweep generation and data logging functions were performed as rapidly as possible. A curve tracer was used to generate a ground-referenced 60 Hz bipolar sinusoidal voltage sweep while providing a real-time display of the probe current-voltage characteristics. High speed data logging was accomplished by use of an A/D converter connected to the laboratory computer system. Probe voltage and current were recorded during the duration of one complete cycle of the 60 Hz source. The data were numerically averaged to eliminate hysteresis resulting from the probe capacitance, and interpolation was used to compensate for the staggering of current and voltage readings (with the instrumentation available, the current and voltage could not be recorded simultaneously). The curve tracer and the computer-related instrumentation were necessarily referenced to earth-ground, so that in order to isolate the double probe from the plasma confinement walls it was necessary to isolate the MPDR cavity and baseplate from earth ground. For this purpose, the MPDR external connections were temporarily modified for the probe measurements as follows. A coaxial radial choke assembly designed for 2.45 GHz was inserted between the microwave power input cable and the cavity input probe, providing dc isolation from the outer conductor of the coaxial cable. A short length of teflon tubing was inserted in the stainless steel gas input line. Distilled cooling water was supplied by gravity flow from a 10 gal plastic bottle and drained into another plastic bottle. After these modifications were made, there was a small residual conductivity to earth ground when a discharge was present in the MPDR. This conductivity was evident as an asymmetry with respect to the origin in the double probe I-V

characteristics, and was probably due to charge transported by flowing ionized gas to the grounded surfaces of the vacuum system. However, the resulting leakage current (usually several μA) was less than 1 percent of the typical probe saturation current, and thus was considered negligible.

I-V measurements were made using the double Langmuir probe in discharges at power and pressure levels corresponding to those studied in the oxidation experiments, and some of the resulting I-V curves are shown in Figures 4.2 and 4.3. The origin of the general form of these curves is explained in [72]. A knee voltage and current can be defined for each curve, and for voltages above the knee voltage, the characteristic can be said to be saturated. The true saturation current is the positive ion current collected by the probe at the lower potential. The current in the intermediate voltage region is the sum of the electron and positive ion currents to the probes, and for low voltages is mainly due to electrons. It is generally assumed for the purposes of analysis that the total positive ion current to the probes is unaffected by the applied probe potential.

Figure 4.2 shows the effect on the measured probe characteristics of varying the plasma input power, and Figure 4.3 shows the effect of varying the plasma pressure. At any voltage in the saturation region the probe current decreased monotonically with increasing pressure in the range 40 to 150 mTorr, and increased with increasing power in the range 80 to 110 W. Details of the data reduction method used to get T_e and n_e from the I-V characteristic are provided in [72], but, roughly speaking, T_e increases with the slope of the I-V characteristic between the saturation regions, and

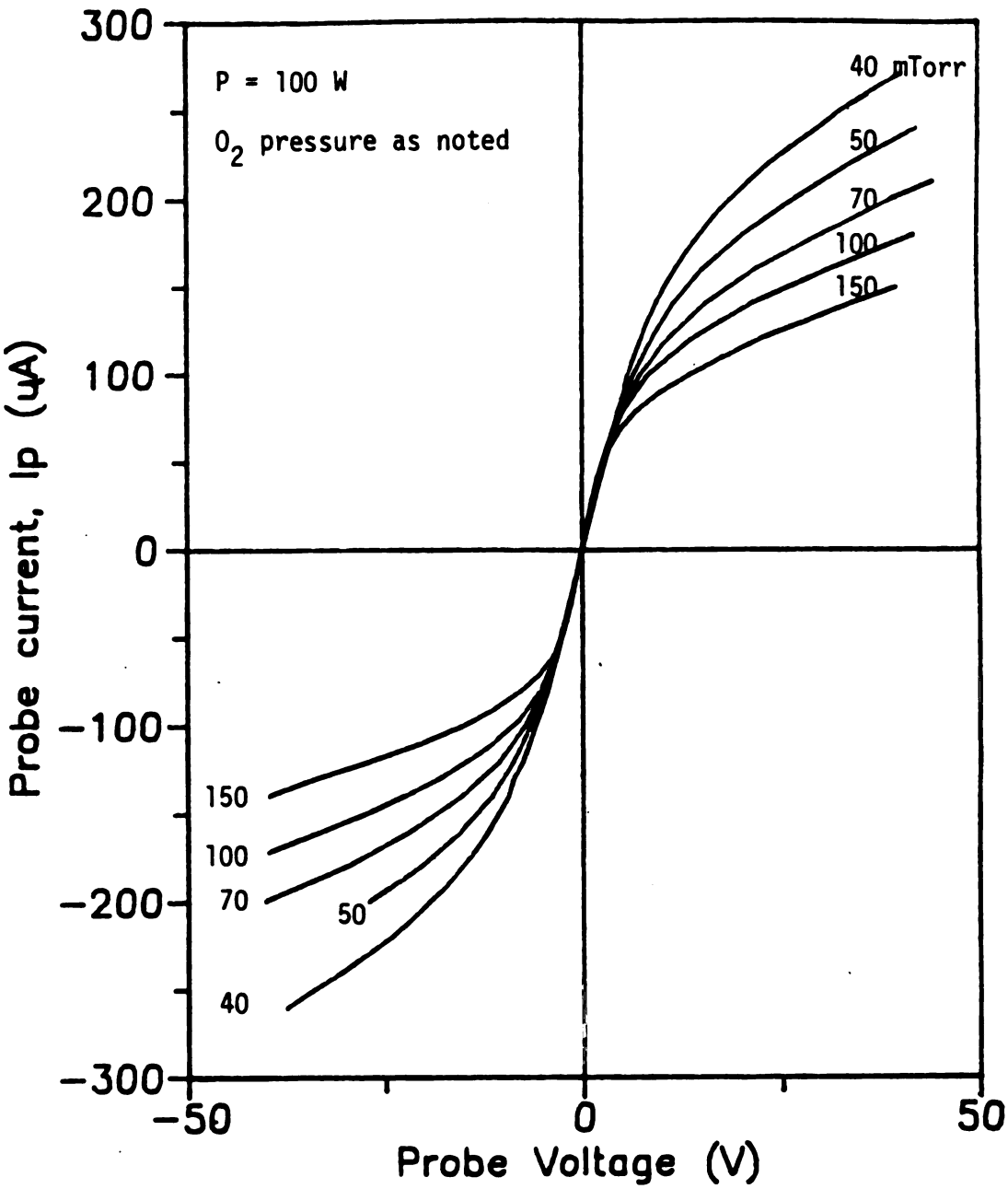

Figure 4.2. Double Langmuir probe I-V characteristics measured in a TE_{211}-mode oxygen discharge in the MPDR with 100 W microwave input power, with oxygen pressure as a parameter.

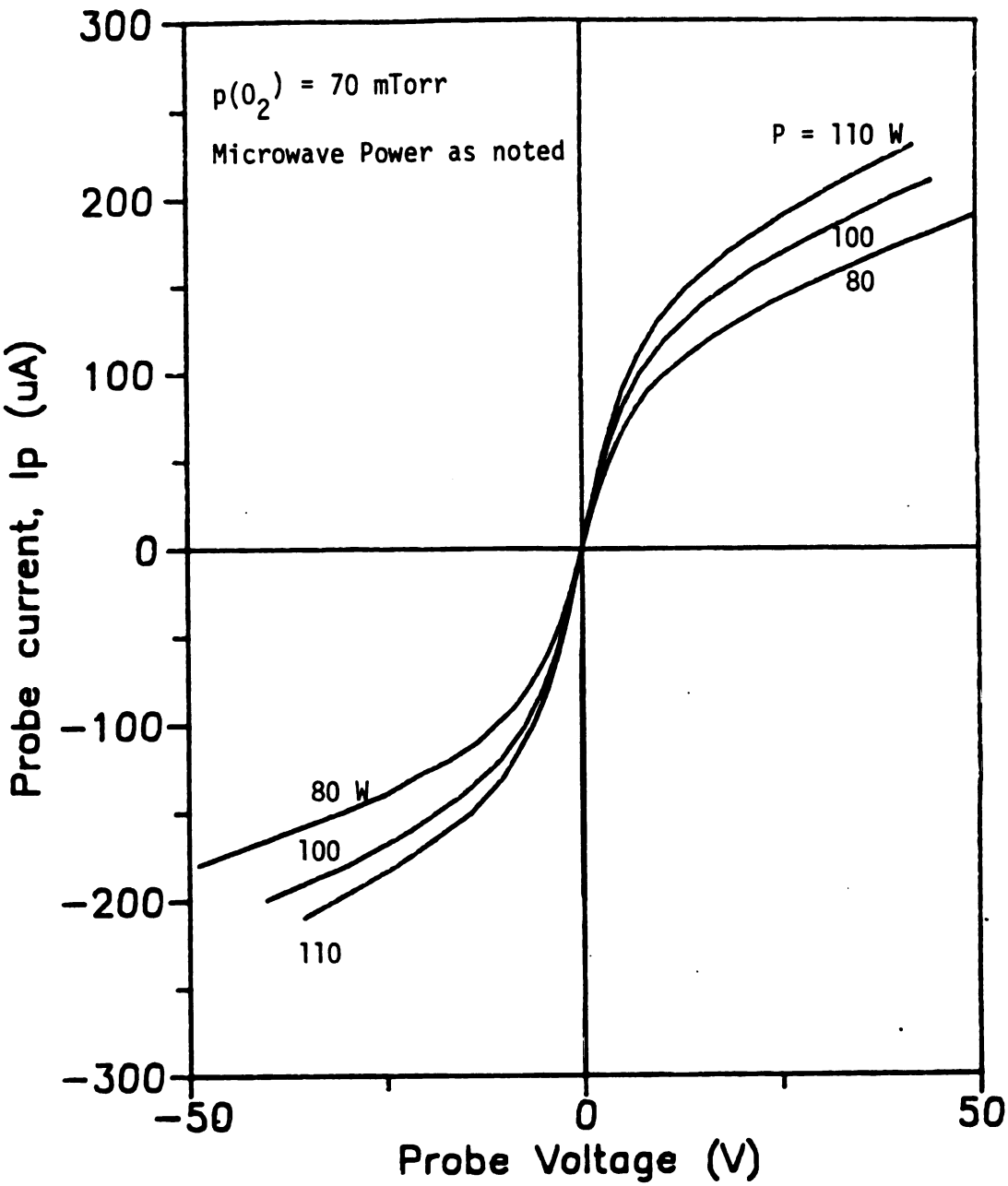

Figure 4.3. Double Langmuir probe I-V characteristics measured in a TE_{211}-mode oxygen discharge in the MPDR at 70 mTorr oxygen pressure, with microwave power as a parameter.

n_e increases with saturation current. The data reduction method described in [72] was implemented on a laboratory computer system. Values of plasma density extracted from double Langmuir probe measurements in the MPDR are plotted in Figure 4.4 as a function of plasma pressure, with input power as a parameter. It is evident from this Figure that n_e decreased with increasing pressure over the entire pressure range studied, for each value of microwave power. Also, for each value of pressure above 40 mTorr, n_e increased with microwave power. The plasma density ranged from 4.6×10^{11} cm^{-3} at 80 W, 150 mTorr to 1.5×10^{12} cm^{-3} at 110 W, 30 mTorr. During the experiments, when the plasma pressure was reduced to about 45 mTorr at 80 W, the plasma mode shifted from TE_{211} to an asymmetrical, possibly hybrid mode, so the data point at 40 mTorr and 80 W is shown only for the sake of completeness. Values of n_e and T_e calculated from the double Langmuir probe I-V characteristics are listed in Table 4.1. These data correspond well with the measurements of Dahimene [71], which were made under similar conditions in a different reactor.

The double Langmuir probe measures electron density, but of particular interest for silicon oxidation is the density of negative oxygen ions which can be generated in a discharge. According to Sabadil and Pfau [74], in an dc oxygen discharge under low current extraction conditions the density of O^- ions has the same order of magnitude as n_e. Under this condition, charge neutrality would require the positive ion density, n_p, to satisfy $n_p \approx 2n_e$, which is contrary to the usual assumption that $n_p \approx n_e$. The case for a microwave discharge might be considerably different, but this is a topic which warrants further study.

Table 4.1. Values of plasma electron density, n_e, and electron temperature, T_e calculated from double Langmuir probe I-V characteristics in a TE_{211} mode discharge in the MPDR.

Plasma Pressure (mTorr)	Microwave Power (W)					
	80		100		110	
	n_e †	T_e ††	n_e	T_e	n_e	T_e
30	____	____	____	____	1.46	4.60
40	1.31	4.52	1.24	3.14	1.40	3.79
50	1.09	3.55	1.03	2.99	1.25	3.61
60	0.895	3.22	1.12	3.44	1.13	3.18
70	0.819	3.04	1.02	3.09	1.14	3.06
80	0.766	2.85	0.977	2.94	1.01	2.53
90	0.641	2.24	0.938	2.72	____	____
100	0.630	2.29	0.931	2.61	0.959	2.35
150	0.462	1.67	7.50	2.00	0.827	1.99

† The units of n_e are 10^{12} cm^{-3}.

†† The units of T_e are 10^4 ^oK.

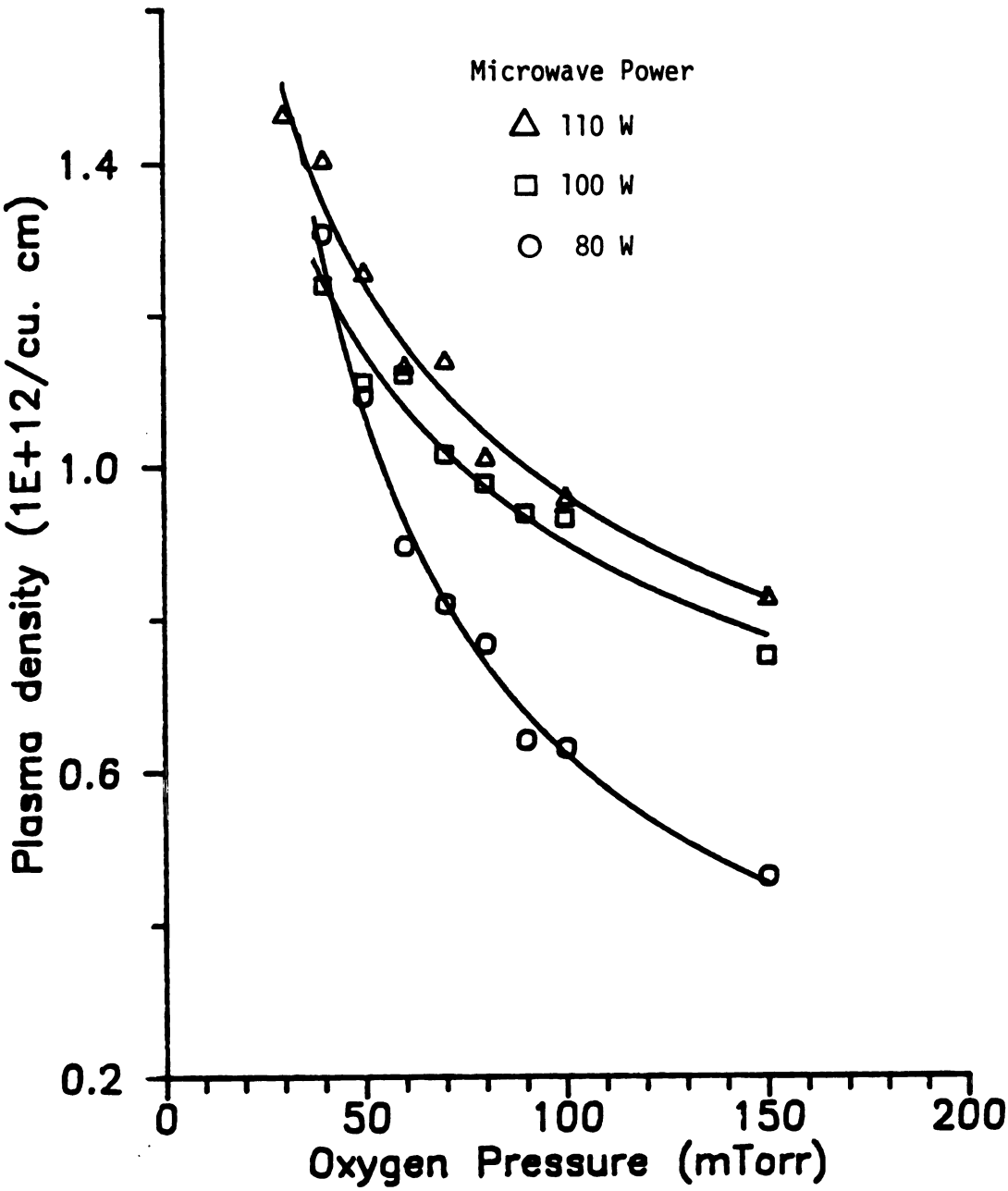

Figure 4.4. Plasma electron density, n_e, in a TE_{211}-mode oxygen discharge in the MPDR as a function of oxygen pressure, for several values of microwave power. The data points were calculated from the double Langmuir probe I-V characteristics shown in Figures 4.2 and 4.3

4.2.2 Gilded Probe Measurements

The double Langmuir probe measurements discussed in 4.2.1 were conducted in an MPDR discharge with no substrate installed, and therefore they did not accurately reflect the plasma conditions in the presence of a substrate. In order to provide more insight into the plasma characteristics and the plasma-substrate interactions with a sample in place, a series of experiments was carried out along the lines of the gilded-probe experiments described in [50]. A probe was used that consisted of a silicon substrate, identical to those used in the oxidation experiments (substrate dimensions are given in Section 3.5), with a 400 Å layer of gold evaporated onto the top surface. The gold prevented oxidation of the silicon substrate, so the probe I-V characteristics could be measured directly. I-V characteristics were measured for discharges under a variety of conditions in the MPDR using this large-area (1.27 cm^2) gilded probe. In order to determine the oxide surface potential during anodization, these measurements were correlated with measurements of substrate anodization current J_a taken during the oxidation experiments, as described in detail in Section 4.4. The results of this correlation are presented in Section 4.3.

Figure 4.5 shows the gold probe I-V characteristics of a TE_{211} mode discharge in the MPDR at 100 W microwave input power for several pressures in the range 30 to 150 mTorr. Figure 4.6 shows the I-V characteristics at 50 mTorr for 100 W, 120 W, and 140 W input power. Only the positive voltage region of each characteristic is shown; in

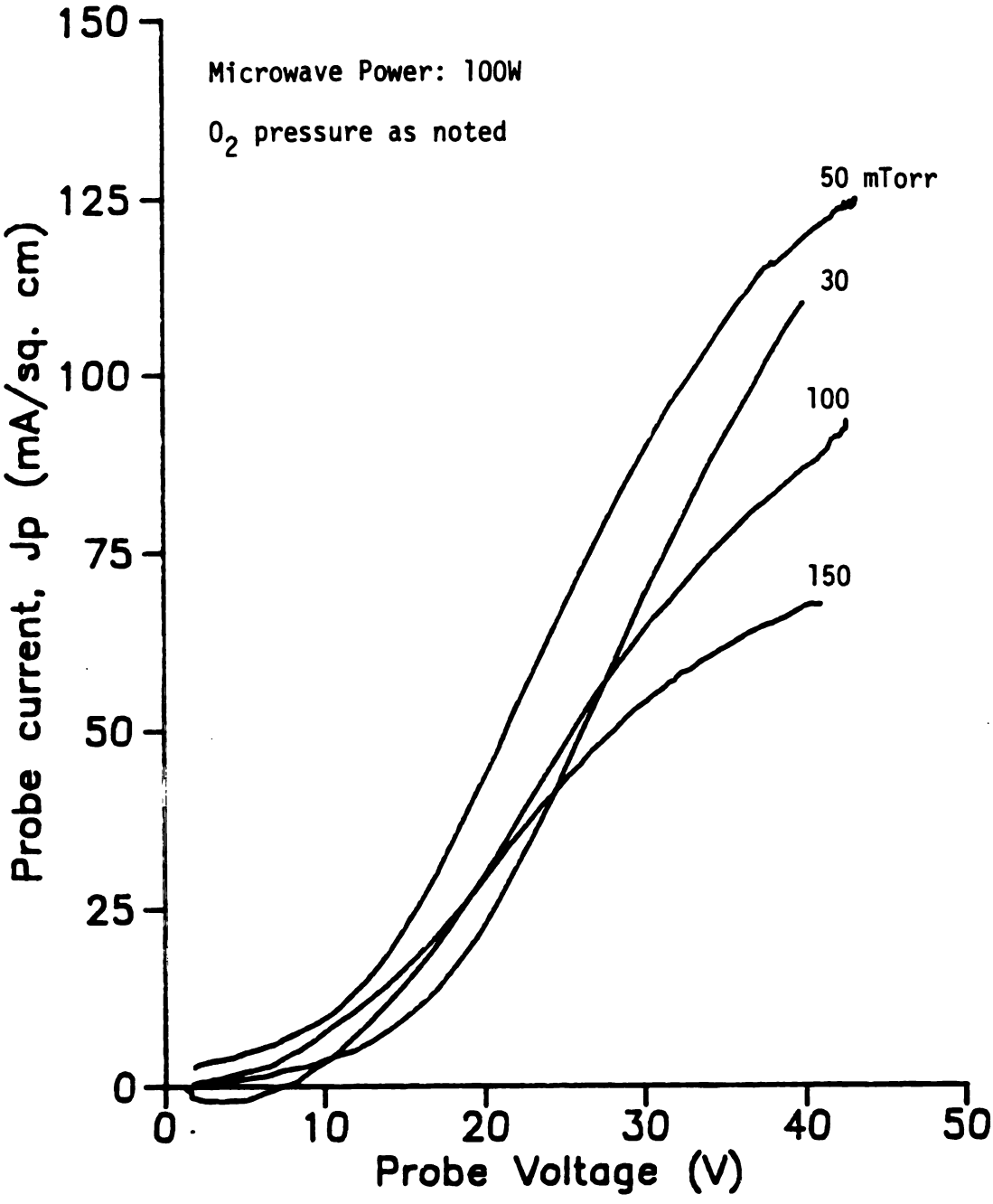

Figure 4.5. Gilded probe J-V characteristics in a TE_{211}-mode oxygen discharge in the MPDR with 100 W microwave power, with oxygen pressure as a parameter.

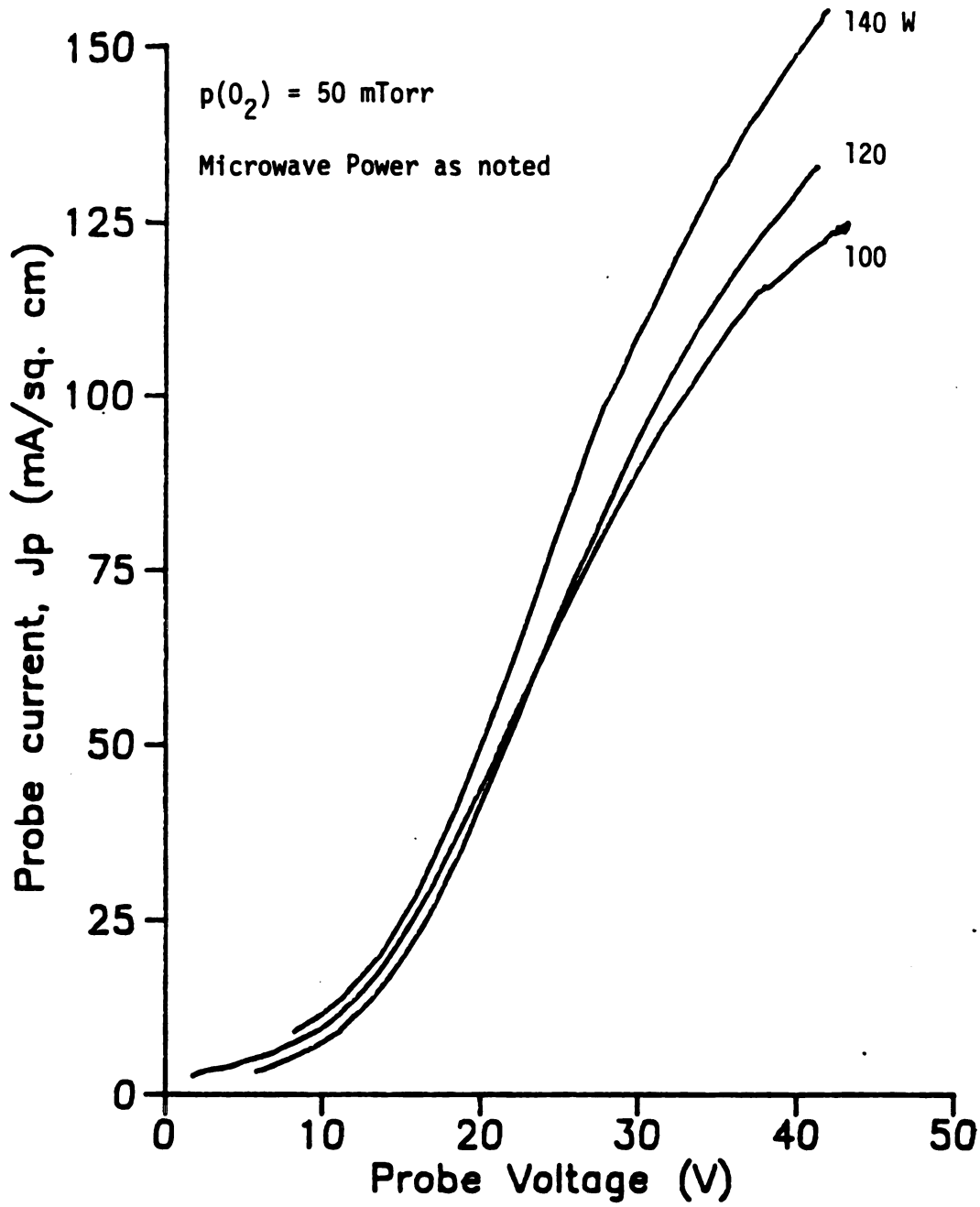

Figure 4.6. Gilded probe J-V characteristics in a TE_{211}-mode oxygen discharge in the MPDR at 50 mTorr, with microwave power as a parameter.

every case the magnitude of the current for negative voltage was below the resolution of the instrumentation (about 2 μA). The upper limit of each curve was the maximum potential which could be applied before dc arcing was observed to occur in the plasma. The general form of these characteristics is typical of large-area probes in that they exhibit a very gradual transition from the regime dominated by electron current to the saturation regime, i.e., there is not a well-defined saturation knee. However, it is possible to identify a knee voltage and a knee current by the method discussed in [72], and to consider the saturation regime to be that for which $V > V_{knee}$. The typical knee current for this probe is three orders of magnitude greater than for the Langmuir probe discussed in 4.2.1 (although the surface area area of the gilded probe exposed to the plasma is only about 20 times that of the double Langmuir probe). It is noteworthy that in Figure 4.5 the saturation current density for the large-area probe exhibits a peak at 50 mTorr, a feature which was not evident in the Langmuir probe measurements, indicating the qualitative difference in discharge properties induced by the presence of a substrate and the extraction of a relatively large current from the discharge. The general features evident from Figure 4.6 are that the knee current increases with power and that increasing the probe voltage has the effect of amplifying the dependence of current upon power. Table 4.2 lists the values of power and pressure studied in the gilded probe experiments, and gives the maximum probe current and voltage measured under each set of conditions. In Section 4.3, these values are compared with the values of initial anodization current measured in the oxidation experiments.

Table 4.2. Values of maximum probe voltage, V_{pmax}, and maximum probe current density, J_{pmax}, measured in the gilded probe experiments.

Plasma Pressure (mTorr)	Microwave Power (W)					
	100		120		140	
	V_{pmax}†	J_{pmax}††	V_{pmax}	J_{pmax}	V_{pmax}	J_{pmax}
30	40.0	110				
40	42.7	114				
50	43.4	125	41.4	133	42.0	155
60	42.7	114				
70	42.4	103				
100	42.6	93				
150	40.9	67				

† The units of V_{pmax} are volts.

†† The units of J_{pmax} are mA/cm^2.

From the measurements reported here, it can be deduced that the oxide surface potential V_s for a sample undergoing anodic oxidation can be a significant fraction of the anodization potential V_a applied to the substrate. For example, a typical set of anodization conditions is anodization voltage V_a = 30 V , anodization current J_a = 50 mA/cm^2, and input power P = 100 W. The data in Figure 4.5 indicate that for these values of current and power, V_s would range from 22 V at 50 mTorr to 28 V at 150 mTorr. The extraction of V_s form the gilded probe data is described in more detail in Section 4.4

4.3 Results of the Oxidation Experiments

In this section, oxide growth in the MPDR in the TE_{211} mode is correlated with the principal experimental parameters: substrate bias, microwave power, and plasma pressure. In 4.3.1, some general features of the oxide growth process are discussed. In subsequent paragraphs, results are correlated with specific experimental parameters. Some of the material in this section was reported in [75].

4.3.1 General Features of the Oxidation Process

Anodic oxidation of silicon substrates in the MPDR was observed to occur within the entire range of experimental parameter values given in Table 3.1. While there were significant effects on oxidation rate and other growth-related processes as the experimental

parameters were varied, there were some features common to most or all of the samples studied. The anodization current was on the order of 10^2 mA/cm^2, from which it can be deduced that the ion current efficiency (also called the Faraday efficiency) was very low. If the anodization current were almost entirely ionic ($\eta = 1$), as is reported to be the case in liquid electrolytic anodization of Si and some other materials, the oxidation rate corresponding to a constant current of 10^2 mA/cm^2 would be about 1350 Å/s, which is far greater than observed experimentally, and is also orders of magnitude greater than the value of 2.78 Å/s given as the reaction rate-limited thermal oxidation rate in dry oxygen at 1200 ^{o}C (some values of thermal oxidation rate constants are given in Table 2.1). This calculation was based on the assumptions that O^- was the oxidant species, all ions were incorporated in the growing oxide film, and the SiO_2 molecular density is 2.3×10^{22}. An estimate of the ion current efficiency for anodic oxidation in the MPDR based on experimental data was given in [75], and resulted in values of η ranging from 3.4×10^{-4} to 5.4×10^{-4}. The low value of ion current efficiency had several implications for interpreting the results of the oxidation experiments. First, the oxidation rate could not be determined directly from measurement of the anodization current, because the variation of the ion current corresponding to the growth process was masked by the electron current. Second, the observed behavior of the anodization current was expected to be primarily determined by the oxide electric field, perhaps through a standard insulator conduction mechanism such as Frenkel-Poole emission or tunneling (for thin oxides), although perhaps through other as-yet undetermined processes. The latter is a distinct possibility since not much is

known about the properties of the oxide film during growth. Finally, a variety of chemical reactions (e.g., electron attachment to adsorbed molecular oxygen, or activation of various species) were considered likely as a result of the large amount of energy incorporated into the substrate-oxide system by the electrons.

The substrate anodization current was recorded as a function of time for each sample. Figure 4.7 shows several anodization current vs. time curves recorded for experiments conducted under various conditions. (Each of these curves is drawn through approximately 60 data points. No attempt was made to smooth the curves for plotting: the curves simply connect the data points. The random fluctuations in the curves are mainly due to minor microwave power source instabilities and oxygen pressure variations which occurred during the experiments.) Inspection of these curves reveals some general features which are typical of most of the samples studied. In most cases, the anodization appears to have occured in two stages: a rapid initial growth stage lasting several minutes, followed by a slower growth stage lasting for the remainder of the experimental duration. For higher anodization potentials, in the range 40 to 50 V, a saturation-like behavior was often observed during the initial few minutes of anodization.

The second stage was usually distinguished by a relatively smooth monotonic decay, in many cases nearly linear over the majority of the experimental duration, and in this stage, the slopes of the best linear approximations to the curves tended to become more negative with increasing anodization potential.

Anodic film growth is often characterized by an initial reaction-rate limited linear growth phase, followed by a growth phase

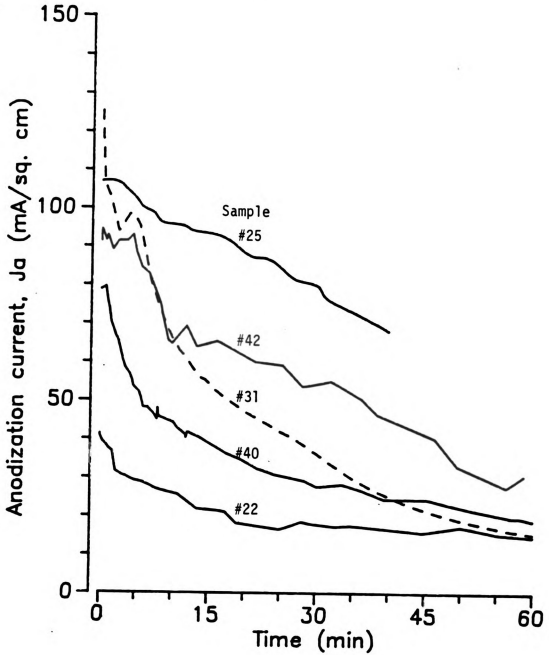

Figure 4.7. Anodization current vs. time for oxide films grown in the MPDR under various conditions (preparation conditions are given in the List of Samples in the Appendix). Curve for sample #31 is dashed for clarity.

in which the rate-limiting mechanism is the rate of oxidant transport through the film. In many cases of interest, the transport-limited growth results in nearly parabolic growth, characterized by a "migration coefficient" [47]. The transition between reaction rate-limited growth and transport-limited growth can only be determined by detailed measurement of the growth kinetics. However, it seems worthwhile to consider the possibility that such a transition occurred at some time during the film growth for the samples in this work. It might be that the observed two-stage behavior of the anodization current was related to the existence of these two distinct growth mechanisms, although further investigation would be required to determine the validity of such a correlation.

Values of the parabolic oxidation rate constant, k, for the samples grown in the MPDR were calculated from the final oxide thickness, x_{ox} and the oxidation time, t_{ox} by using the expression

$$k = \frac{(x_{ox}^2 - x_i^2)}{t_{ox}}$$

in which a value of 50 Å was used for the initial oxide thickness, x_i. These calculations were performed for the purpose of comparing oxidation rates in the MPDR with those reported in the literature for other plasma oxidation methods and for thermal oxidation. The calculated values of k for the samples prepared in the MPDR plasma oxidation experiments ranged from 4.2×10^3 Å^2/min to 8.1×10^4 Å^2/min. Parabolic rate constants reported in the literature are summarized and compared with those found in the MPDR oxidation experiments in Table 4.3.

Table 4.3. A comparison of values reported for the parabolic rate constant, k, in the plasma oxidation (anodization) of silicon.

Source	k ($Å^2$/min)	Oxidation Conditions
Ref. [7]	1.4×10^6	J_a=30 mA/cm^2, P=1kW, f=240kHz, p=0.2 Torr, T_s=600 C.
Ref. [11]	1.7×10^3	V_a=0, P=140W, f=2.45GHz, p=8×10^{-5}Torr, T_s=640 C
Ref. [12]	1.3×10^6	V_a=50V, P=600W, f=2.45GHz, p=150 mTorr, T_s < 500C.
Ref. [13]	7.8×10^3 - 3.4×10^4	V_a=100V, P=200W, f=2.45GHz, p=100mTorr, 300 C<T_s<400 C
Ref. [14]	2.5×10^4	J_a=35 mA/cm^2, P≈600W, f=dc, p=70 mTorr, T_s=225 C.
Ref. [27]	6.4×10^4 - 4.9×10^5	V_a=0, P=300W, f=2.45GHz, p=0.5-1.5 Torr, T_s≈300 C.
Ref. [31]	3.3×10^4	V_a=0, P=1kW, f=3MHz, p=30 mTorr, T_s=540 C.
Steam thermal oxidation (Ref. [1])	6.7×10^5 - 1.5×10^6	p=760 mTorr, T_s = 1000 C - 1200 C
This work	4.2×10^3 - 8.1×10^4	20<V_a<50V, P≈100W, f=2.45GHz, 30<p<150 mTorr, T_s<300 C.

V_a = constant anodization potential
J_a = constant anodization current
P = discharge input power
f = excitation frequency
T_s = substrate temperature
p = ambient O_2 (or steam) pressure

4.3.2 Correlation with Anodization Potential

Figure 4.8 shows the observed dependence of oxide thickness upon anodization potential, for 1 h oxidations at a fixed input power level of 100 W, at pressures of 40, 70 and 100 mTorr. In this Figure, the data points are fit by a straight line at each pressure, and the slopes of the best fit lines increase with pressure. The observed linear dependence is consistent with other reported results [44,28]. The physical origin of the linear dependence is presently unclear, however, it is successfully predicted by the high-field discrete hopping model studied in Chapter Six (i.e., see Figure 6.3), which also predicts an increase in the slope of the linear fit as the concentration of oxidant ions at the oxide-plasma interface increases.

Figure 4.9 shows oxide thickness plotted against initial anodization current density. All of the samples prepared in the oxidation experiments for which reliable measurements of final oxide thickness could be obtained are represented in this Figure. A best fit line is drawn through the data; this line has an intercept of 16 Å at zero current. It is evident that while there is a general tendency for oxide thickness to increase with initial anodization current, the correlation is weak. A correlation between initial anodization current and oxide thickness might be expected if the initial current is taken to be indicative of the general condition of the discharge, i.e., the degree of dissociation and energy of the electrons and reactive species. However, the fact that the correlation is weak is not unexpected since, as discussed earlier,

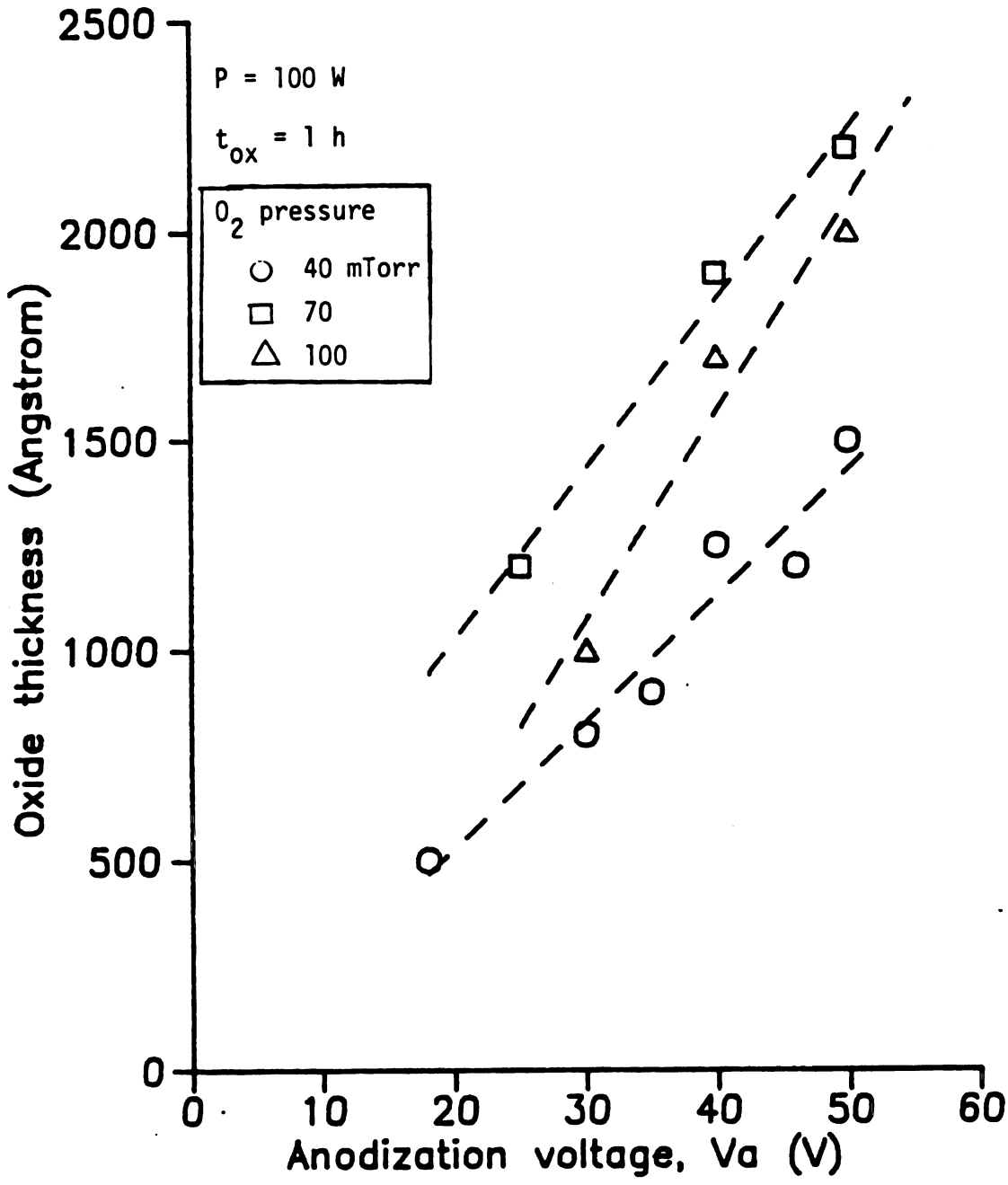

Figure 4.8. Oxide thickness grown in one hour in the MPDR as a function of anodization voltage, with oxygen pressure as a parameter. Dashed lines indicate best linear fit to the data at each pressure. Microwave power is 100 W.

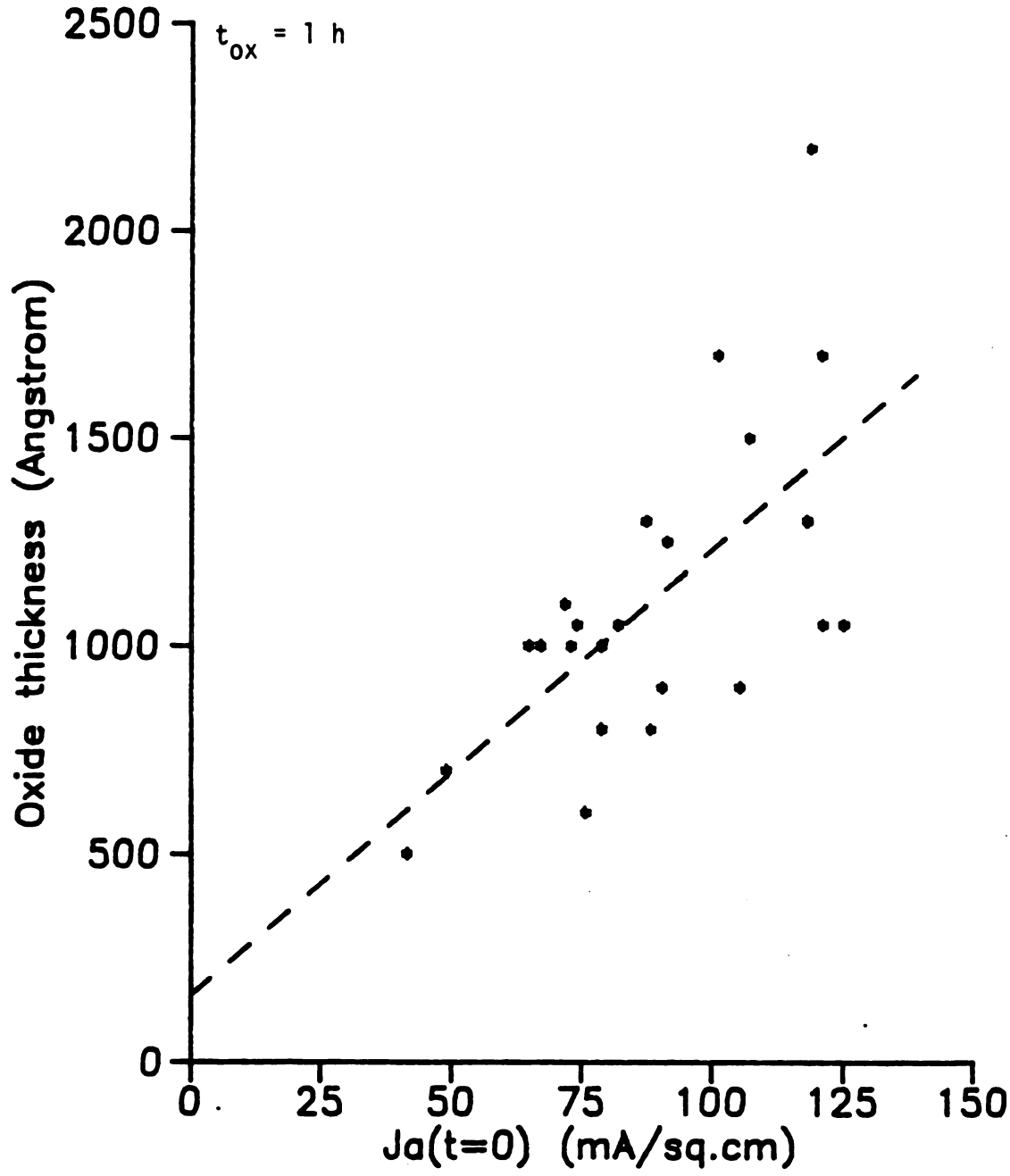

Figure 4.9. Relation of oxide thickness grown in one hour to initial anodization current. Each data point represents a sample prepared in the MPDR oxidation experiments; a wide range of preparation conditions are represented.

the measured anodization current is predominantly due to electrons, and the current due to the oxidant ion flux was not separately observed.

In Figure 4.10, the substrate anodization current curves are compared for five samples prepared at 40 mTorr and 100 W with anodization potentials ranging from 18 V to 50 V. From this Figure, it can be seen that anodization current increased significantly with anodization voltage. Also, the order of the curves is maintained throughout the experimental duration (i.e., the curves do not cross). The 18 V and 30 V curves appear to approach a zero-slope limit; this behavior is similar to that observed for anodization under conditions of relatively low surface concentration, such as in conventional liquid anodization [2]. The 18 V, 30 V, and 35 V curves show clearly an initial rapid decay stage. The 40 V curve shows an initial plateau (0 min - 5 min) followed by a brief rapid decay stage (5 min - 10 min). For the 50 V curve, a plateau is evident for approximately the first 3 min, but a rapid decay stage is noticeably absent. The form of the curves resulting from anodization at lower voltages is similar to that predicted by the modeling results in Chapter Six (i.e., see Figures 6.2(b), 6.4(b)), and may be considered to arise from high-field transport of oxidant ions across the growing oxide film in the presence of space-charge. It may be speculated that the plateau which occured for the 40 V and 50 V curves was due to a charge-supply limitation imposed by the plasma; this would be consistent with the fact that the saturation voltages of the gilded-probe plasma I-V characteristics, V_{pmax}, (listed in Table 4.2) are very close to 40 V.

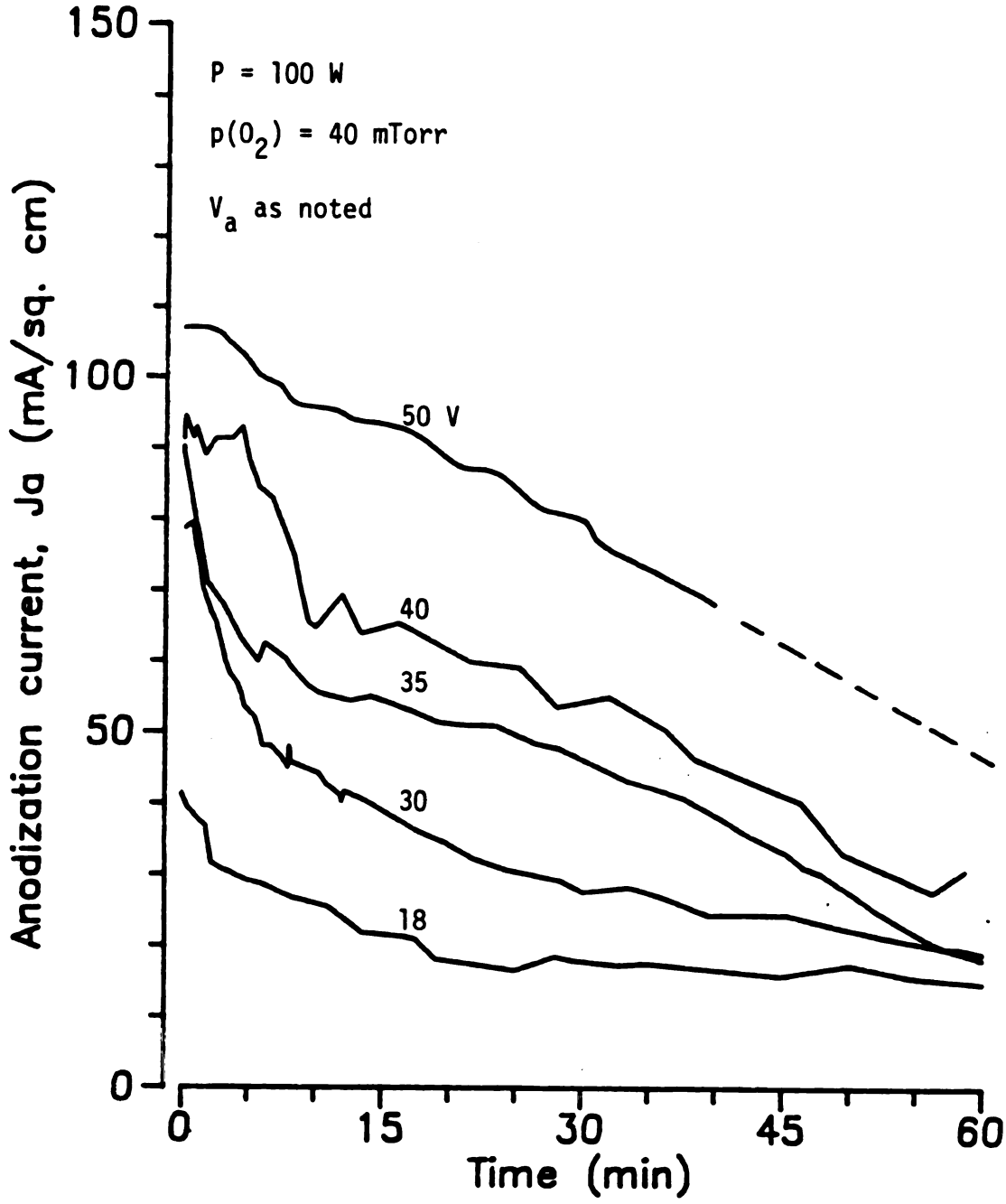

Figure 4.10. Anodization current vs. time with anodization voltage as a parameter. Microwave power = 100 W, oxygen pressure = 40 mTorr.

4.3.3 Correlation with Microwave Power

Most of the oxide samples studied were prepared with 100 W microwave input power. However, two samples were prepared at higher power levels. The resulting oxide thickness values are shown in Table 4.4, and anodization current curves for these samples are shown in Figure 4.11. Data for a sample prepared under the same conditions at 100 W are shown for reference. For convenience, the samples are referred to as A (140 W), B (120 W), and C (100 W).

Table 4.4. The effect of microwave input power on oxide thickness. For each sample, t_{ox} = 60 min, O_2 pressure = 50 mTorr, and V_a = 30 V.

Sample #	Microwave Power (W)	Oxide Thickness (Å)
31 (A)	140	1050
32 (B)	120	900
41 (C)	100	1050

From Table 4.4, it can be seen that oxide thickness formed in 1 hour was not strongly correlated with microwave power in the range studied. To the extent that the total bias current was indicative of the relative growth rate, it can be surmised from the data in Figure 4.11 that the initial growth rate was an increasing function of microwave power (J(0) increased from 81.9 mA/cm^2 for C to 125 mA/cm^2 for A), but that after a certain growth time had elapsed, the growth

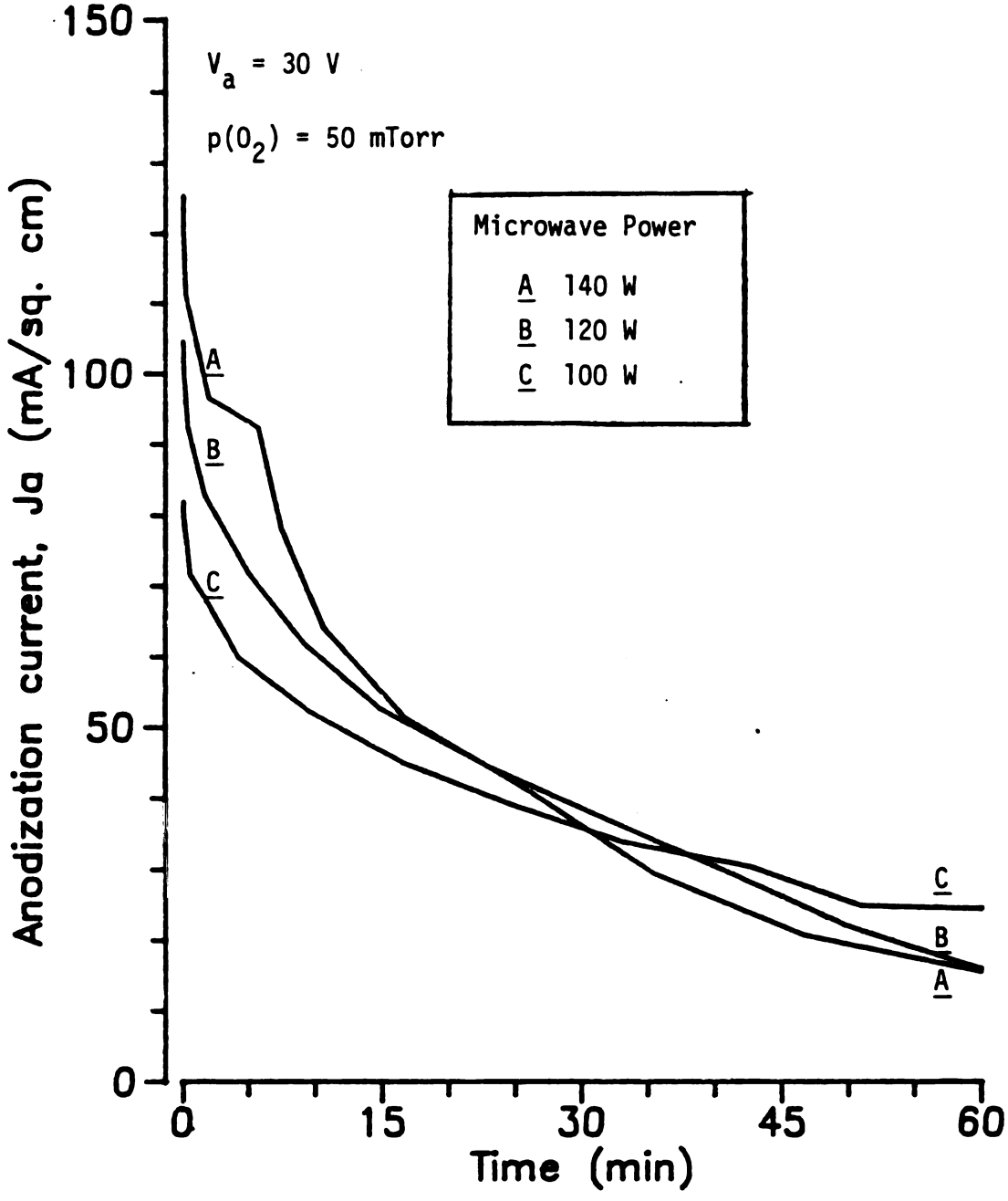

Figure 4.11. Anodization current vs. time at several values of microwave power. A, B, and C are the same samples listed in Table 4.4.

rate order was reversed, with the higher power samples exhibiting the lower growth rate. This indicates that at higher power levels, the initial oxidation rate was greater, as expected due to the increased plasma density, but the oxidation rate subsequently decreased more rapidly because the oxide formed more quickly.

The final bias current densities in Figure 4.11 were 15.5 mA/cm^2 for A, 15.9 mA/cm^2 for B, and 24.4 mA/cm^2 for C. After the end of the 60 min oxidation period, oxides A and B were only slightly thicker than oxide C, but the electron current in A and B was about half that in C, in spite of the fact that B was in a higher power plasma. This may be consistent with other evidence of highly nonlinear electron conduction mechanisms in SiO_2, but this phenomenon requires further investigation.

The reversal of the growth rate order during the anodization could account for the lack of correlation between oxide thickness and microwave power over the time interval studied, and leaves open the possibility that the lack of correlation was an artifact of the particular duration chosen for these experiments.

4.3.4 Correlation with Plasma Pressure and Plasma Density

In Figure 4.12, oxide thickness grown in 1 hour is shown as a function of plasma pressure for anodization potentials of 30 V and 40 V. Several anodization current curves are plotted in Figure 4.13 for anodization potentials of 30 V and and 40 V. Figure 4.12 shows that the oxide thickness is broadly peaked around 70 mTorr for each value of substrate bias, while Figure 4.13 indicates a rather weak

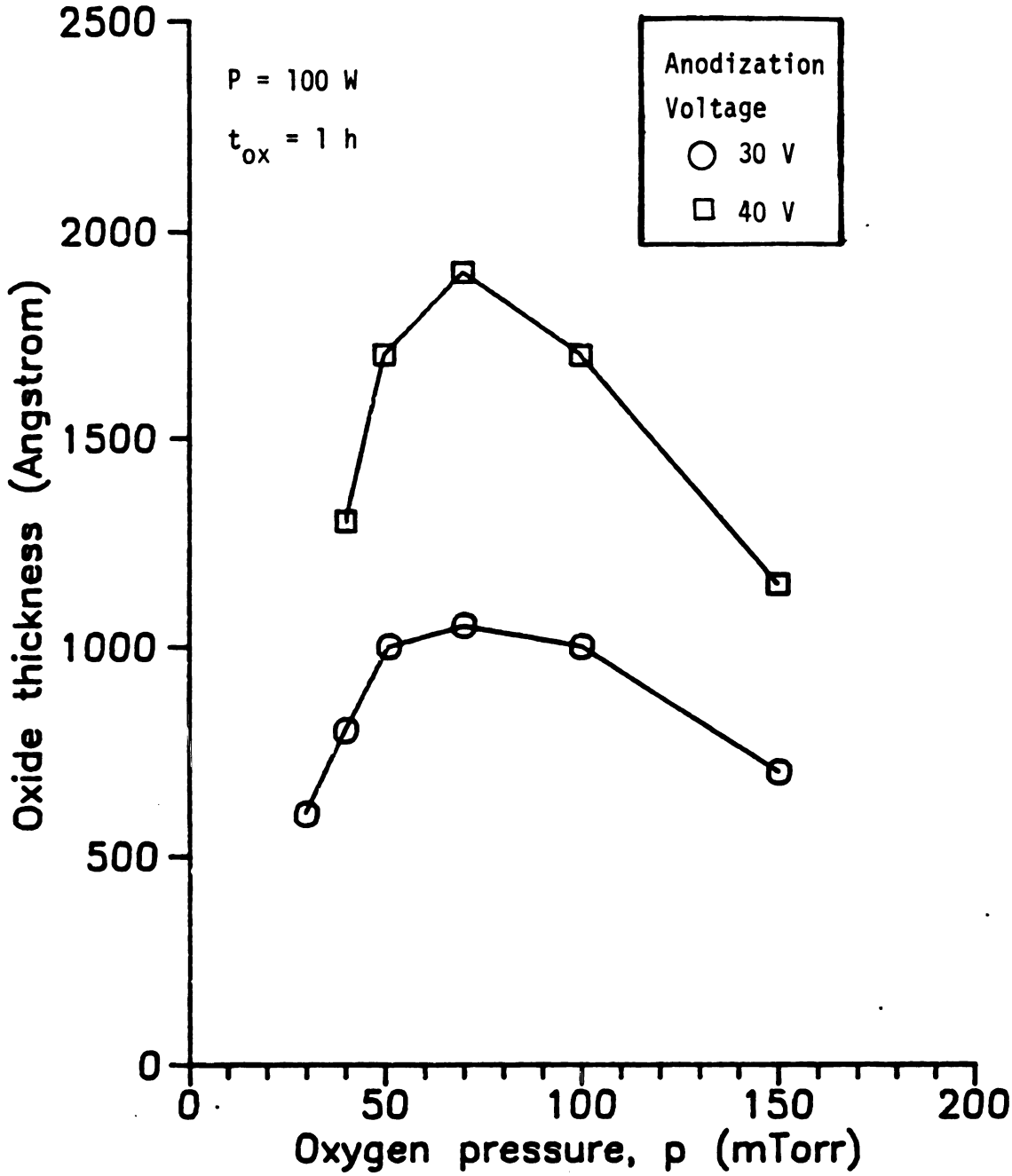

Figure 4.12. Oxide thickness grown in one hour as a function of oxygen pressure, for V_a = 30 V and V_a = 40 V. Microwave power = 100 W.

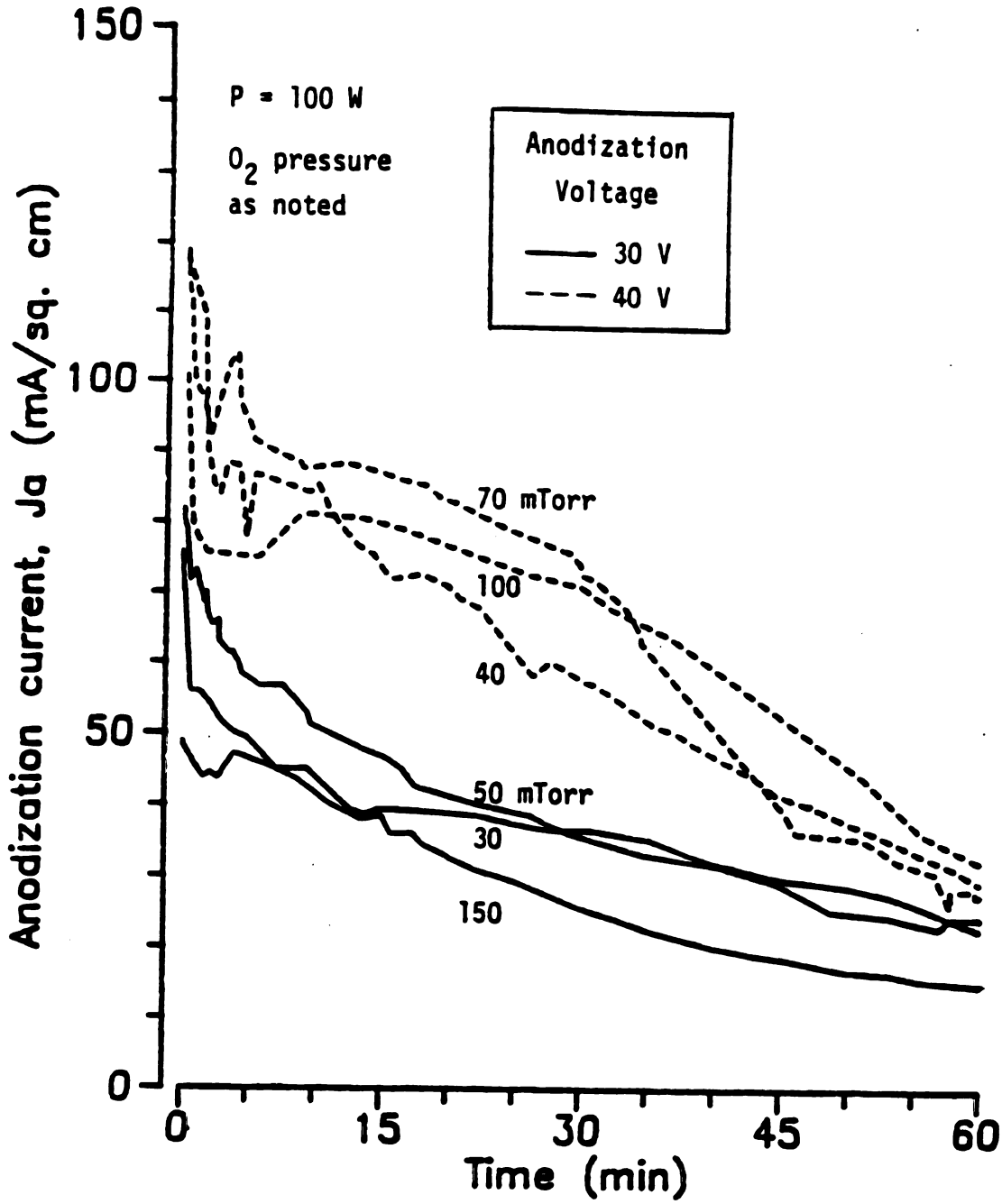

Figure 4.13. Anodization current for several of the samples represented in Figure 4.12.

dependence of anodization current upon plasma pressure. At 30 V, the oxide thickness was 600 Å at 30 mTorr, 1050 Å at 50 mTorr, and 500 Å at 150 mTorr. At 40 V, the peak was more pronounced, with X_{ox} increasing from 1300 Å at 40 mTorr to 1900 Å at 70 mTorr, and decreasing again to 1150 Å at 150 mTorr. This pressure dependence may be compared to Figure 4.14, which illustrates the pressure dependence of the saturation current in the gold-probe experiments (discussed in Section 4.2), and the pressure dependence of the values of initial anodization current density for these same samples. A similar pressure dependence is observed for each of these curves; however, this pressure dependence is different than that determined for the plasma density (Figure 4.4).

4.4 Oxide Surface Potential, Oxide Voltage, and Oxide Electric Field

The oxide electric field plays an important role in determining transport processes in the oxide during anodic oxidation. Over a wide range of typical experimental conditions, the effect of the electric field on the transport of oxidant species can be comparable to or greater than that of diffusion. For large fields, electric field dependent space-charge limitations on ionic transport can be important [48]. Furthermore, if the oxide field during growth is greater than the breakdown field in the oxide (typically on the order of 7 MV/cm), poor quality films will result. Also, electron conduction in the oxide is governed by the oxide electric field, and the flux of energetic electrons to the oxide-substrate interface may be important in determining interfacial reaction rates, as well as

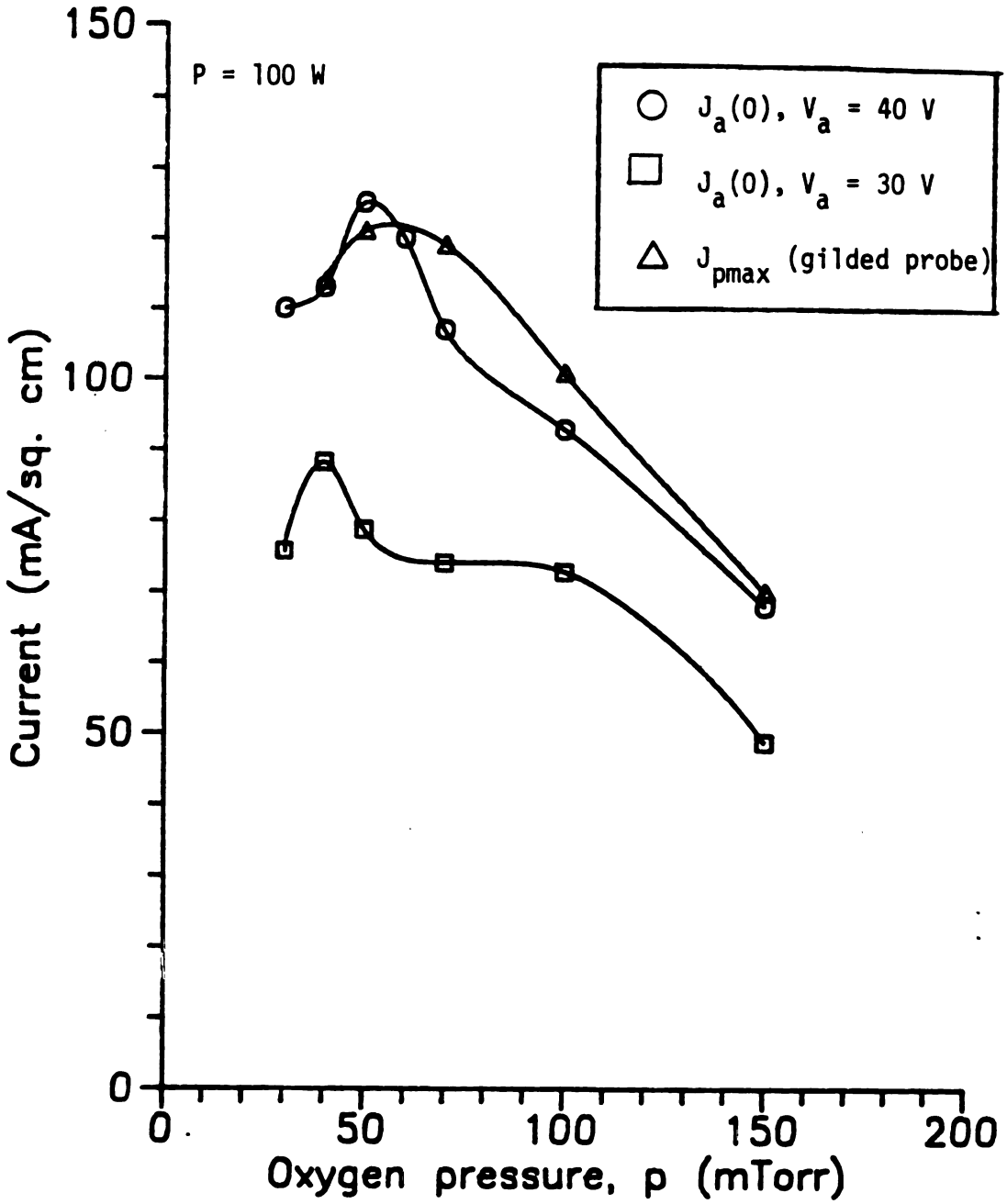

Figure 4.14. Pressure dependence of the maximum gilded probe current, J_{pmax}, the initial anodization current, $J_a(0)$, at V_a = 40V, and $J_a(0)$ at V_a = 30 V. Microwave power = 100 W.

the rates of production of certain types of defects in the bulk oxide and at the interface.

The electric field, oxide voltage V_{ox}, oxide surface potential V_s, and anodization voltage V_a are connected through the following relationships:

$$V_{ox} = V_a - V_s$$

and

$$E_{ox} = \frac{V_{ox}}{x_{ox}} \quad .$$

V_a is the potential at the substrate-oxide interface (the potential drop in the Si substrate is considered to be negligible), and V_s is the potential at the oxide-plasma interface.

The surface potential of a sample oxide film in an MPDR oxidation experiment was determined as a function of time by correlating the anodization current density recorded for the sample with the gold-probe J-V characteristics measured in the same plasma conditions (input power and oxygen pressure). The gold-probe experiments are described in Section 4.2. It was assumed for this purpose that the oxide surface potential which corresponded to a given current during anodic oxidation was equal to the gold-probe potential which yielded the same current during the probe measurement. A graphical example of the determination of V_s vs. t is shown in Figure 4.15.

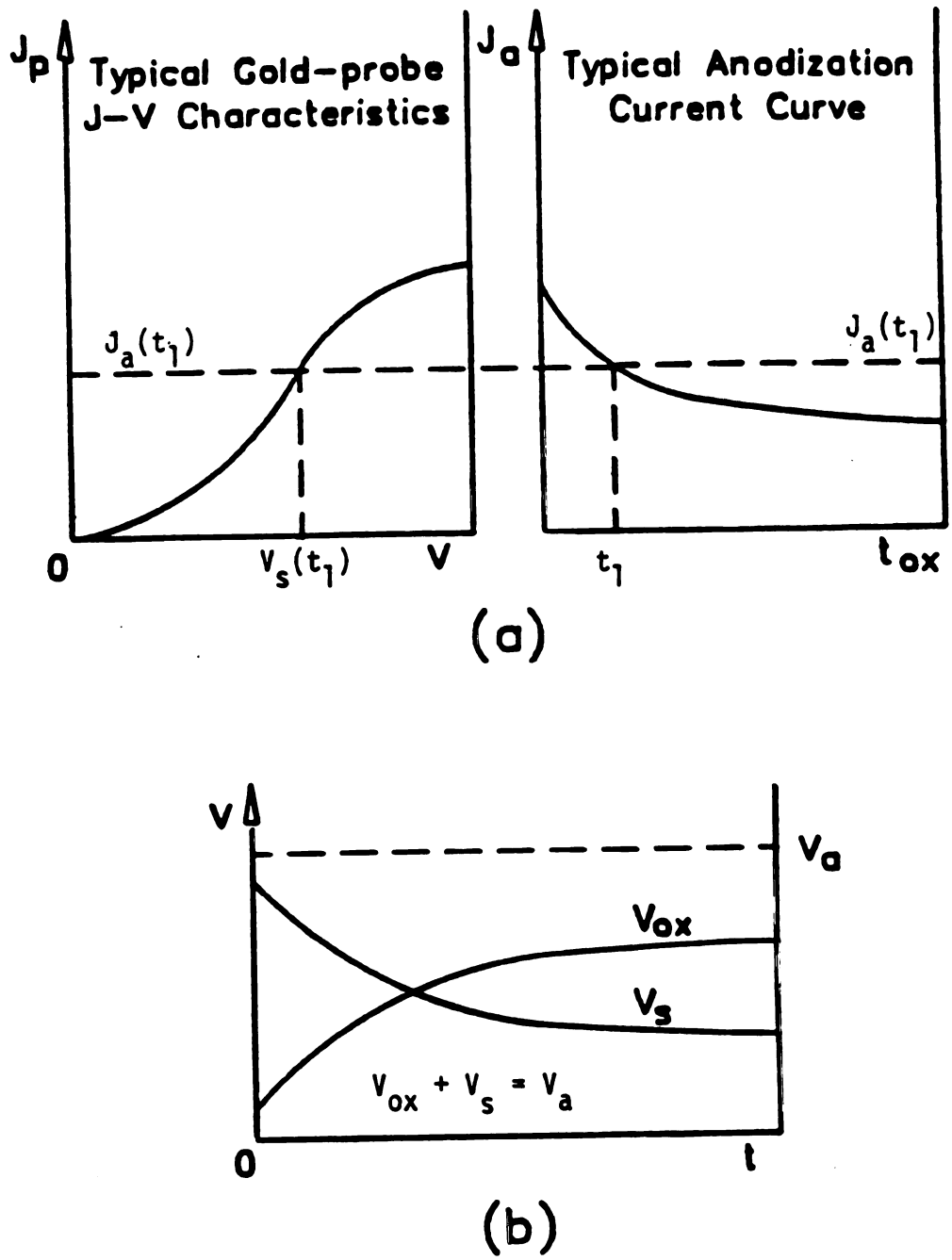

Figure 4.15. (a) Method of correlating gilded probe J-V characteristics with anodization current to obtain oxide surface voltage, $V_s(t)$. Probe characteristics and anodization current are measured at the same microwave power and oxygen pressure. (b) Illustrative $V_s(t)$ and $V_{ox}(t)$ curves resulting from the correlation procedure shown in (a).

The relationship of V_{ox} to anodization potential, plasma pressure, and microwave input power was investigated, and the results are presented in Figures 4.16 - 4.18.

Figure 4.16 shows V_{ox} as a function of time for samples prepared at several values of V_a in the range 18 V to 46 V. The microwave power and pressure were constant for the samples represented in this figure. The data are somewhat erratic near t = 0; this reflects both the rapid variations in initial stage anodization current which were often observed during anodization, as well as the nature of the gold-probe current-voltage characteristics in the high current (small t) regime. The slope of the gold-probe characteristics in the high current regime (near saturation) was small, so a small change in current corresponded to a large change in surface potential. Consequently, near t=0, small fluctuations in anodization current led to large fluctuations in V_{ox}.

In Figure 4.16 the oxide voltage is observed to increase with time during each anodization, and during the last 30 min or so the curves are clearly separated with V_{ox} an increasing function of V_a. Some of the curves show negative values near t = 0. Computationally, the negative values arise because the probe voltage was greater than V_a for the recorded value of J. Physically this might be interpreted as indicating the presence of a retarding field for negative ions and electrons in the oxide arising in response to a large initial diffusion current for these species. Another possible explanation is that there was an offset voltage associated with the gold probe immersed in the plasma, so that V_s was not exactly equal to V_p as assumed. Possible origins of such an offset include plasma sheath

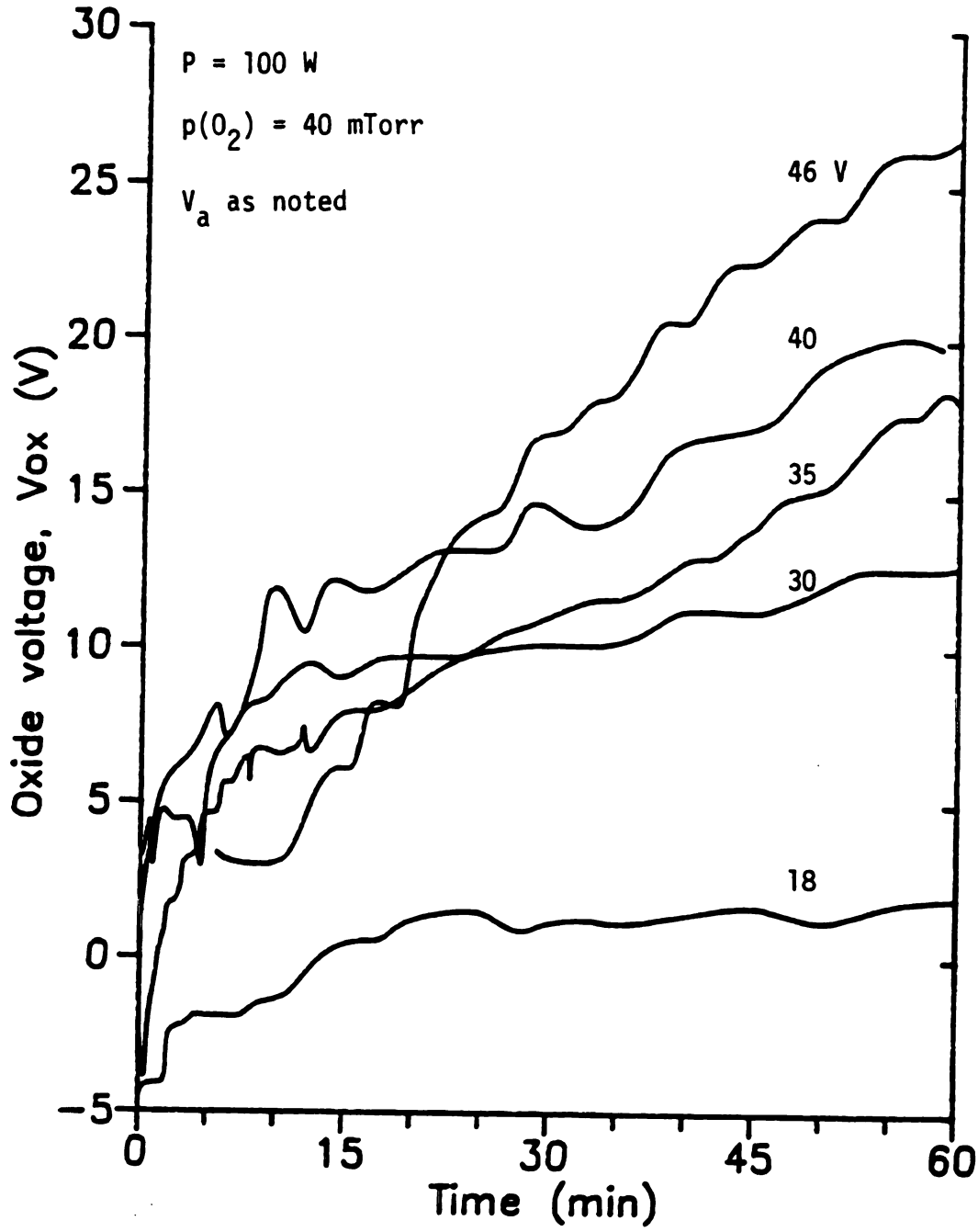

Figure 4.16. Oxide voltage as a function of time, with anodization voltage as a parameter. Microwave power = 100 W, O_2 pressure = 40 mTorr.

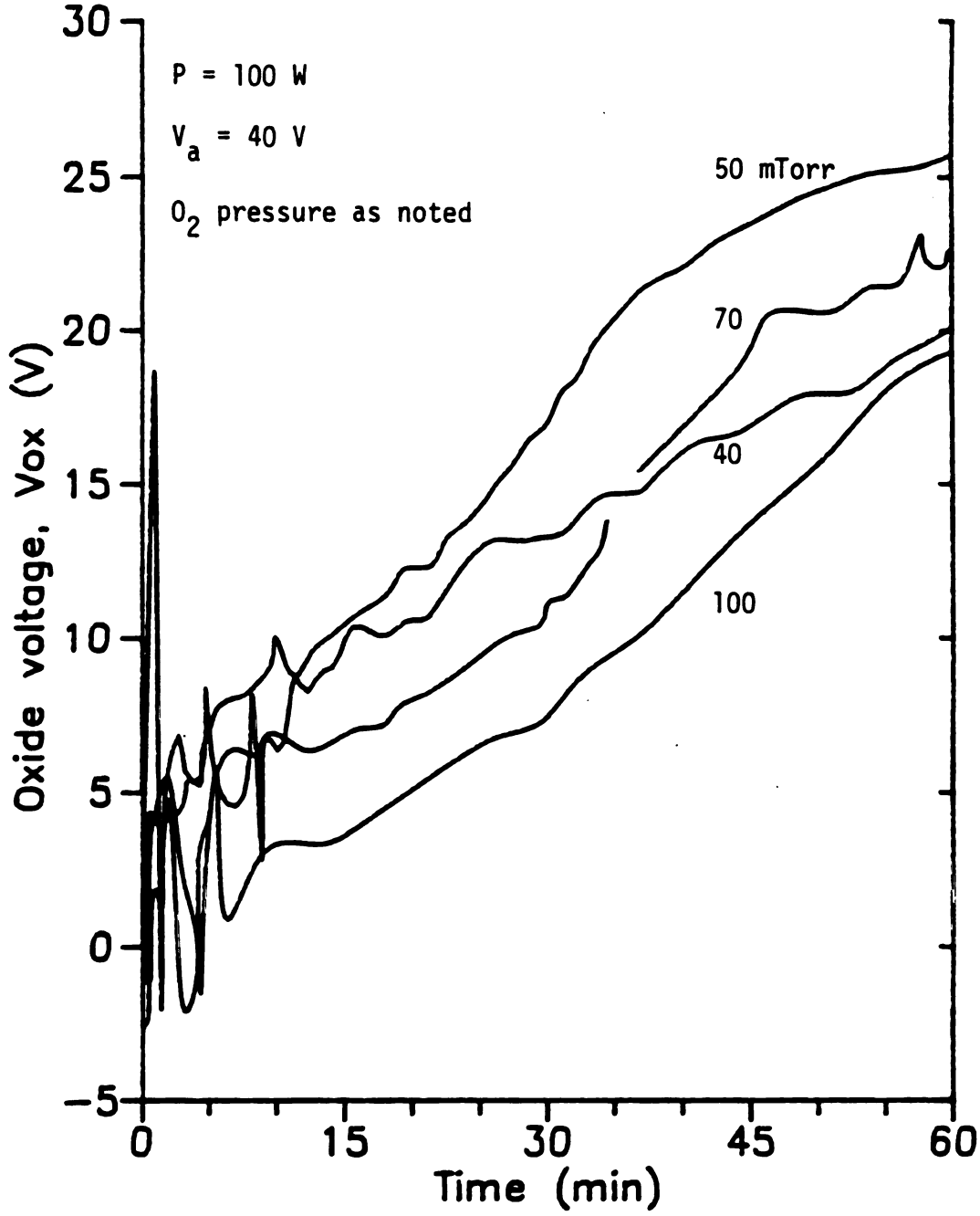

Figure 4.17. Oxide voltage as a function of time, with oxygen pressure as a parameter. Microwave power = 100 W, anodization voltage = 40 V.

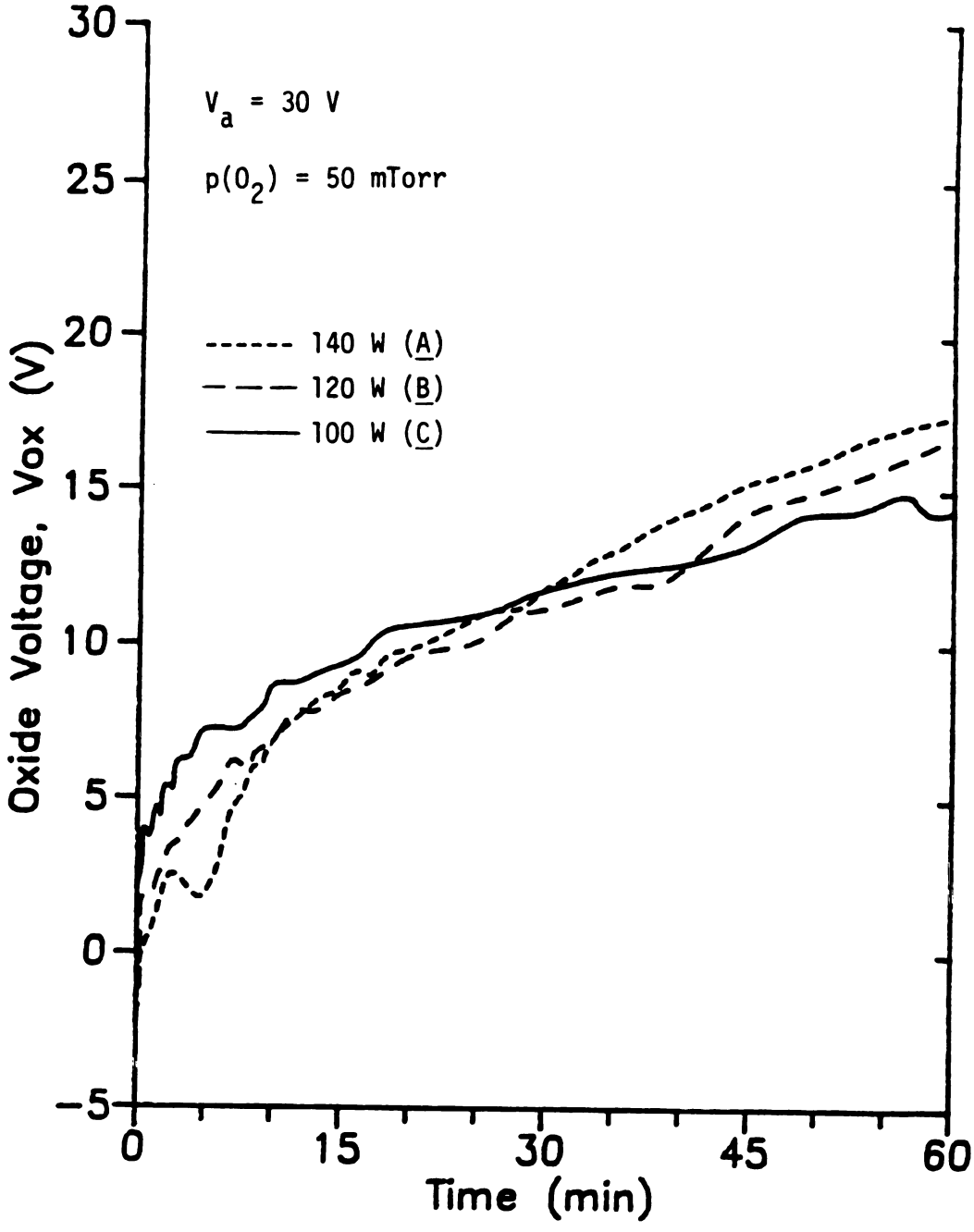

Figure 4.18. Oxide voltage as a function of time, with microwave power as a parameter. Anodization voltage = 30 V, O_2 pressure = 50 mTorr.

potentials, and plasma-metal or metal-semiconductor contact potentials, among others.

In Figure 4.17 the parameter is plasma pressure. After about 35 min, the order of the curves remains fixed, and the pressure dependence exhibits a peak at 50 mTorr. This is the same pressure dependence observed in Figure 4.14 for the initial anodization current, the final maximum gold probe current, and the final oxide thickness.

The effect of varying the microwave power is shown in Figure 4.18. The labels A, B, and C in this figure refer to the same samples as those in Table 4.4 and Figure 4.11. Initially the oxide voltage is a decreasing function of power, but after about 45 min the order of the curves is reversed. This is similar to the reversal of the order of the anodization current curves in Figure 4.11.

The average oxide electric field E_{ox} during oxidation was determined from the ratio of oxide voltage drop to oxide thickness, V_{ox}/x_{ox}. Because $x_{ox}(t)$ was not measured directly, E_{ox} was estimated in three different ways. These methods of estimation are described below, and illustrative growth curves resulting from each method are drawn in Figure 4.19.

Method 1. A constant growth rate was assumed for the entire anodization, with $x(t=0) = x_0$ and $x(t_f) = x_f$, where t_f was the total oxidation time and x_f was the measured oxide thickness for the sample. Thus the growth was described by

$$x_{ox}(t) = s_1 t + x_0 ,$$

$$\text{with } s_1 = (x_f - x_0)/t_f .$$

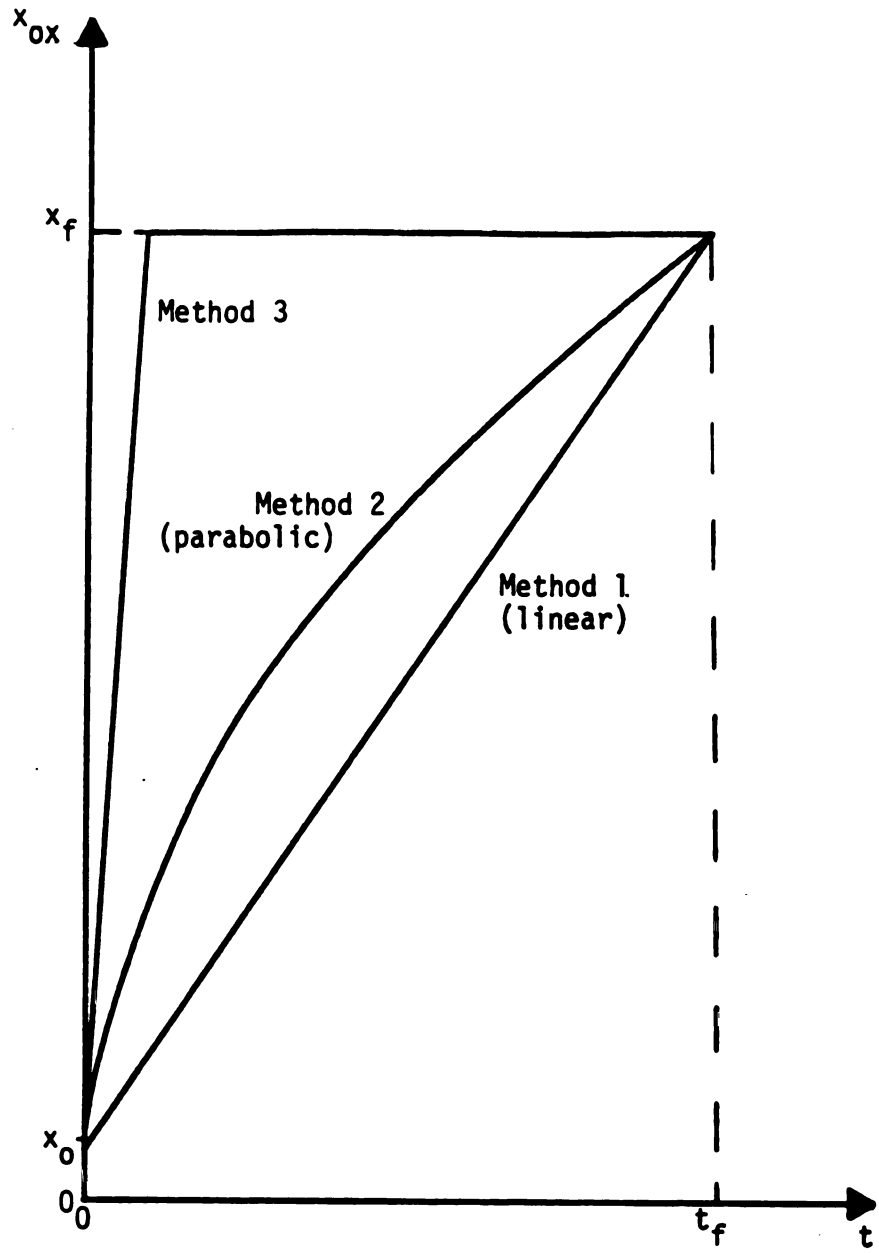

Figure 4.19. Growth curves illustrating three methods of estimating oxidation kinetics described in the text. Method 1: slow linear growth. Method 2: parabolic growth. Method 3: fast linear initial growth representing reaction-rate limited initial growth rate.

Method 2. A parabolic growth law was assumed, given by

$$x_{ox}^2(t) = kt + x_0^2 \quad ,$$

$$\text{with } k = (x_f^2 - x_0^2)/t_f .$$

Method 3. The growth rate was assumed to be linear and equal to the initial slope for Method 2, $k/2x_0$, for the time t_1 required to grow the total oxide thickness x_f, and then to be zero for $t_1 < t < t_f$. The growth equation was:

$$x_{ox}(t) = s_2 t + x_0 \quad \text{for} \quad 0 \le t \le t_1$$
$$x_{ox}(t) = x_f \quad \text{for} \quad t_1 \le t \le t_f$$

$$\text{with } s_2 = k/2x_0 \text{ and } t_1 = (x_f - x_0)/s_2 \ .$$

If it is assumed that the growth was approximately linear-parabolic in nature, then Method 1 provided an upper bound on E_{ox} during the entire oxidation process, and Method 3 provided an underestimate for E_{ox} for most of the growth period, but was potentially the most accurate during the inital, presumably linear growth stage. Method 2 would provide the most accurate estimate for E_{ox} during a diffusion-limited growth stage, where the expected growth would be parabolic.

Estimates of E_{ox} were calculated using the values of oxide voltage in Figures 4.16 - 4.18 and x_{ox} as given by Methods 1, 2, and 3 discussed above. The results are shown in Figures 4.20 - 4.22. The graphs in Figure 4.20(a) are scaled so that all of the data can be displayed. The irregular initial behavior exhibited by the curves is a result of dividing the already erratic V_{ox} data by small values of x_{ox}. In addition, the large negative initial values of E_{ox} shown for some of the samples derive from negative initial values of V_{ox}, which were discussed earlier as possibly being due, at least in part, to measurement inaccuracies. However, the sensitivity of the computations to these inaccuracies is greatly reduced as the oxide thickness increases and the anodization current decreases. It can be noted that since each of the oxide growth models converges to the measured value of final oxide thickness at t = 60 min, the estimates shown in the Figures tend to become more accurate as time increases. To allow the relationships among the curves to be more easily recognized, the graphs in Figure 4.20(a) are reproduced in Figure 4.20(b), ommitting the first 10 min of data and using a different scale. Similarly, in Figures 4.21 and 4.22, the first 10 min of each curve is ommitted for clarity.

Figure 4.20(b) shows the effect of anodization voltage on the oxide field. A significant observation is that with the exception of the 18 V curve, the oxide field was almost constant for most of the anodization, regardless of the model assumed for oxide growth. The average oxide field for sample #22 (V_a = 18 V) was notably lower than for the other samples for the entire duration of the anodization. The oxide thickness of 500 Å determined for this sample was the lowest among all the samples studied, and the anodization current

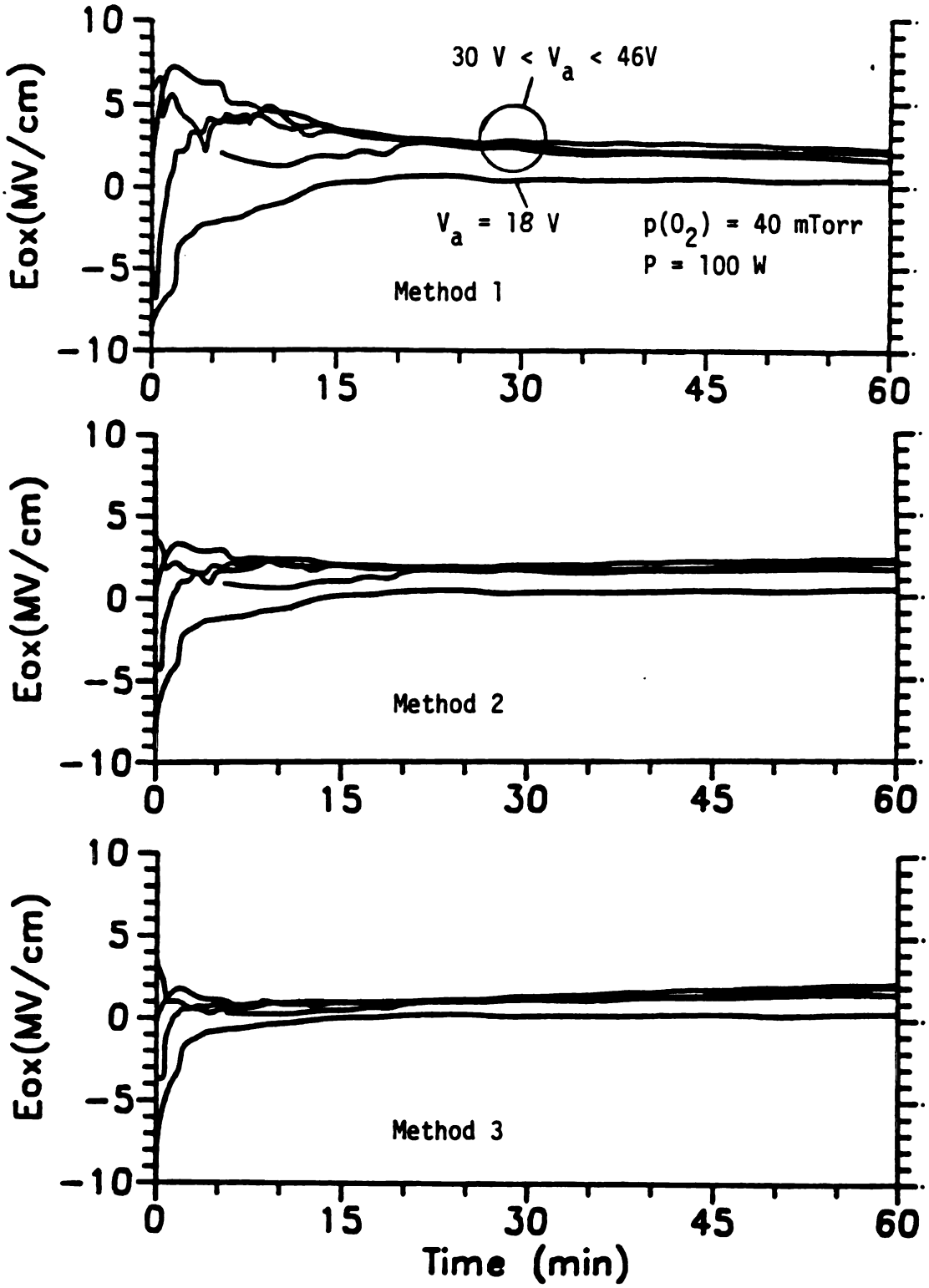

Figure 4.20. (a) Oxide electric field as a function of time estimated by three different methods (described in the text), with anodization voltage as a parameter. Microwave power = 100 W, O_2 pressure = 40 mTorr. Graphs are scaled to include the initial part of the curves.

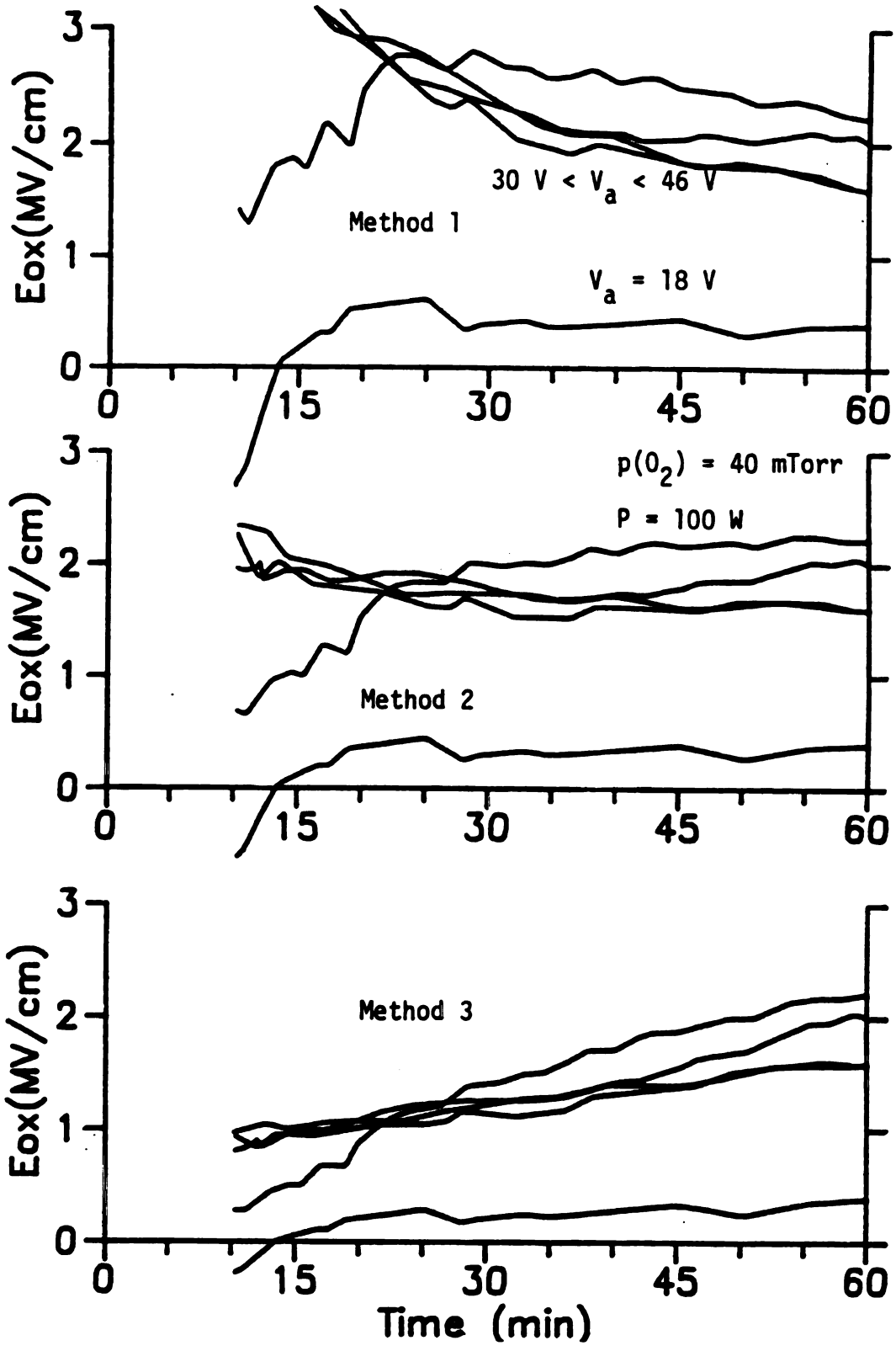

Figure 4.20. (b) This Figure is the same as Figure 4.20(a), except the first ten minutes of the curves are not shown, and the graphs are rescaled accordingly.

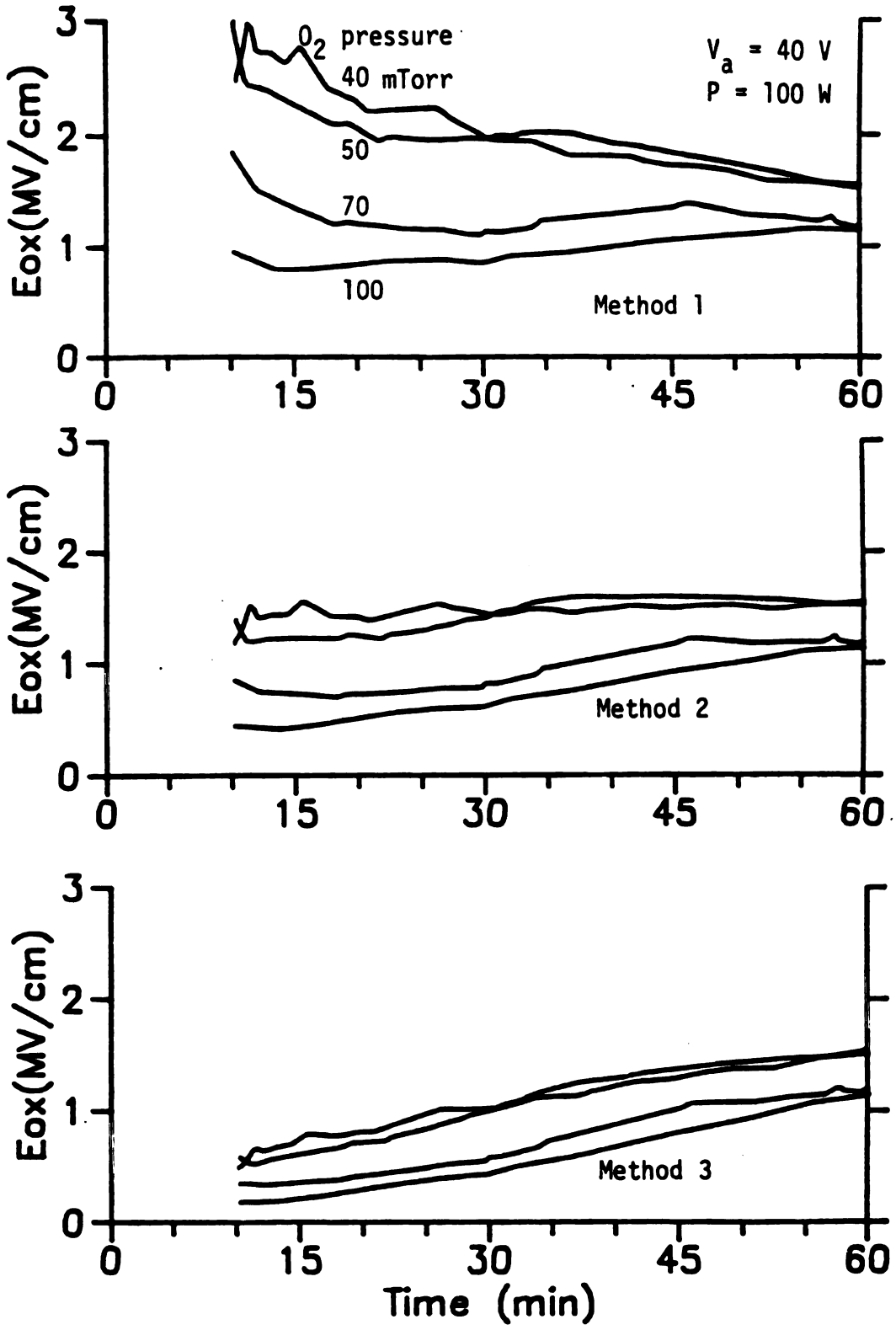

Figure 4.21. Estimated oxide field as a function of time with pressure as a parameter. Method of estimating oxide growth is indicated on each graph and described in the text. Microwave power = 100 W, anodization voltage = 40 V.

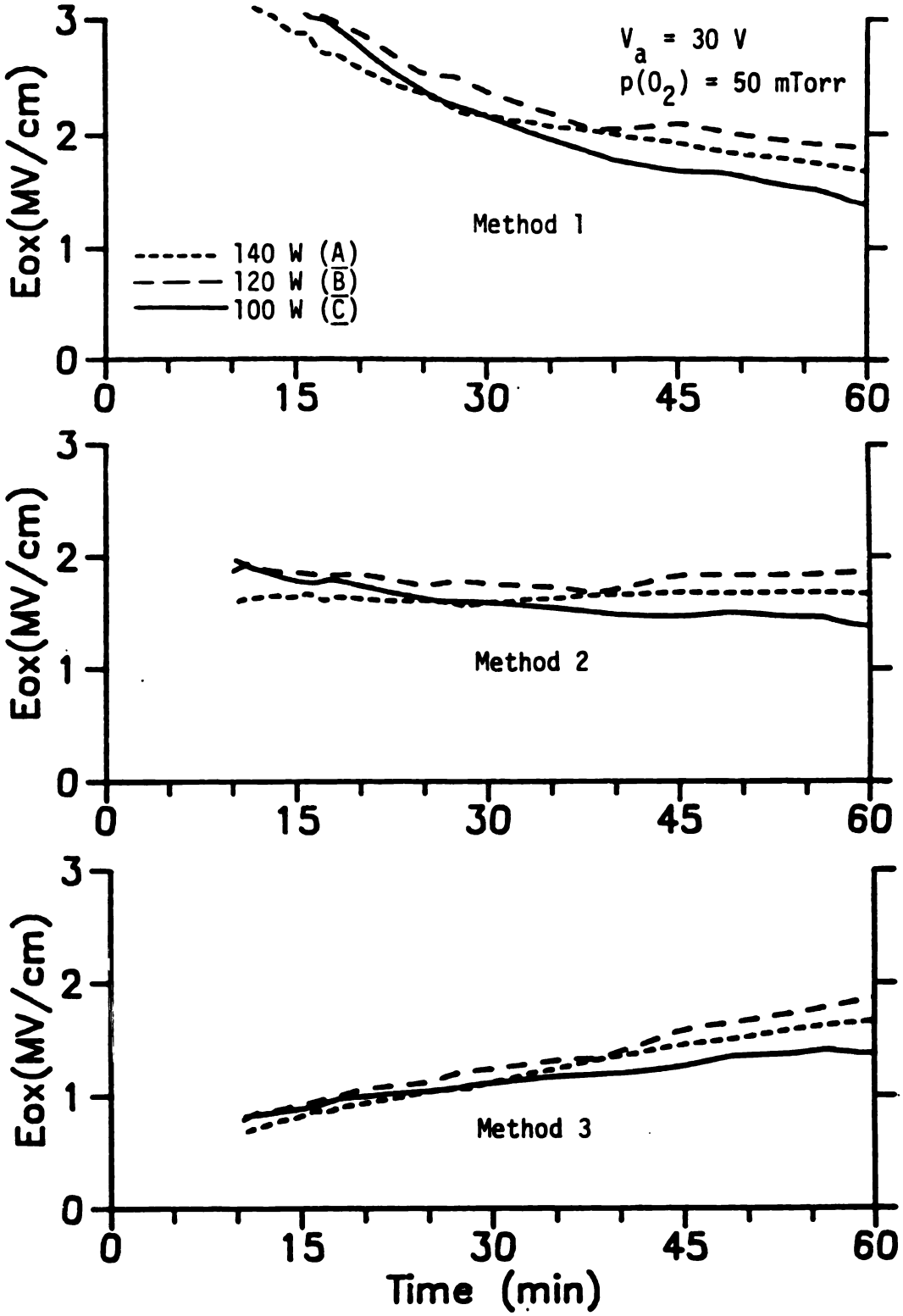

Figure 4.22. Estimated oxide field as a function of time with microwave power as a parameter. Method of estimating oxide growth is indicated on each graph and described in the text. Anodization voltage = 30 V, O_2 pressure = 50 mTorr.

(shown in Figure 4.10) was distinctly lower than for the other samples as well. At t = 60 min, E_{ox} was 0.4 MV/cm for sample #22, whereas for the other samples E_{ox} ranged from 1.6 MV/cm to 2.2 MV/cm. These values may be compared with the value of 1.5 MV/cm given in [7] as an empirically determined minimum field required for oxidation.

Figure 4.21 shows the effect of pressure on the estimated oxide field. Over most of the 60 min duration investigated there is a tendency for the oxide field to increase as the pressure decreases from 100 mTorr to 50 mTorr, however the most evident point regarding this plot is that regardless of the method of estimation, after the initial transient period E_{ox} falls into a well-defined range of values between 1 and 2 MV/cm. The final values of E_{ox} increase with decreasing pressure and range from 1.1 MV/cm to 1.6 MV/cm.

Figure 4.22 shows the effect of varying the microwave power. The labels A, B, and C refer to the same samples as in Table 4.4 and Figure 4.18. For the first few minutes of anodization, the oxide field was observed to increase with microwave power for the samples studied, however, this ordering was not maintained as the anodization progressed. The final values of E_{ox} are 1.4 MV/cm (C), 1.7 MV/cm (A), and 1.9 MV/cm (B).

4.5 Summary of the Oxidation Results

Analysis of the growth of SiO_2 films in the MPDR for 1 h constant voltage anodizations provided the following results:

(1) Oxidation occurred over the full range of each of the parameters investigated (the parameters studied and the range investigated for each parameter are listed in Table 3.1).

(2) Oxide thickness increased approximately linearly with anodization potential, and the slope of the linear relationship increased with oxygen pressure.

(3) The maximum oxide thickness occurred at a pressure of 70 mTorr. The variation of oxide thickness with pressure was similar to that observed for the saturation current of a large area gilded probe, but it was significantly different than the variation of plasma density determined from double Langmuir probe measurements. This is possibly an indication that the microwave discharge properties are significantly modified by supplying dc power to the discharge (i.e., by extracting a non-negligible dc current with the anodization or gilded-probe circuit).

(4) In the range investigated, varying the microwave power to the plasma did not have much effect on the oxide thickness, although it did affect the initial anodization current density, the plasma density, and the oxide electric field.

(5) The oxide surface potential decreased with time during anodization, correspondingly the oxide voltage drop increased in magnitude.

(6) The estimated electric field in the oxide was generally in the range of 1 to 2 MV/cm for most of the conditions studied.

Chapter Five

Analysis of the Plasma-Grown Oxide Samples

5.1 Introduction

This Chapter presents the results of experiments and observations conducted to determine the quality of the plasma oxide films grown in the MPDR. These included microscopic and visual observations of the oxide films (Section 5.2), as well as measurements on MOS test capacitors formed on the films (Section 5.3). The latter included C-V characterization as well as I-V measurements. Interface trap density was extracted from the measured C-V data, and the effects of two annealing techniques were investigated. Dielectric strength and oxide leakage were also investigated for the plasma-grown oxide samples.

A summary of the major results presented in this Chapter, together with a comparison of the quality of MPDR-grown oxides and present-day thermal oxides, is provided at the end of Section 5.3.

5.2 Visual and Microscopic Observation of the Plasma-Grown Oxide Films

5.2.1 Oxide Thickness and Uniformity

Following oxidation in the MPDR, a visual examination of each sample was conducted to determine of the color of the oxide film, and to permit assesment of the uniformity of the film based upon color variations.

If a thin transparent film on a reflecting substrate is viewed under white light at near-normal incidence, the film will appear to have a certain color due to the destructive interference of light of wavelength λ, where

$$\lambda = \frac{2\,d\,n}{(k + \frac{1}{2})} .$$

Here, λ is the wavelength absent from the reflected light due to destructive interference, d is the film thickness, n is the refractive index of the film, and k is an integer order number.

This principle is commonly applied to the measurement of the thickness of SiO_2 films on Si substrates. Because of the subjectivity involved in color determination, it is necessary to have reference to a standardized color chart in order for this method to be accurate and repeatable. In addition, it is necessary to have an independent method for determining the order number for the film

thickness being measured, since in general each color is repeated in each order.

The MPDR-grown oxide film thickness was customarily measured by comparing the color, observed under perpendicular illumination with fluorescent light, with a detailed color chart designed for these conditions [76]. The order number was determined by rotating the samples under white light from near-normal incidence to near-parallel incidence and comparing the observed color sequence with that on the chart. An additional indication of the order number was provided by observing the sequence of colors displayed as the oxide thickness decreased toward the edges of the samples.

Although the listings in the color chart referenced above were separated by 200 to 300 Å, the thickness resolution obtained was better than this for the MPDR samples, because the samples could be compared with each other to improve the resolution. For example, twelve samples were determined to have colors which fell between the adjacent listings of 1000 Å and 1200 Å on the chart, and among these, four distinct colors could readily be observed and ordered by the appearance of more or less of either of the two endpoint colors. Therefore, the resolution in this thickness range was about 70 Å (about 7 percent). Similar resolution was obtained for the other thickness ranges investigated. For several samples, oxide thickness as a function of position on the sample surface was mapped using optical interferometry (a description of this technique is provided in [1]). The results were in close agreement with visual observations. Interferometry offered better thickness resolution than visual observation, but it was not used routinely on the MPDR

samples because it is a destructive technique which requires that a sample be selectively etched and then metalized before examination.

A typical MPDR-grown oxide sample had a circular central region of uniform color comprising 95 percent or more of the oxidized area, surrounded by a narrow ring or series of narrow rings of various colors extending outward to the unoxidized region of the silicon substrate. Each ring was typically 0.05 to 0.1 mm across, and the sequence of colors observed generally indicated steadily decreasing oxide thickness from the edge of the central region outward. As a rule, oxide samples prepared at higher pressures had thinner and fewer outer rings, and oxides prepared with higher anodization voltages had a thicker outer ring structure. The total diameter of the oxidized region on the substrate was usually several millimeters less than the diameter of the opening in the quartz mask (12.7 mm) used during the oxidation (see Section 3.5 and the Appendix for details of the sample mounting and mask geometry).

5.2.2 Surface Degradation of the Oxide Films

Microscopic examination of the MPDR-grown oxide films was conducted for the purpose of identifying various features, including oxide surface blemishes, local nonuniformities (as indicated by color variations), and pinholes.

The oxide samples were examined by optical microscopy with magnifications ranging from 65× to 1500×, and resolution up to 1 μm. Some sample oxide films were grown on substrates mounted outside the discharge zone, downstream in the vacuum system. These samples

showed considerably more evidence of surface damage than did samples mounted in the discharge zone. In particular, on each of the downstream samples there were very identifiable marks on the oxide surface seemingly indicative of bombardment by large particulates (50 - 100 μm). The presence of such particulates indicates the existence of an undesirable source of contamination in the version of the MPDR used in these experiments, which must be identified and removed to permit further investigation of the downstream mode of operation.

On several of the samples prepared inside the discharge zone, filamentary nonuniformities, or streaks, were observed on the oxide. These were apparently due to thickness variations, and they were more often evident on thicker oxides (> 1200 Å) than on thinner ones. A typical streak was slightly thicker than the surrounding oxide (as indicated by the color), and it was on the order of 10 μm wide and several hundred micrometers long.

5.2.3 Observation of Pinholes

Pinholes through the oxide were observed on most of the plasma-oxidized samples formed in the MPDR. The density of pinholes varied from sample to sample, but typically there were 3 to 5 pinholes in a microscope field of view 200 μm in diameter. The diameter of the pinholes ranged from about 5 μm to 20 μm, with most on the smaller end of this range. Prominent characteristics common to the pinholes were that they appeared almost exactly round, and that there was a small dark spot at the center of almost every one observed. Although at least one early investigation of oxide physical features indicated

a higher density of pinholes on plasma-grown oxides than on thermal oxides [77], no explanation was given for this observation. There are believed to be several possible causes of pinhole formation on the MPDR oxides: (i) sputtering of the oxide during growth due to the applied bias voltage, (ii) deposition in the form of particulates of some material exposed to the discharge, masking the oxidation in isolated spots, and (iii) the presence of particulate contamination on the substrate surface prior to vacuum pumpdown in the MPDR. The last two causes are considered the most likely, since sputtering of an oxide film would (a) be expected to require a higher dc bias (e.g., 100 to 200 V) than used in the oxidation experiments and (b) be accompanied by substantial deposition on the walls of the discharge chamber (not observed).

As described in more detail in the Appendix, the substrate surface preparation consisted of scrubbing with methanol and rinsing with H_2O, but did not include other pre-oxidation cleaning steps which are used in conventional thermal oxidation. These additional steps include immersion in boiling TCE (a solvent), de-metal etch (an HCl and H_2O_2solution) and de-grease etch (an NH_4OH and H_2O_2solution). (The principal reason for not including these steps was that in order to be effective, they would have had to be implemented after the bias wire was attached, which was considered impractical.) In addition, after cleaning, the samples were exposed to unfiltered room air while being mounted in the MPDR, leading to the likelihood of some surface recontamination prior to system evacuation.

In view of considerations stated above, it is quite likely that the pinholes were a result of surface contamination of the

experimental substrates which occurred prior to initiation of oxidation.

5.3. MOS Capacitor Measurements

5.3.1 Overview

MOS capacitors were formed on some of the plasma grown oxide samples to permit the use of standard capacitance-voltage (C-V) and current-voltage (I-V) techniques for interface and bulk oxide characterization. Interface trap density and oxide uniformity for the MPDR-grown oxides were investigated by the high-frequency C-V technique introduced in Section 2.4. Oxide leakage resistance and breakdown strength was investigated by I-V measurements. These properties were compared with the reported properties of oxides formed in other plasma reactors, and with the properties of thermally grown oxides.

5.3.2 MOS Capacitor Device Preparation

MOS capacitors were formed on the MPDR-grown oxide samples by evaporating aluminum on an entire oxide sample, and then selectively removing the aluminum using contact photolithography and etching. This process left an array of aluminum dots on the sample surface. Each dot defined the top contact (gate) for an MOS capacitor. The back contact for each capacitor was provided by the stainless steel

chuck upon which the sample was mounted for probing. The sample was maintained in intimate contact with the chuck during testing by a vacuum system. For the devices reported here, the gates were circles 200 μm in diameter on 250 μm centers. Thus the capacitor area was 3.14×10^{-4} cm^2. If a typical value of 3.9 is used for the relative dielectric permittivity of the oxide, the following expression gives the oxide capacitance in pF when the oxide thickness is expressed in Angstroms:

$$C\ (pF) = \frac{1.09\times10^{4}}{x_{ox}(\text{Å})} \quad .$$

Values of x_{ox} for the samples studied ranged from 500 Å to 2500 Å, resulting in expected oxide capacitances in the range 4.3 pF to 22 pF.

5.3.3 High-Frequency C-V: Experimental Method

A block diagram of the measurement apparatus used in the high-frequency C-V analysis of the plasma oxide samples is shown in Figure 5.1. Substrates were vacuum-mounted on the stainless steel chuck of a wafer test station. Contact to the gate of a capacitor to be tested was made by manually positioning a tungsten probe on the gate with the aid of a micromanipulator and a low power optical microscope provided at the station. Capacitance was measured with a Boonton Model 74C-S8 Bridge, which operated at a fixed frequency of 100 kHz. This bridge provided four-digit precision for capacitance readings,

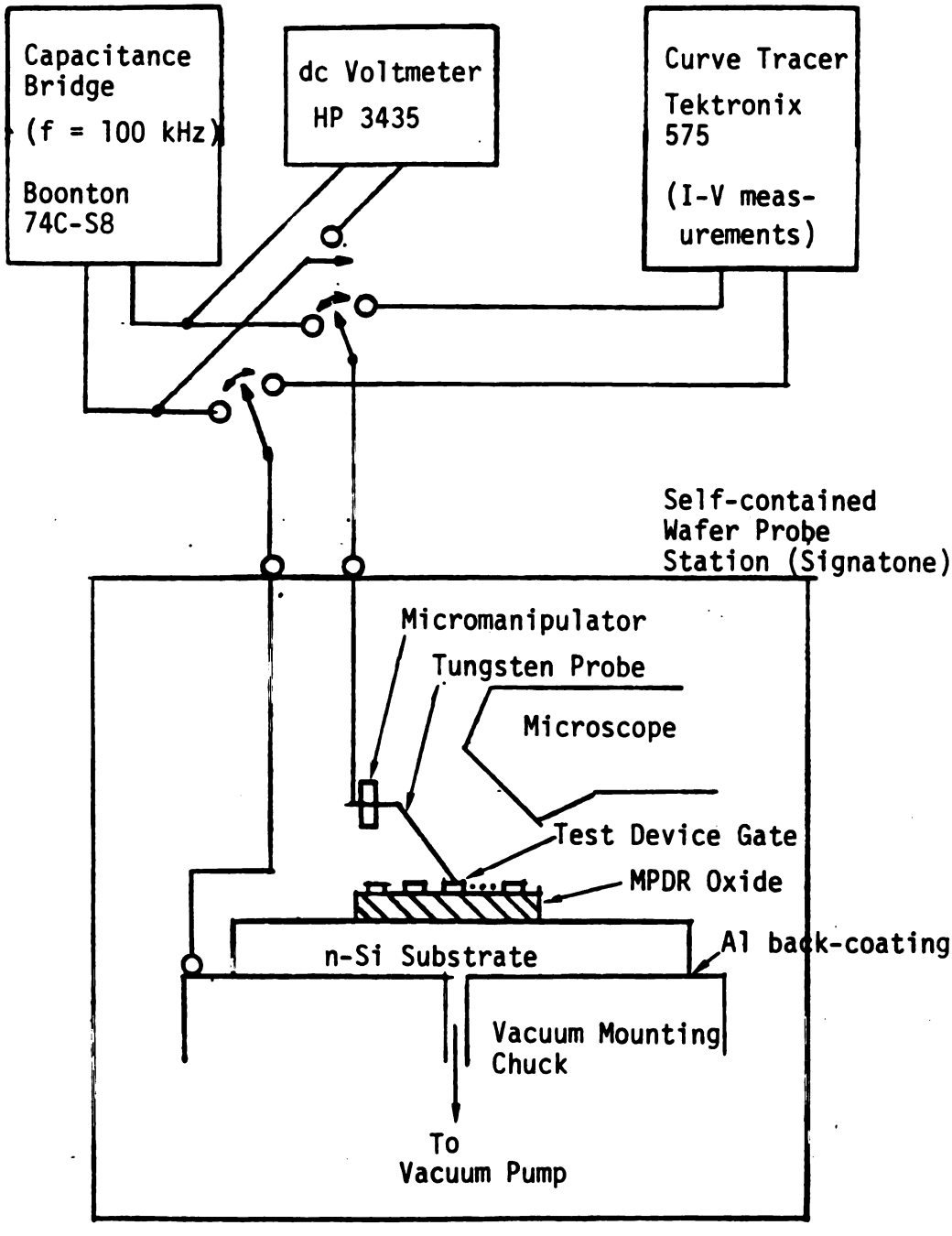

Figure 5.1 Experimental set-up used for making C-V and I-V measurements on the MPDR-grown oxide samples.

and two digit precision for ac conductance readings. A dc bias supply was built in to the bridge. Capacitance, conductance, and gate bias voltage (V_G) readings were recorded manually. Data points were recorded at least ten seconds apart, ensuring sufficient time for thermal equilibrium to apply during each measurement. In a typical device analysis, V_G was varied from +5 V to -20 V (potential at the gate with respect to the back contact) and about 25 data points were recorded, with most points allocated to the depletion region, where capacitance varied rapidly with voltage. (A discussion of MOS C-V characteristics is included in Section 2.4.)

5.3.4 Results of C-V Measurements on the Plasma-Grown Oxides

A considerable volume of data was accumulated in the C-V measurements, and rather than presenting all the data here, an attempt has been made to present enough to allow the reader to appreciate the principal results, without redundancy.

Three MPDR-oxidized samples, #36, #38, and #39, were selected for C-V characterization. These samples were selected primarily because they appeared highly uniform and unblemished, except for the presence of pinholes. They were all grown with V_a = 30 V and 100 W microwave power. Sample #36 was grown at 100 mTorr oxygen pressure, sample #38 at 150 mTorr, and sample #39 at 70 mTorr. Approximately one hundred capacitors were formed on each sample, with gate geometry as previously specified. Each device on a particular sample was uniquely identifiable within a cartesian coordinate system centered

around an origin (device 0,0) which was chosen by virtue of being easily recognized under the test-station microscope.

Because of the existence of pinholes in the oxide films, most of the devices tested encompassed surface regions where the gate metal was in direct contact with the silicon substrate, forming an Al-Si Schottky barrier diode structure (this structure is discussed in detail in [78]). The effect on the C-V measurements when a Schottky barrier diode is in parallel with an MOS test capacitor is considered next. The metal-semiconductor contact is accompanied by a depletion layer in the silicon of width x_{sb}, where

$$x_{sb} = \left[\frac{2\epsilon_s}{qN_D}\left[\psi_{s0} - V_G - \frac{kT}{q}\right]\right]^{\frac{1}{2}} \qquad [5.1]$$

having capacitance per unit area C_{sb}, where

$$C_{sb} = \frac{\epsilon_s}{x_{sb}} \; . \qquad [5.2]$$

These expressions may be compared with similar expressions applying to the MOS capacitor, for which the depletion layer width is given by

$$x_d = \left[\frac{2\epsilon_s}{qN_D}\,(-\psi_s)\right]^{\frac{1}{2}} \qquad [5.3]$$

and the capacitance per unit area in depletion is

$$C_d = \left[\frac{1}{C_{ox}} + \frac{1}{C_d}\right]^{-1} , \qquad [5.4]$$

where $C_d = \epsilon_s/x_d$, $C_{ox} = \epsilon_{ox}/x_{ox}$, and ψ_{s0} is the silicon band bending in equilibrium ($V_G = 0$) which is due to the metal-semiconductor work function difference and the presence of oxide charge, as discussed in Section 2.4. For the capacitor,

$$\psi_s = V_G - V_{ox} , \qquad [5.5]$$

where V_{ox} is the voltage drop across the oxide.

Equations 5.1 through 5.5 were used to compare the capacitance of an MOS capacitor ($x_{ox} = 1000$ Å) with that of a Schottky barrier diode, both devices having $N_D = 2\times10^{15}$ cm^{-3}. The MOS capcitor was assumed to have no oxide charge, and the threshold voltage was computed to be -1.29 V. At $V_G = -1$ V the value of C_d was 1.31×10^{-8} pF/cm^2 and C_{sb} was 1.17×10^{-8} pF/cm^2. Since these values were comparable, the relative contribution of the diode and the capacitor to the total measured device capacitance, would depend upon the relative areas of each. Using average values from the microscope observations reported in the previous section, i.e., four pinholes per device with diameter 10 μm, the total Schottky barrier diode area would be approximately one percent of the total gate area.

With this in mind, the C-V measurements made in depletion and inversion were safely considered to be largely unaffected by the oxide pinholes. However, the presence of pinholes prevented C-V measurements in strong accumulation, since the device conductance increased rapidly for $V_G > 0$, rendering the capacitance readings inaccurate. As a result, for most devices tested it was not possible to determine the true value of C_{ox}. In the data presented here, values of C are shown for $V_G > 0$ only for devices for which it was ascertained by I-V measurements that the device was not affected by pinholes.

Figure 5.2 shows the results of 100 kHz C-V and ac conductance (G-V) measurements on a device from each sample studied. The general features of a typical C-V curve are discussed in Section 2.4 and are illustrated in Figure 2.4. In the C-V curves shown in Figure 5.2, with increasingly negative gate bias, the regions of accumulation, depletion, and inversion are evident. An exception is that for the representative device from sample #39, the inversion region could not be investigated because the device exhibited breakdown-like instability before V_G reached the threshold voltage; however, it is likely that this was Schottky-barrier reverse breakdown related to the existence of oxide pinholes, as previously discussed.

From these C-V curves, values of oxide fixed charge, Q_f, were computed for the devices represented. It was assumed that oxide trapped charge, Q_{ot}, and mobile ionic charge, ρ_M, were negligible. Equation 2.8 was used to compute Q_f from the lateral translation, ΔV, of the C-V curves, measured as the difference between the experimentally determined flatband voltage, V_{FB}, and the ideal

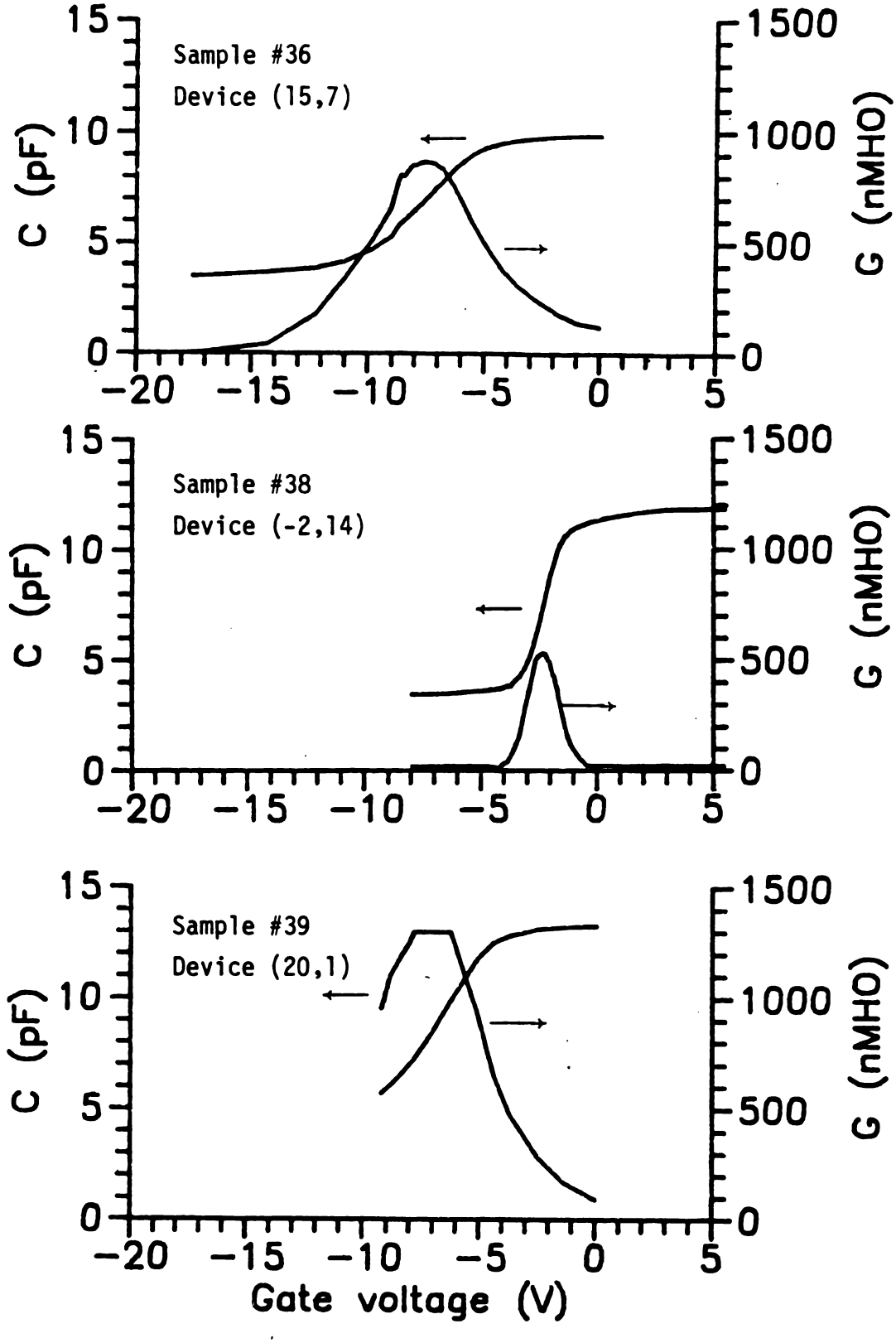

Figure 5.2 Results of C-V and G-V measurements on representative devices from three different MPDR-grown oxide samples.

flatband voltage, V'_{FB}. The values of Q_f thus determined are listed in Table 5.1.

Table 5.1 Oxide fixed charge densities calculated from the experimental C-V curves in Figure 5.2. For these samples, $N_D = 2\times10^{15}$ cm^{-3} and the ideal flatband voltage is $V'_{FB} = -0.246$ V.

Sample	x_{ox}(Å)	C_{FB}(pF)	V_{FB}(V)	$Q_f(cm^{-2})$
#36	1100†	7.71	-6.84	1.29×10^{12}
#38	917	8.87	-2.04	4.20×10^{11}
#39	815†	9.70	-6.28	1.60×10^{12}

†These values were computed from C measured at V_G=0 instead of in strong accumulation ($V_G \gtrsim 5$ V), therefore the true values of x_{ox} are several percent smaller than those given here.

The G-V data in Figure 5.2 can be compared qualitatively with, for example, Figure 5.13 in [2] to verify the expected MOS conductance behavior. However, in order to obtain quantitative information from G-V data, a series of measurements must be made at different frequencies, and this type of analysis was not carried out for the samples studied here. However, it is shown in [78] that the peak of the G-V curve increases with interface trap density at any frequency. Comparing sample #38 with either sample #39 or sample #36, it is evident that the C-V curve for sample #38 shows the least amount of stretchout in depletion, indicating, as discussed in

Section 2.4, that this sample has the lowest interface trap density, and this is corroborated by comparison of the G-V curves.

Hysteresis in a C-V curve can be indicative of the presence of mobile ionic contamination. As the gate bias is made increasingly negative, for example, positive ions such as Na^+ drift in the oxide toward the gate, shifting the C-V curve by an amount which can be calculated using Equation 2.8. If the gate bias is then swept back to its starting value at a different rate than that by which it was increased, hysteresis results. Figure 5.3 shows the results of a hysteresis measurement on a device from sample #38. On this figure, the data points represented by crosses were taken as V_G was made more negative, and the circles indicate the retrace data points. This device was typical of all the devices studied from each sample in that there was no evidence of hysteresis.

The effects of annealing were investigated on the plasma-grown oxide samples, since it is well known that the values of Q_f and D_{it} for thermal oxides are substantially reduced by annealing. In addition, most reports in the literature indicated that significant improvement in the properties of plasma-grown oxides was obtained by annealing (i.e., see Section 2.4).

A commonly used post-metalization annealing treatment is a low temperature ($< 600\ ^oC$) anneal in forming gas (5% H_2, 95% N_2). Sample #38 was annealed in forming gas at 450 ^oC for 1 h. Figure 5.4 shows C-V curves measured for a typical as-grown device on this sample, and for the same device after the forming gas anneal. Also shown is the ideal C-V curve computed using x_{ox} and N_D for this sample. The forming gas anneal was evidently effective in reducing Q_f. The post-anneal flatband voltage shift was determined to be

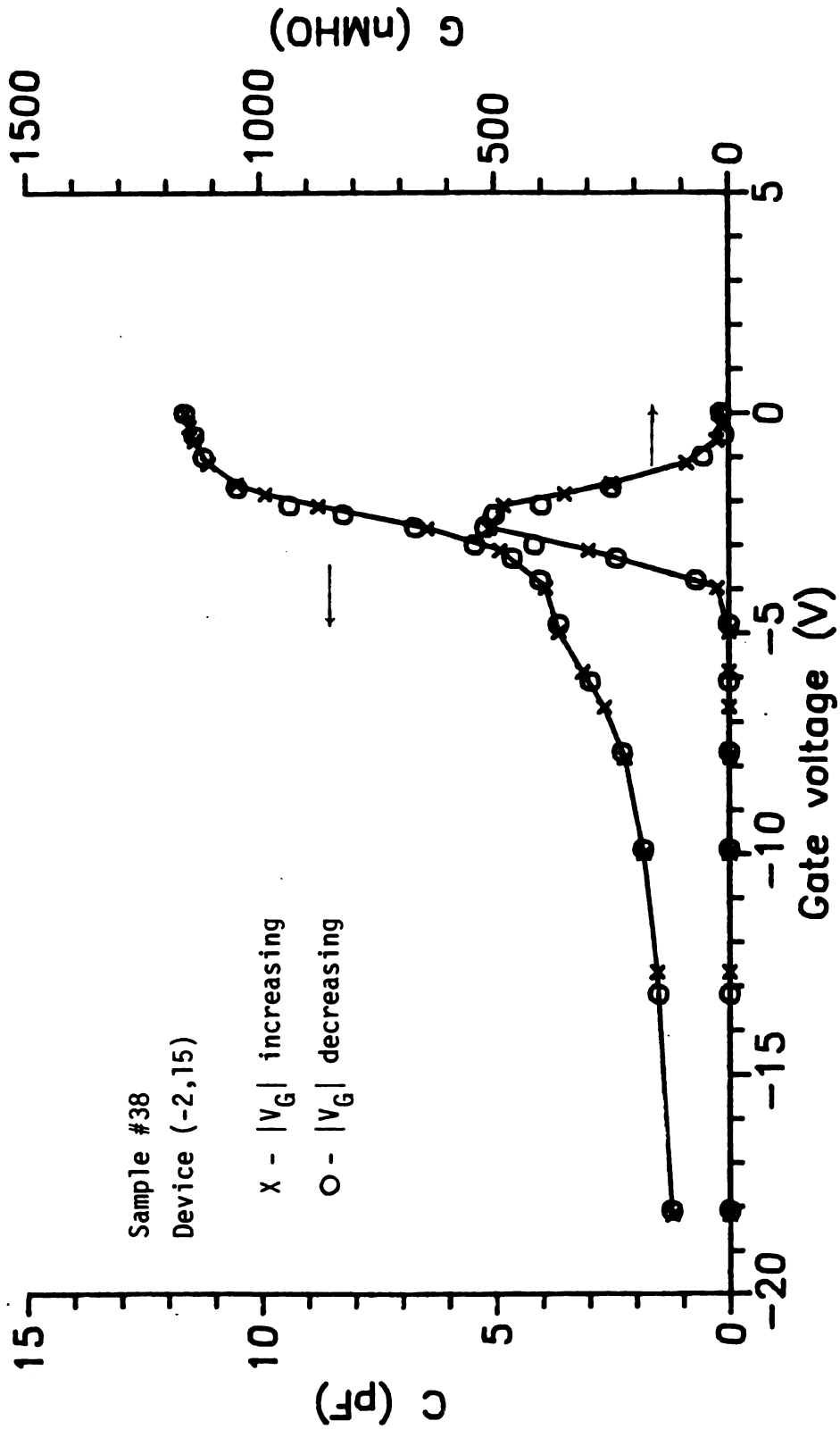

Figure 5.3 C-V and G-V measurements made on a representative device to investigate hysteresis resulting from mobile ion contamination; no hysteresis was evident on any of the samples studied.

-0.42 V for this sample, yielding $Q_f = 1.0 \times 10^{11}$ cm^{-2}. This may be compared with the as-grown value of Q_f, listed in Table 5.1 as 4.2×10^{11} cm^{-2}. The hydrogen anneal also reduced D_{it}, as discussed in Section 5.3.5.

The devices on sample #38 were the only ones to receive a hydrogen anneal. However, sample #36 received a nitrogen-only anneal at 450 ^{o}C. The post-anneal C-V characteristics of all the devices investigated on sample #36 suggested that the oxide dielectric strength was degraded. The C-V characteristics were no longer representative of an MOS sample; neither a flatband voltage nor a threshold voltage could be identified. Instead, a plot of $1/C^2$ vs voltage yielded a straight line which indicative of Schottky diode behavior. One possible explanation is that the N_2 anneal, or related sample handling, reduced the oxide dielectric strength so that at relatively low oxide fields the oxide underwent breakdown, effectively forming a metal-semiconductor contact under the gate.

5.3.5 Calculation of D_{it} from the C-V Data

The method by which interface trap density was extracted from measured C-V data is described here in detail. This method, which closely follows the technique described in [2], is applied by way of example to a particular device on sample #38, referred to here, for convenience, as device A. The pre-anneal, post-forming gas anneal, and ideal C-V characteristics for device A are those shown in Figure 5.4.

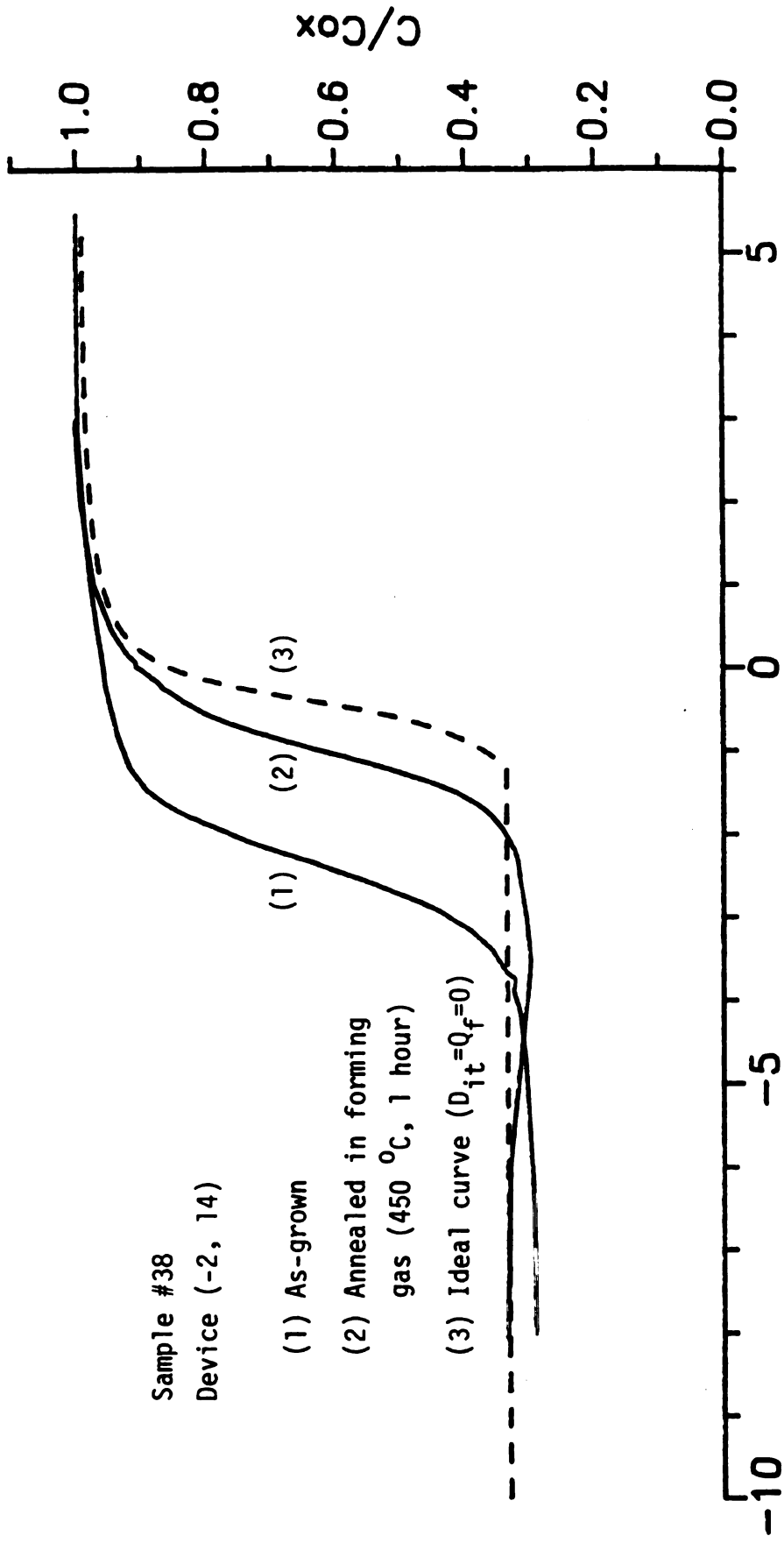

Figure 5.4 C-V curves for a representative device, showing the reduction of oxide fixed charge, Q_f, after annealing in forming gas. (Q_f causes a lateral translation of the C-V curve, as discussed in the text.)

To begin with, a theoretical C-V curve is calculated for a capacitor having the same values of x_{ox} and N_D as the real device. First, the silicon surface charge is computed:

$$Q_s = \left[\frac{\epsilon_s}{\lambda_i}\right]\left[\frac{kT}{q}\right] \mathrm{Sgn}(U_B - U_s)\ F(U_s,U_B), \qquad [5.6]$$

where λ_i is the intrinsic Debye length in the Si,

$$\lambda_i = \frac{\epsilon_s kT}{q^2 N_D} ,$$

and $U_B = (q/kT)\phi_B$, $U_s = (q/kT)\phi_s$, where ϕ_B and ϕ_s are defined in Figure 2.2. Sgn is the signum function. The quantity $F(U_s,U_B)$ is a dimensionless electric field given by

$$F(U_s,U_B) = \left[\frac{N_D}{n_i}\right]^{\frac{1}{2}}\left[(U_B - U_s - 1) + \frac{n_s}{N_D} + \frac{p_s}{N_D}\right]^{\frac{1}{2}} , \qquad [5.7]$$

where n_i is the intrinsic carrier concentration in the Si, and n_s and p_s are the electron and hole concentrations at the silicon surface. For n-type Si these can be computed from $n_s = n_i \exp(U_s)$, $p_s = n_i^2/n_s$.

Next, the silicon surface capacitance is computed:

$$C_s = -\mathrm{Sgn}(U_B - U_s)\left[\frac{\epsilon_s}{\lambda_i}\right] \frac{\sinh U_s - \sinh U_B}{F(U_s,U_B)} . \qquad [5.8]$$

The total device capacitance is computed as C_s in series with C_{ox}:

$$C = \left[\frac{1}{C_s(\psi_s)} + \frac{1}{C_{ox}}\right]^{-1} ,$$

[5.9]

where ψ_s is the silicon surface band-bending, $\psi_s = (kT/q)(U_s - U_B)$. The ideal gate voltage is computed to be the sum of the oxide voltage and the silicon band bending:

$$V_G = \frac{-Q_s}{C_{ox}} - \psi_s .$$

[5.10]

The appropriate choice for the independent variable in the expressions above is the silicon band bending, ψ_s. For n-type Si in accumulation, ψ_s is positive, and in depletion and inversion ψ_s is negative. In order to generate a theoretical C-V curve using Equations 5.7 - 5.10, a computer program was written which stepped ψ_s between user-specified limits. The limits were chosen initially by trial and error, the criterion being that the domain of band-bending values should be wide enough to generate the entire range of gate voltage values of interest.

A key point in the extraction of interface trap density is that interface traps do not affect the variation of C_s with ψ_s. Therefore, the measured value of C will be the same as the ideal value of C for the same band bending. However, the presence of interface traps decreases the fraction of the gate voltage which appears across the silicon space charge layer. For a given gate

voltage, the band bending for the real sample must be deduced by comparing the measured C-V_G curve with the theoretical C-ψ_s curve. If this is done at each value of measured gate voltage, the resulting ψ_s vs V_G curve can be used to calculate C_{it}, the interface trap capacitance, according to the following expression :

$$C_{it} = C_{ox} \left[\left(\frac{d\psi_s}{dV_G}\right)^{-1} - 1 \right] - C_s(\psi_s) \quad . \tag{5.11}$$

In order to carry out the above comparison efficiently, a computer program was written which read each measured C-V data point from a file, and then iteratively selected the value of ψ_s which resulted in a theoretical C equal to the measured value, and then recorded C, ψ_s, C_s, and V_G in a new data file. This new data file could be used to calculate C_{it}.

The final step was to calculate D_{it} from C_{it}. A derivation of the relationship between these quantities is given in [2]. For band bendings that do not place the Fermi level within a few kT/q of the band edges,

$$C_{it}(\psi_s) \approx qD_{it}(E_s) \quad , \text{ where}$$

$$E_s = E_i - E_V + \psi_s + (kT/q)U_B \quad . \tag{5.12}$$

The quantity E_s measures the position of the Fermi energy relative to the valence band edge at the silicon surface. For this n-type

sample, as the gate bias is made more negative than required for flat-bands, the band bending becomes more negative, the bands bend increasingly upward at the silicon surface, and the relative position of the Fermi energy is closer to the valence band edge, so E_s decreases. As discussed in [2], only the interface traps within a few kT of the Fermi level affect the measured capacitance, so the effect of varying the band-bending is to select out and measure those interface traps near the Fermi level. The Fermi level "points" to the interface traps being measured at a given gate bias. The energy relative to the silicon valence band edge associated with this "pointer" is given by E_s.

Plots of D_{it} vs E_s for device A as-grown and after annealing in forming gas are shown in Figure 5.5. Several points are noteworthy regarding this plot. In strong inversion, the band bending is pinned at $-2\phi_B$, so the Fermi level is pinned at $E_i - q\phi_B$. Therefore, the range of energies from the valence band edge to slightly below mid-gap cannot be explored on an n-type device using the high-frequency C-V technique. Also, as the device is driven into accumulation, the capacitance and the band bending change very slowly with gate bias. This leads to large inaccuracies in extracting D_{it}, since Equation 5.11 involves a derivative which must be calculated from a limited number of data points, as well as a subtraction of two quantities which are large and of comparable magnitude.

The D_{it} curves in each case are roughly U-shaped, with the minimum value obtaining when the Fermi level is near mid-gap. This is characteristic of D_{it} plots reported in other work for both thermally-grown oxides and plasma-grown oxides.

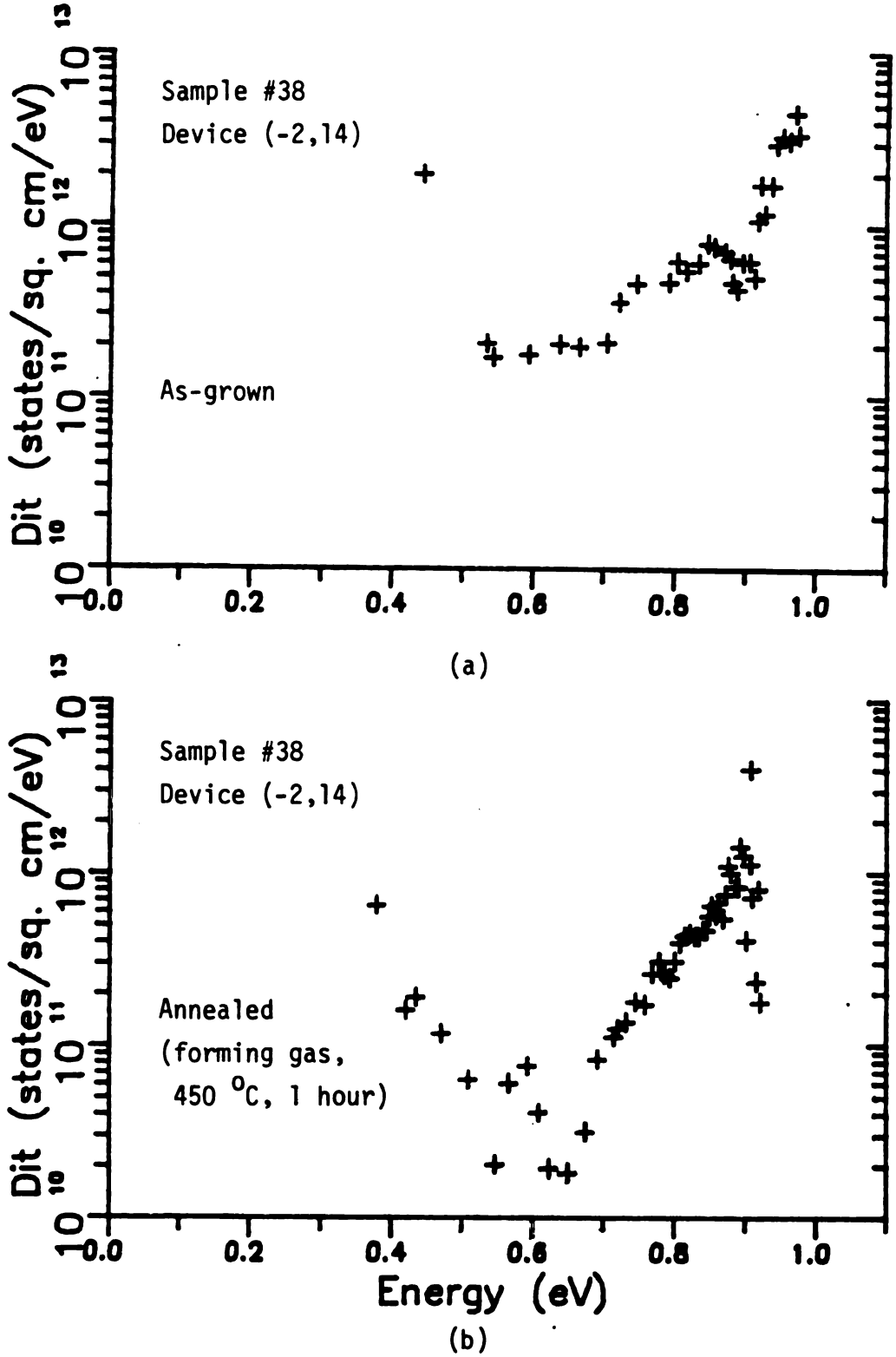

Figure 5.5 D_{it} as a function of energy in the silicon bandgap (0.0 eV = valence band edge, 1.1 eV = conduction band edge). (a) As-grown. (b) After annealing in forming gas . Data points for these plots were computed from the measured C-V data shown in Figure 5.4.

The minimum value of D_{it} for the as-grown device A was 1.7×10^{11} $cm^{-2}eV^{-1}$; this value occurred at E_s = 0.54 eV, just below midgap ($E_s \simeq 0.55$ at midgap). After annealing in forming gas, the minimum value of D_{it} was reduced to 1.8×10^{10} $cm^{-2}eV^{-1}$, and the minimum occurred at 0.65 eV. This reduction in D_{it}, together with the observed reduction in Q_f, indicates that the forming gas anneal was effective in improving the interface properties of the sample oxide.

5.3.6 I-V Measurements on the MOS Capacitors

Pre- and post-anneal breakdown field histograms were obtained for devices on sample #38, and the results are shown in Figure 5.6. The measured pre-anneal breakdown fields for 18 devices ranged from 1.03 MV/cm to 5.58 MV/cm, and averaged 2.58 MV/cm. The post-anneal breakdown fields measured for 37 devices ranged from 1.18 MV/cm to 10.3 MV/cm, and averaged 6.26 MV/cm. In addition, the post-anneal histogram is peaked in the range 6 - 8 MV/cm. The post-anneal results obtained here are similar to those obtained on good quality thermally grown oxides, indicating further the beneficial effect of the forming gas anneal.

The dc currents through the oxides were measured as a function of gate bias and results are shown in Figure 5.7. This data must be interpreted in light of the oxide pinholes discussed earlier. In pinhole regions, the gate metal is in intimate contact with the underlying silicon. The resulting Schottky diode structure is in reverse bias under capacitor test conditions (except in strong

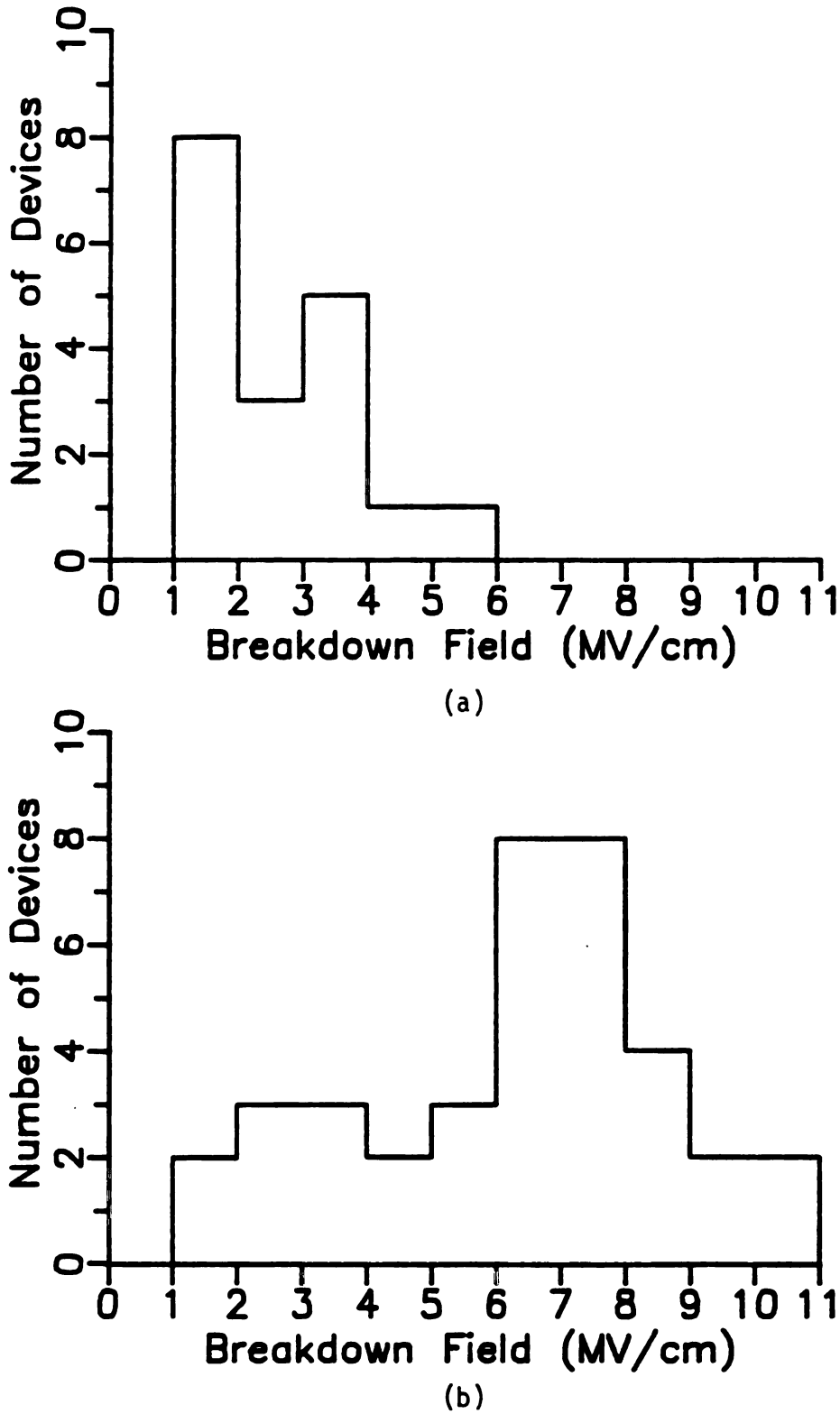

Figure 5.6 Histograms of oxide electric field required to cause breakdown. (a) As-grown MPDR oxides. (b) After annealing in forming gas at 450 ^{o}C for 1 h.

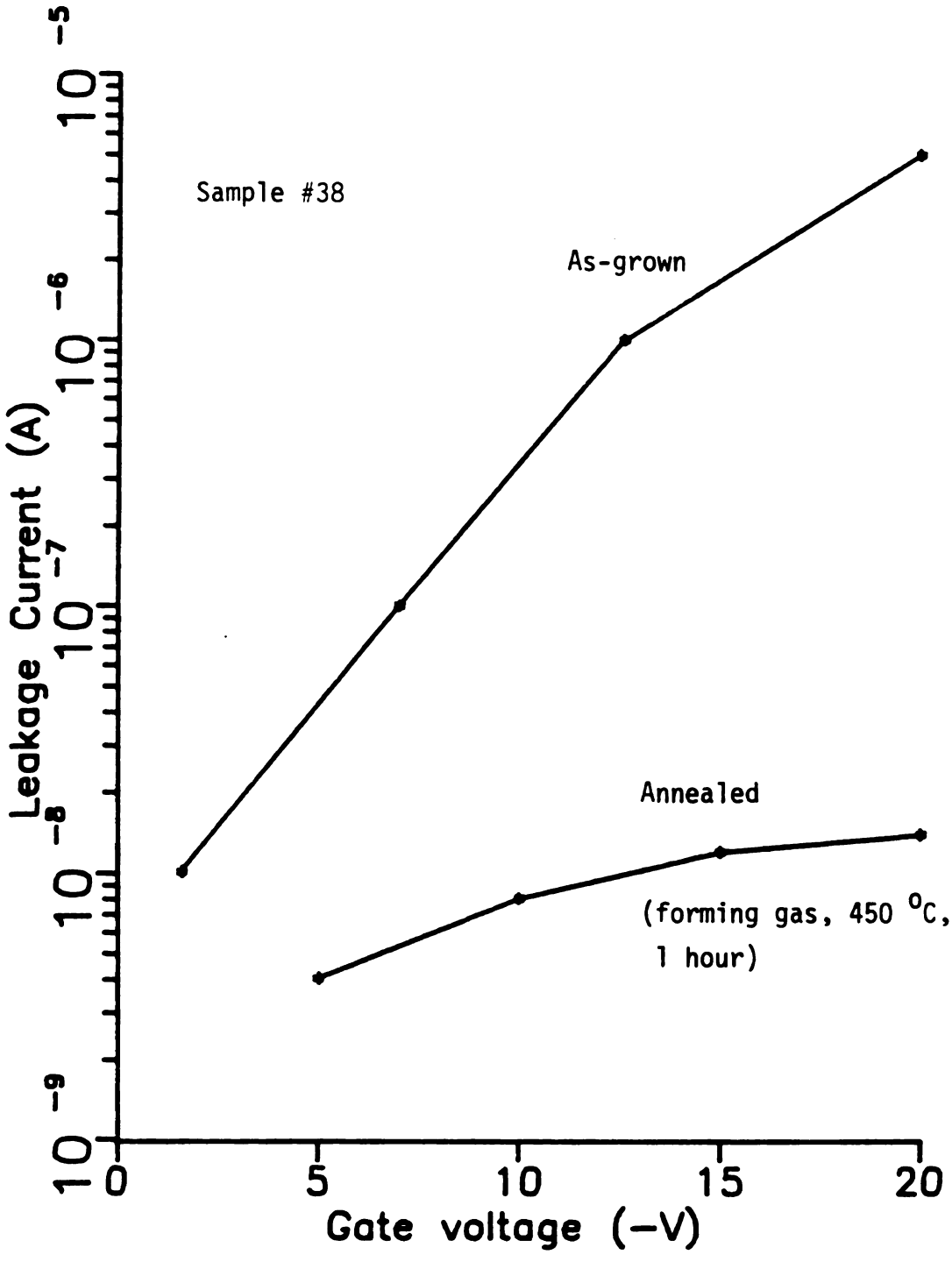

Figure 5.7. Leakage current measured on a representative device before and after annealing in forming gas. This current is probably due to pinholes in the oxide.

accumulation). The reverse current in a Schottky diode is dependent upon the metal-semiconductor Schottky barrier height, and does not actually saturate (as does the reverse current in a p-n junction diode) because of the electric field dependence of the barrier height [78].

Assuming, as discussed in Section 5.3.4, that the pinholes under a typical capacitor gate comprise about one percent of the total gate area, a diode leakage current density of about 10^{-3} A/cm^2 would account for the observed leakage currents. In fact, the reverse characteristics of Schottky barrier diodes with barrier heights of 0.7 eV (which is approximately the barrier height of Al on Si) increases from about 10^{-4} to 10^{-3} A/cm^2 as the bias increases from -1 to -10 V [79]. Therefore, it is surmised that the values of leakage current indicated in Figure 5.7 are due to oxide pinholes, rather than the conductivity of the oxide. Further evidence for this was provided by I-V measurements in the forward-bias regime, which yielded typical forward bias diode-like characteristics.

5.3.7 Summary of MOS Capacitor Measurement Results

As-grown MOS capacitors on the plasma oxides exhibited fixed charge densities in the range from 4×10^{11} to 1×10^{12} cm^{-2}. Mid-gap interface densities of about 2×10^{11} cm^{-2}ev^{-1} were measured. A breakdown field histogram peaked between 1 and 2 MV/cm. After annealing in 5% H_2, 95% N_2 at 450 ^{o}C for 1 h, a substantial improvement was observed in each property tested. The value of Q_f decreased to about 1×10^{11} cm^{-2}, D_{it} decreased to the range of

10^{10} $cm^{-2}eV^{-1}$, and the breakdown field histogram peak shifted upward to approximately 7 MV/cm.

These properties are compared with the properties of thermally grown oxides as follows. A 1986 study of thermal gate oxide integrity [80] found a 50 percent failure rate at a field strength of 7.6×10^{6} V/cm. This value is quite close to the histogram peak for post-annealed MPDR-grown oxides shown in Figure 5.6. A 1972 study of D_{it} for thermal oxides [81] found a minimu value of 2×10^{10} $cm^{-2}eV^{-1}$, which is close to the minimum shown for the samples in this study as illustrated in Figure 5.5. A minimum of about 10^{10} $cm^{-2}eV^{-1}$ for D_{it} is still considered state-of-the-art for thermal oxides.

Hamilton and Howard [82], in 1975, reported typical Q_F values of 0.9×10^{11} cm^{-2} for (100)-oriented thermally oxidized silicon. Nicollian and Brews [2] reported in 1982 that a typical value of Q_F was 1.3×10^{11} cm^{-2} for thermal gate oxides in a standard process used for making n-channel MOSFET's. Again, this is quite close to the results reported in this work for MPDR-grown oxides, $Q_F \approx 10^{11}$ cm^{-2}.

The one characteristic of the MPDR-grown oxides which was not found to be as good as present-day thermal oxides was the leakage current, but the leakage in the samples reported here is believed to be due to pinholes in the oxide which most likely resulted from surface contamination unrelated to the actual oxidation process.

Chapter Six

Modeling the Oxidation Kinetics

6.1 Introduction

In this chapter a model of oxidation kinetics is developed and investigated, and the results are compared with qualitatively with some of the results of the MPDR oxidation experiments reported in Chapter Four. The goal of this modeling study is to gain insight into oxidation kinetics in the MPDR, and in particular to develop a greater understanding of the interrelationships among the growth parameters, including anodization voltage and current, oxide voltage, and oxide field.

The model developed in this chapter uses as a starting point the high-field discrete hopping model, including space-charge, which is described in detail in [48]. A brief discussion of the derivation of the discrete hopping model is provided in Section 6.2. The modifications and extensions which have been made to apply the discrete hopping model to the particular case of anodic oxidation of

Si in the MPDR are discussed in Section 6.3. Results of the modeling and comparison with experiment are presented in Section 6.4.

6.2 The High-Field Discrete Hopping Model

The discrete hopping model for one dimensional motion of charged particles through a thin film is illustrated schematically in Figure 6.1. The basis of this model is the idea that particles move through the film by hopping between adjacent potential minima, or wells, which are labeled x_k in Figure 6.1. Particles enter the film at $x = 0$ from an external medium, and the film grows as particles are incorporated at the interface at $x = x_{ox}$. In order to leave a potential well, a charged particle must surmount a barrier of height $(W \pm zqE_k a)$, where the minus sign applies to hopping in the direction encouraged by the electric field (forward hopping), and the plus sign aplies to reverse hopping. The quantity W is the energy barrier between adjacent potential minima in the film in the absence of an applied electric field, which is assumed to be a constant of the material, z is the particle charge number ($z = -1$ for electrons and singly charged negative ions), q is the magnitude of the electronic charge, E_k is the electric field at position x_k in the film, and 2a is the distance between adjacent potential minima. The

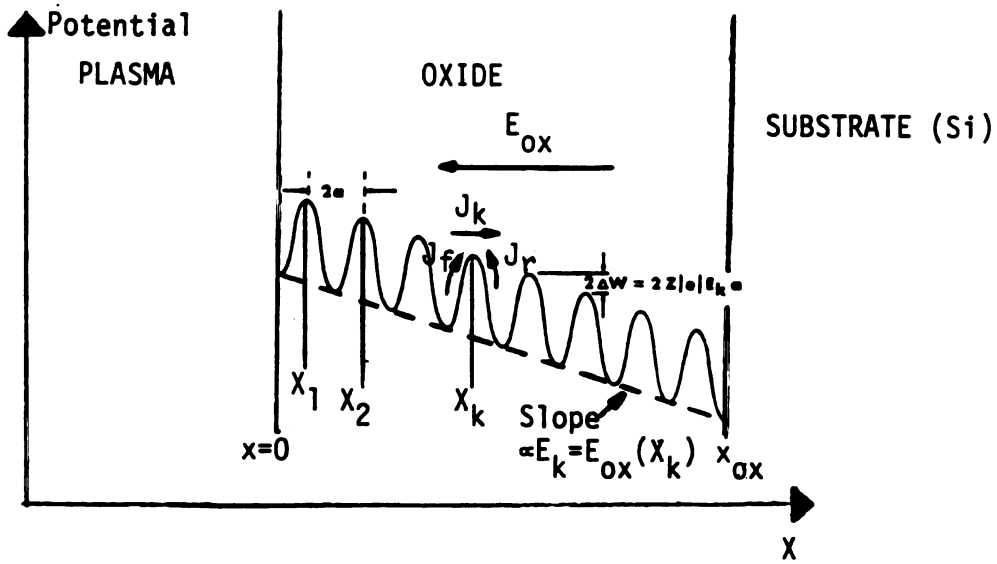

Figure 6.1. Illustration of the discrete hopping model used to model plasma anodic oxidation. The electric field in the oxide is not constant because of the presence of oxide space charge, which is due to the oxidant ion flux.

expressions for forward, reverse, and total particle flux over barrier k are written, according to Boltzmann statistical theory,

$$F_f = n_{k-1}\nu \exp\left[-(W-zqE_k a)/k_B T\right] \qquad [6.1]$$

$$F_r = n_{k-1}\nu \exp\left[-(W+zqE_k a)/k_B T\right] \qquad [6.2]$$

$$F_k = F_f - F_r \quad . \qquad [6.3]$$

Here, F_f is the number of particles per unit area per unit time which cross from the potential well at x_{k-1} to x_k in the positive x direction (toward the substrate interface as defined in Figure 6.1), and F_f is the corresponding flux in the negative x direction. The quantity n_{k-1} is the number of particles per unit area in the k-1st potential well, n_k is the number per unit area in the kth potential well, and ν is the frequency with which the particles attempt to cross the barrier. The Boltzmann constant is denoted by k_B, and T is the absolute temperature of the film, which is assumed constant throughout.

Substituting Equations 6.1 and 6.2 into Equation 6.3 and rearranging yields

$$F_k = \nu \exp(-W/k_B T)\left(n_{k-1}\exp\left[zqE_k a/k_B T\right] - n_k \exp\left[-zqE_k a/k_B T\right]\right) \quad . \qquad [6.4]$$

In [46] it is shown that by making the transformation

$$C(x_k) = (n_{k-1} + n_k)/4a$$

and the approximation

$$C(x_k \pm a) \approx C(x_k) \pm a\left[\frac{\partial C(x)}{\partial x}\right]_{x=x_k} \qquad [6.5]$$

and by in addition requiring continuity of the current (steady state assumption) the discrete Equation 6.4 can be extended into the continuum, with the result that

$$F \approx (D/a)\, C(x)\, \sinh(zqE(x)a/k_BT) - \left[\frac{\partial C(x)}{\partial x}\right] a \cosh(zqE(x)a/k_BT) \qquad [6.6]$$

where F is the steady state particle flux in any cross-sectional plane of the film, $D \triangleq 4a^2\nu \exp(-W/kT)$ is called the migration coefficient, and C(x) is the number of particles per unit area at x.

Equation 6.6 can be simplified for the case of large oxide fields [48] to

$$F = (D/2a)\, C(x) \exp\left[zqE(x)a/k_BT\right] \qquad [6.7]$$

In writing Equation 6.7, the concentration gradient term ($\propto \partial C(x)/\partial x$) in Equation 6.6 has been neglected, and the large-argument limit

$2\sinh(zqE(x)a/k_BT) \rightarrow \exp(zqE(x)a/k_BT)$ has been applied. As discussed further in [48], a sufficient condition for obtaining reasonably accurate quantitative results is

$$|zqE(x)a/k_BT| \geq 2, \quad \text{for } 0 < x < x_{ox} . \qquad [6.8]$$

This constraint will be considered further in the next section.

Continuing with the derivation of the model, the electric field in the film is related to the particle concentration by Poisson's equation in differential form

$$\frac{\partial E}{\partial x} = \frac{zqC(x)}{\epsilon} \qquad [6.9]$$

where ϵ is the permittivity of the film. The surface concentration of particles C(0) is assumed to be externally defined.

Combining Equations 6.9 and 6.7 leads, after some development [48], to the following expressions valid when a constant voltage V_a

is maintained at $x = x_{ox}$:

$$F = [QDC(0)/2a] \exp\left[\frac{V_{ox}}{E' x_{ox}}\right] \qquad [6.10]$$

where

$V_{ox} = V_a - V_s$ (total voltage across the film)

$E' = k_B T/zqa$ (thermal fluctuation field)

$$\ln Q = 1 - \left(\frac{x'}{x_{ox}}\right)\left(1 + \frac{x_{ox}}{x'}\right) \ln\left(1 + \frac{x_{ox}}{x'}\right)$$

(space charge parameter)

$x' = \frac{1}{\lambda C(0)}$ (space charge screening parameter)

$\lambda = \frac{(zq)^2 a}{\epsilon k_B T}$ (scaling parameter).

and V_s, the oxide surface potential, is assumed to be externally defined. In addition, an average electric field in the film may be defined by

$$E_{ox} = V_{ox}/x_{ox}. \qquad [6.11]$$

6.3 Modifications and Extensions of the Basic Model for the Case of Constant Voltage Anodic Oxidation of Silicon in the MPDR

6.3.1 Analytical

The model described by Equations 6.10 and 6.11 in Section 6.2 was modified and extended to apply to the specific experimental system studied in this work, namely, constant voltage anodic oxidation of Si in an MPDR oxygen discharge. Because the model only requires that the charge, z, of the migrating species be given, it is equally valid for any oxygen ion which may be considered to be the principal oxidant species.

At the maximum estimated substrate temperature for the experimental work reported here ($T_{max} \approx 300\ ^{o}C \approx 573\ ^{o}K$), the criterion for quantitative accuracy (Equation 6.8) becomes

$$E(x) \gtrsim \frac{k_B T}{q|z|a} = \frac{2.8}{|z|}\ \text{MV/cm}, \quad 0 < x < x_{ox} . \qquad [6.12]$$

Here, standard values have been used for k_B and q. Following [48], the value used for 2a was the lattice parameter of the anodic film. For the particular case of SiO_2, this was calculated as $2a = (N_{SiO2})^{-1/3}$, where N_{SiO2} is the density of SiO_2 molecules in an amorphous oxide layer. A value of $2.3 \times 10^{22}\ cm^{-3}$ given in [1] was used for N_{SiO2}, resulting in a value for a of 1.8 Å.

In Chapter 4, it was shown that under many of the oxidation conditions studied in the MPDR, 1.5 MV/cm < E_{ox}< 2 MV/cm. Therefore, Equation 6.12 would hold with |z| = 2, but not with |z| = 1. In view of the above considerations, the model was initially applied with z = -2, but after some experience was gained with the model, the case for z = -1 was investigated, and it was determined that the qualitative results remained essentially unchanged.

At this point, it is convenient to rewrite Equation 6.10 and to include the notation previously developed for anodic oxidation:

$$J_i/zq = F_i = [QDC(0)/2a] \exp\left(\frac{V_{ox}}{E' x_{ox}}\right) \qquad [6.13]$$

where J_i is the ionic current in the oxide, and F_i is the ion flux.

In the case of anodic oxidation in an oxygen discharge, the oxidant ion flux in the oxide may be modeled by Equation 6.13. However, as discussed in Chapter Four, the total anodization current is mainly due to electrons, and in the absence of experimental data on $x_{ox}(t)$ it is particularly important for the model to generate curves of total current vs. time for comparison with the experimental results. According to [50], the relatively large electron current in the oxide during plasma anodization is due to the high velocities achieved by electrons under the influence of the oxide field ($\approx 10^7$ cm/s), but the concentration of electrons in the oxide ($\approx 10^{10}$ cm^{-3}) is much lower, in general, than that of the ions, so the

electrons do not make a significant contribution to the space charge in the oxide.

Therefore, for this model the electron contribution to space charge was neglected and the electron current J_e was computed by making the linear approximation

$$J_e \approx J_{e0} + \sigma_e E_{ox} \qquad [6.14]$$

where J_{e0} and σ_e were, in general, determined from experimental data. In order to simplify this analysis, the value of J_{e0} was chosen to be zero (implying a conduction mechanism that was mostly ohmic in nature). The total anodization current in the oxide was modeled as

$$J_a = J_i + J_e \ . \qquad [6.15]$$

An additional consideration in applying the model to oxidation in the MPDR was that the oxide current should be related to the plasma conditions through the measured gold-coated plasma probe characteristics (discussed in Section 4.2). The plasma probe characteristics for a specified set of plasma conditions (microwave

input power and oxygen pressure) were approximated for use in the model by a piecewise linear relationship

$$J_p = V_p\left[\frac{J_{pmax}}{V_{pmax}}\right] \qquad V_p < V_{pmax}$$

$$J_p = J_{pmax} \qquad V_p \geq V_{pmax} \qquad [6.16]$$

where J_p was the probe current measured at probe voltage V_p, and J_{pmax} and V_{pmax} were the maximum values of these quantities measured under the specified conditions. (Values of J_{pmax} and V_{pmax} measured under various conditions in the MPDR are given in Table 4.2.) The oxide surface potential was chosen to simultaneously satisfy Equation 6.15 and Equation 6.16 such that $J_p = J_a$.

At this point, the oxide growth rate can be incorporated into the model. It was assumed that the oxide grows by incorporation of the ions at the reaction interface ($x = x_{ox}(t)$), and that each ion which is transported to the interface according to Equation 6.13 is incorporated into the oxide. Thus

$$\frac{d}{dt}(x_{ox}) = \frac{J_i(t)}{N_i} \qquad [6.17]$$

where N_i is the number of ions per unit volume required to form the oxide, i.e., $N_i = N_{SiO2}/2$ for ions of the form O^{-x}.

A constraint must be imposed upon the value of J_i calculated from Equation 6.13, or else the growth rate given by Equation 6.17

becomes unphysically large, particularly near the beginning of the growth period, when x_{ox} is small. In the model this was accomplished by using for the ion current a value of J_i' given by

$$J_i' = J_i \qquad J_i \leq J_i(max)$$

$$J_i' = J_i(max) \qquad J_i > J_i(max) \qquad [6.18]$$

(In what follows, the distinction between J_i and J_i' will not be made: it will be understood that the modeled value of ion current is subject to the limit in Equation 6.18.) This limit on J_i may be considered tantamount to a reaction-rate imposed limit at the substrate-oxide interface. The typical maximum growth rate used in the model was 200 Å/min. For O^- ions, this corresponds to a maximum ion flux to the interface of 1.8×10^{15} $cm^{-2}s^{-1}$ and a maximum ion current of 290 $\mu A/cm^2$.

6.3.2 Implementation of the Model

An incremental form of the modified high-field discrete hopping model (Equations 6.13 - 6.18) was implemented on a computer. The oxide growth was modeled in increments of thickness Δx_{ox}. Typically Δx_{ox} was chosen to be 50 Å, since it was determined that under most conditions the qualitative results were not changed by increasing the resolution beyond this value. At each growth step, the model outputs included oxidation time, t; oxide thickness, x_{ox}; ion current, J_i;

electron current, J_e; oxide surface potential, V_s; oxide voltage, V_{ox}; and oxide electric field, E_{ox}. The value of current efficiency, η, was also computed as the ratio J_i/J_a.

An order-of-magnitude default value for σ_e was chosen in the following manner: For each oxidation experiment conducted in the MPDR for which the necessary data were available, a value of conductivity was computed by

$$\sigma = \left[J_a(t_f)/E_{ox}(t_f)\right] \qquad [6.19]$$

where $J_a(t_f)$ and $E_{ox}(t_f)$ were the final values of anodization current and oxide field for each experiment. The values of σ for 29 samples ranged from 2.96×10^{-9} $(\Omega\text{-cm})^{-1}$ to 2.84×10^{-8} $(\Omega\text{-cm})^{-1}$, and averaged 1.08×10^{-8} $(\Omega\text{-cm})^{-1}$. (These values are for the case when the oxide is under growth conditions in the plasma, in the presence of a large electric field and exposed to highly energetic electrons. The conductivity of the MPDR oxides after the growth process and after annealing is much lower). The default value of σ_e used in the model was initially chosen to be 1.0×10^{-8} $(\Omega\text{-cm})^{-1}$, since this was close to the average value of σ computed using Equation 6.19.

Default values for the model parameters C(0) and D, which could not be easily estimated from the experimental data, were arrived at by generating model outputs and iteratively adjusting to get order-of-magnitude agreement between model and experiment. A starting point was provided by the values listed in Table I and Table III of [48]. The default values of all parameters used in the model are listed in Table 6.1

Table 6.1 Default parameter values used in the high-field discrete hopping model for modeling oxidation kinetics in the MPDR.

Symbol	Parameter	Default Value
ϵ_{ox}	Permittivity of the oxide	$3.9\epsilon_o$ $= 3.45\times10^{-13}$ F/cm^2
T	Substrate/oxide temperature	300 ^oC
z	charge of oxidant ions	-1
2a	hopping distance and lattice parameter	1.8 Å
σ_e	conductivity of the oxide for electrons	1.5×10^{-8} $(\Omega\text{-cm})^{-1}$
r_{max}	$(dx_{ox}/dt)_{max}$ - growth rate limit	200 Å/s
x_i	initial oxide thickness	50 Å
C(0)	surface concentration of oxidant ions	2×10^{15} cm^{-3}
D	migration coefficient for oxidant ions	1×10^{-9} cm^2/s
J_{pmax}	maximum current from plasma	125 mA/cm^2
V_{pmax}	oxide surface voltage when $J_a = J_{pmax}$	42 V
V_a	anodization potential	30 V

6.4 Modeling Results and Comparison with Experiment

The model investigated here was a relatively simple one based on the fundamental physical processes underlying anodic oxidation. Therefore the comparisons between model results and experimental results will principally be of a qualitative nature. These comparisons will show the successes of the model as well as indicate areas in which the present oversimplifications will benefit from future refinement.

An experimental parameter which appears explicity in Equation 6.13 is the anodization voltage, V_a. A family of model curves with V_a as a parameter is shown in Figure 6.2. This figure shows (a) the oxide thickness x_{ox}, (b) the total current density J_a, (c) the oxide voltage V_{ox}, and (d) the electric field E_{ox} all modeled as a function of time for a 60 min oxidation. The default values listed in Table 6.1 were used for model parameters not otherwise labeled on the figure.

As V_a was increased from 10 V to 50 V, the final oxide thickness generated by the model increased from 700 Å to about 1700 Å, and the modeled values of J_a, V_{ox}, and E_{ox} all increased with V_a at each point in time. The modeled J_a curves (Figure 6.2(b)) may be compared with Figure 4.10. The initial nonlinear decay becomes more pronounced with increasing V_a in both experiment and model. However, the initial saturation-like behavior observed in the experimental curves for $V_a \geq 40$ V is not in evidence in the modeled curves. (This is because the growth rate limit expressed in Equation 6.18 was not reached by any of the curves shown in this figure.) The modeled V_{ox} curves may be compared with Figure 4.16, and the modeled E_{ox} curves

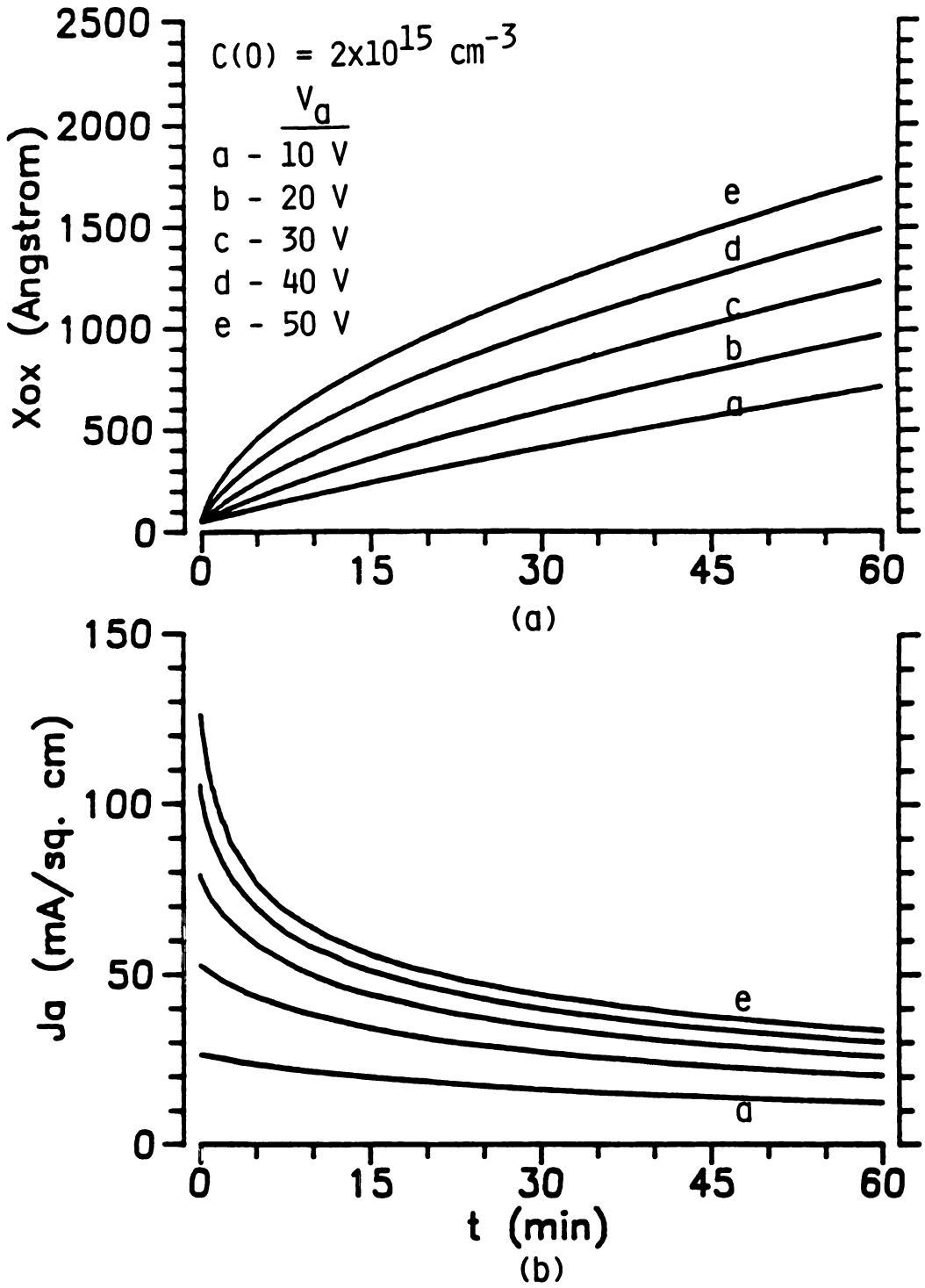

Figure 6.2 (a) Oxide thickness vs. time, and (b) anodization current during oxide growth modeled by the high-field discrete hopping model. The effect of varying V_a is shown, all other model parameters have the default values listed in Table 6.1.

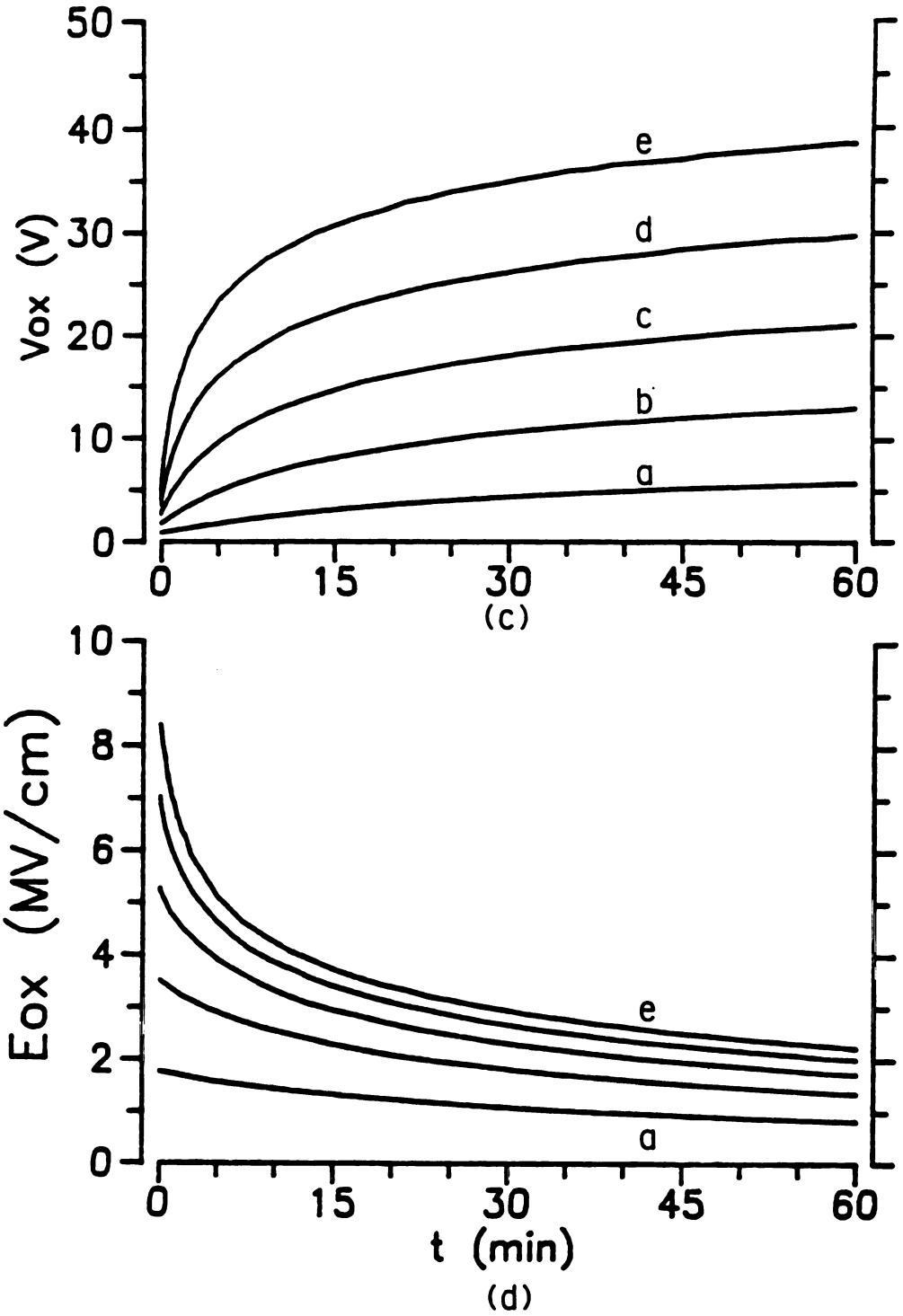

Figure 6.2 (c) Oxide voltage vs. time and (d) oxide electric field vs. time modeled by the high-field discrete hopping model. The effect of varying V_a is shown, all other model parameters have the default values listed in Table 6.1.

shown in Figure 6.2(d) may be compared with Figure 4.20. The initial behavior of the experimental curves is dominated by experimental uncertainty, which prevents meaningful comparison with the model results during the initial growth period. Later, however, there is qualitative agreement between model and experiment in each case. The experimental oxide voltage curves have a form similar to the modeled curves, and, for the last 30 min, they show the same dependence upon V_a. The experimental oxide electric field curves are not as easily distinguished in Figure 4.20 as are the model curves in Figure 6.2(d), but this is because the electric field in the later part of the growth is not greatly dependent upon V_a; this feature is evident in both the experimental and modeled curves. In both cases, E_{ox} is in the range of 1-3 MV/cm for most of the growth period.

The dependence of modeled oxide thickness after a 1 hour growth period upon V_a was investigated, and the results are shown in Figure 6.3, with C(0) as a parameter. This figure may be compared with Figure 4.8. Figure 6.3 shows clearly that x_{ox} increases linearly with V_a for each value of C(0), and that the slope of the linear dependence increases with C(0). Figure 4.8 also indicates a linear dependence for the experimental data, and shows that the slope increases with pressure. It may be noted that (1) modeled x_{ox} increases with C(0), while experimental x_{ox} exhibits a peak with pressure, and (2) the zero-voltage intercept is always positive (the intercept increases with C(0)) for the model, but not for the experimental data.

In order to investigate C(0) further, a series of curves was generated with C(0) as the independent parameter. These curves are shown in Figure 6.4(a)-(d). Oxide thickness is evidently a strong

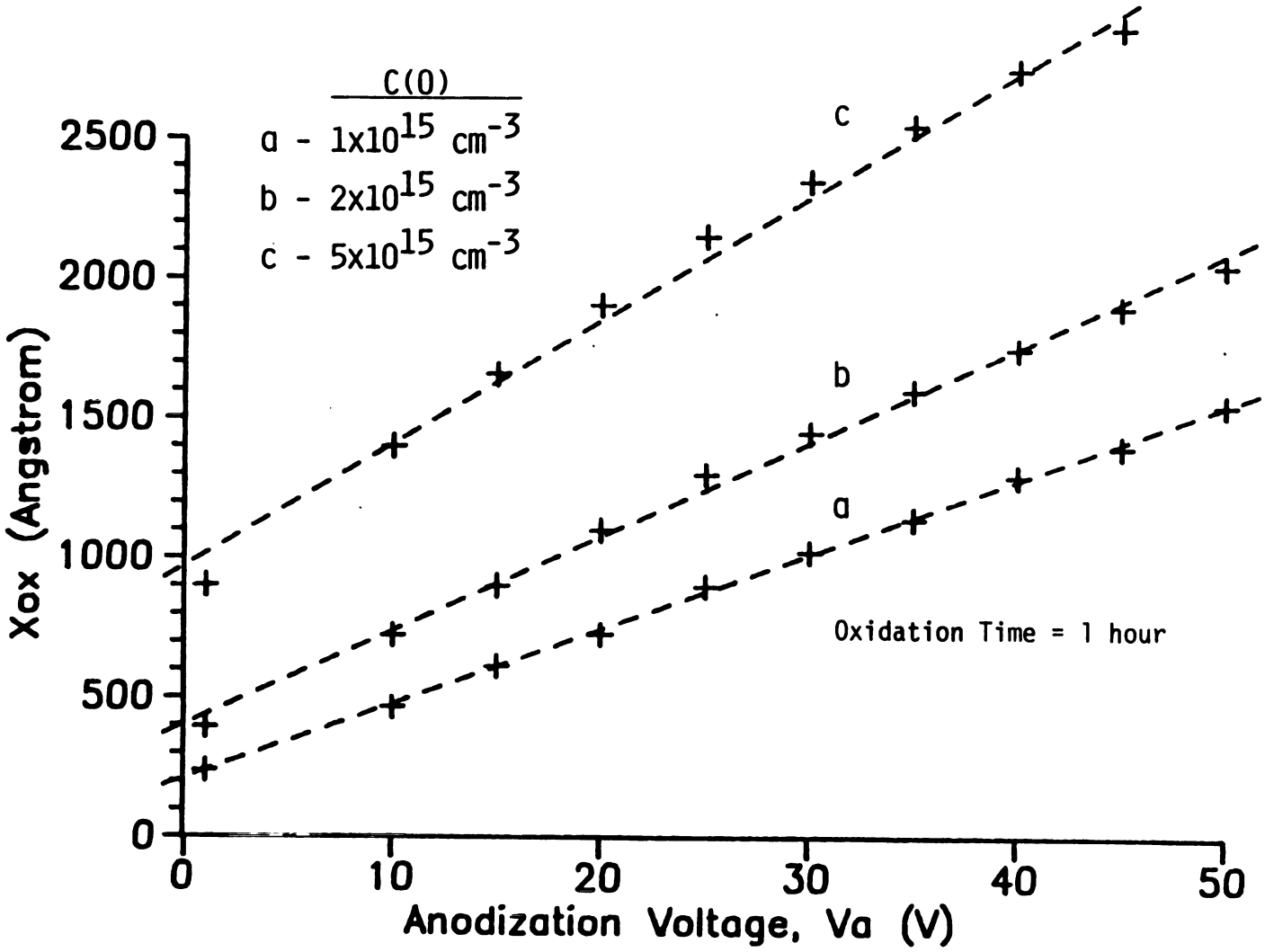

Figure 6.3. Modeled oxide thickness grown in one hour as a function of anodization voltage, for several values of C(0) (ion surface concentration).

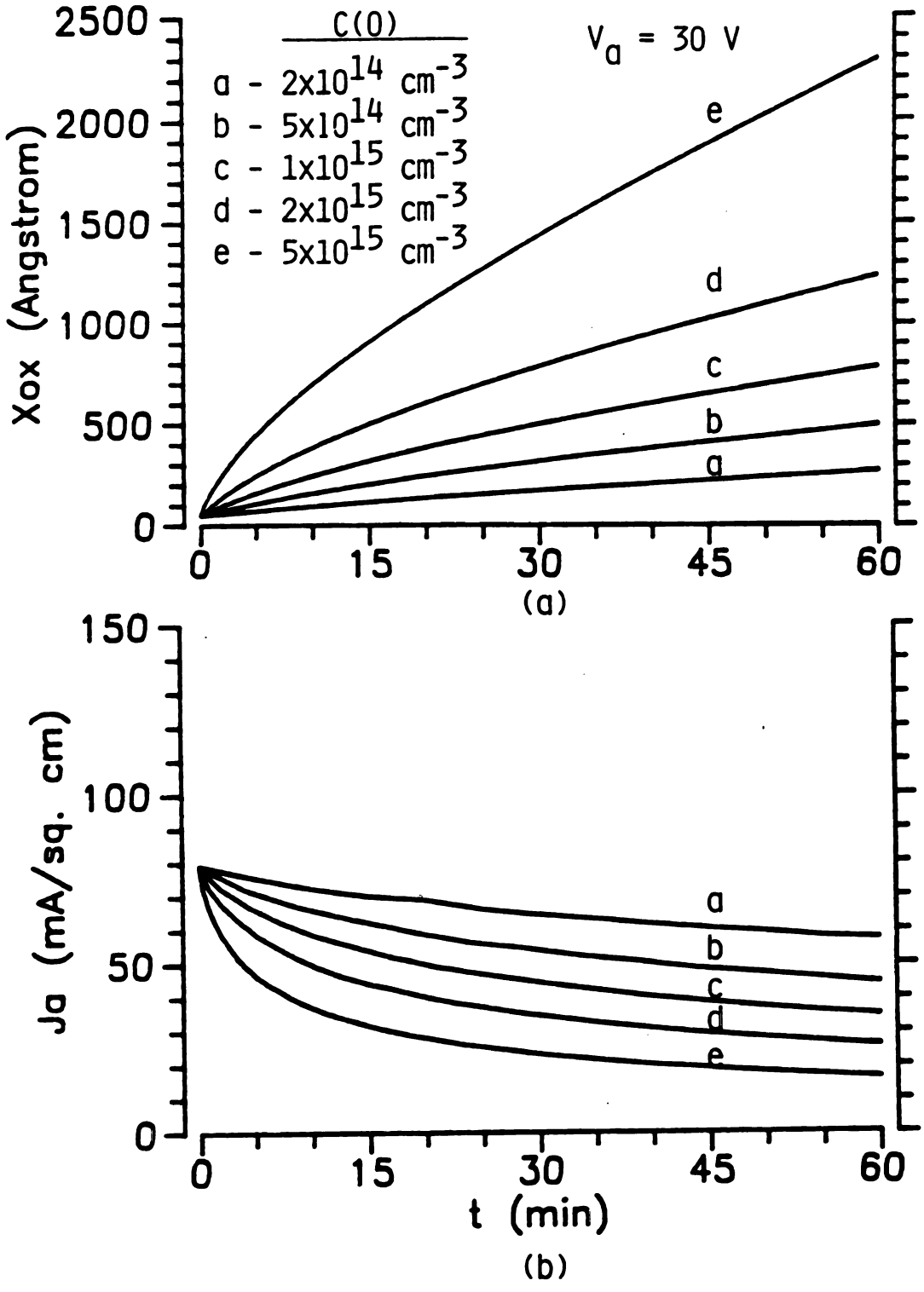

Figure 6.4. (a) Oxide thickness vs. time, and (b) anodization current during growth modeled by the high-field discrete hopping model. The effect of varying C(0) is shown, all other model parameters have the default values listed in Table 6.1.

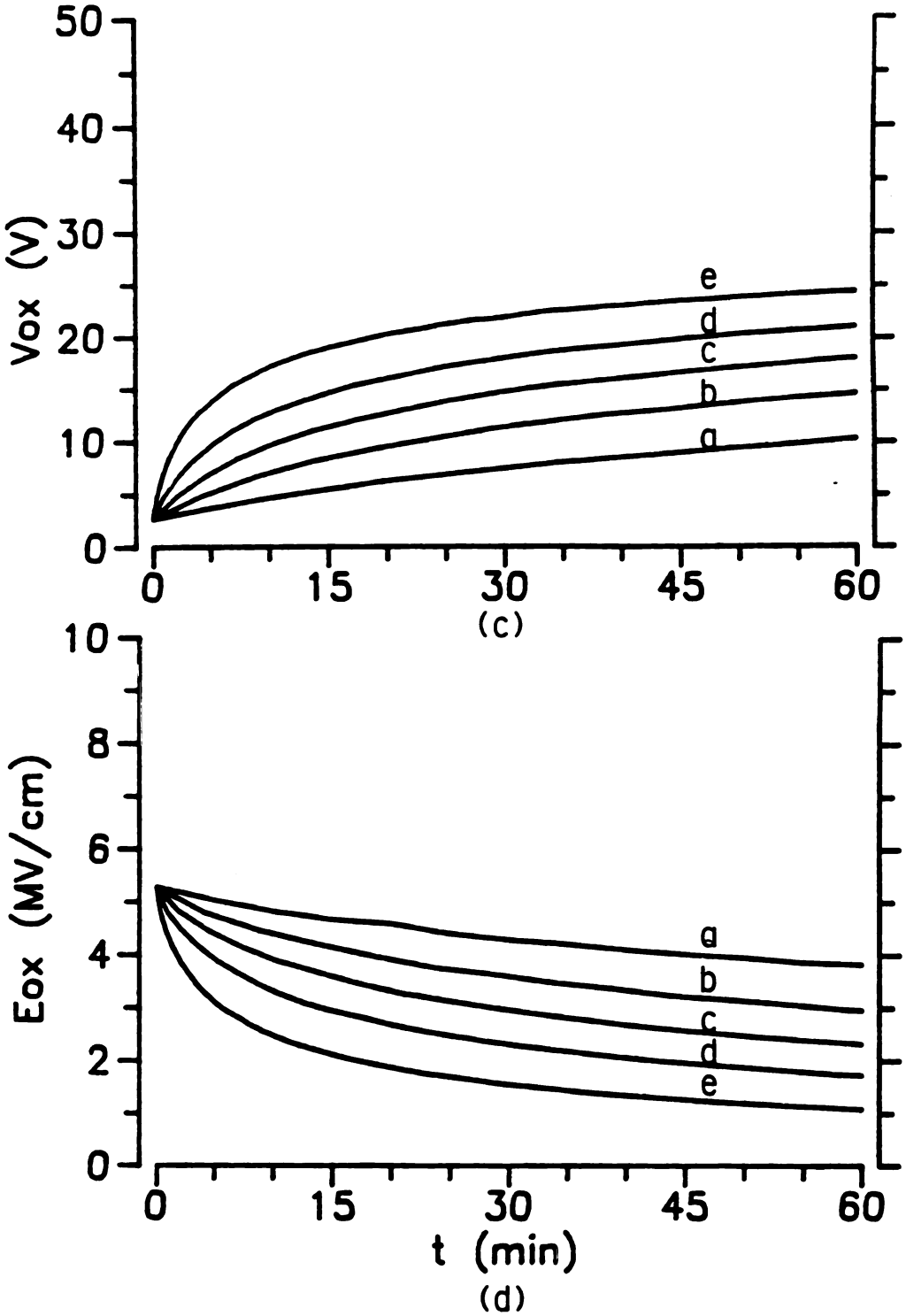

Figure 6.4 (c) Oxide voltage vs. time, and (d) oxide electric field vs. time modeled by the high-field discrete hopping model. The effect of varying C(0) is shown, all other model parameters have the default values listed in Table 6.1.

function of C(0), increasing from about 300 Å to 2300 Å as C(0) increased from 2×10^{14} cm^{-3} to 5×10^{15} cm^{-3} at V_a = 30 V.

It is notable that, as shown in Figure 6.4(b), increasing C(0) caused J_a to decrease. Experimentally, it was found that significant increases in total oxide thickness were always correlated with increased total anodization current. It might be understood from this that C(0) was not an independently controlled parameter in the MPDR oxidation experiments. That is to say, a variation in C(0) effected by a change in, say, pressure is always accompanied by a change in another parameter (oxide surface potential, for example) which results in the observed increase in anodization current.

The effect of C(0) on J_a can be understood this way: as C(0) increases, a reduced electric field suffices to drive the same ion flux across the oxide. Thus, the same growth rate requires a smaller total current J_a. This explanation is confirmed by Figure 6.4(d), which shows that E_{ox} decreases with increasing C(0).

The effect of pressure was considered by replacing the default values of J_{pmax} and V_{pmax} in Table 6.1 by experimental values from Table 4.2 that corresponded to pressures in the range from 30 to 100 mTorr. The results are shown in Figure 6.5, and may be compared with Figure 4.12 (30 V curve). Model and experiment both show a peak, however, the model peak is at 50 mTorr, and it is considerably less pronounced than the peak in the experimental data which occurs at 70 mTorr. Comparison of these curves indicates the effect of pressure is not represented solely by J_{pmax} and V_{pmax}.

As discussed in Section 2.4, oxide growth rates in plasma oxidation experiments reported in the literature are often specified by parabolic rate constants, by analogy with the approximation for

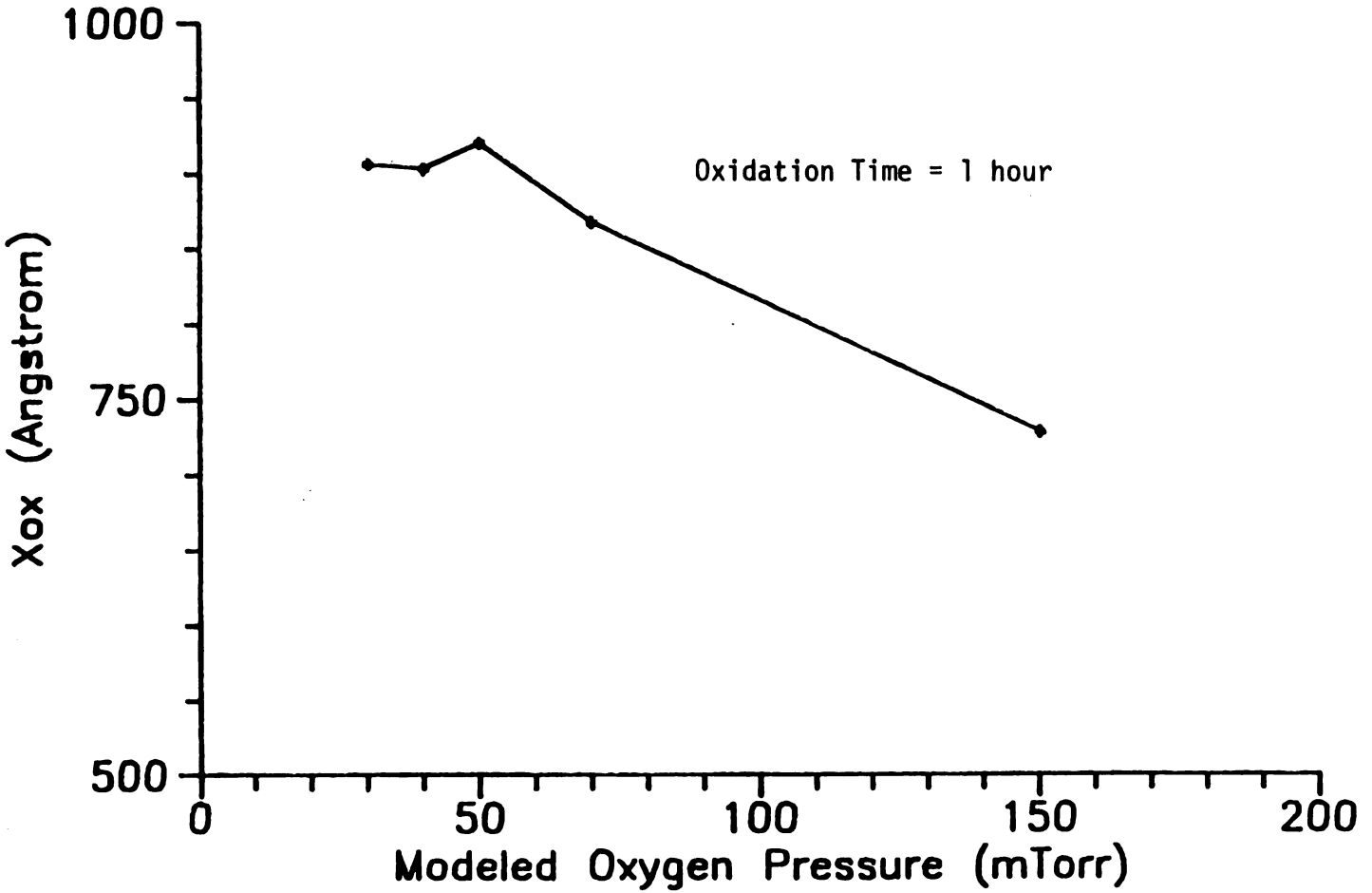

Figure 6.5 Modeled oxide thickness grown in one hour as a function of modeled oxygen pressure (oxygen pressure was modeled by replacing the default values of J_{pmax} and V_{pmax} by the values measured at each pressure in the gold-probe experiments (Table 4.2)).

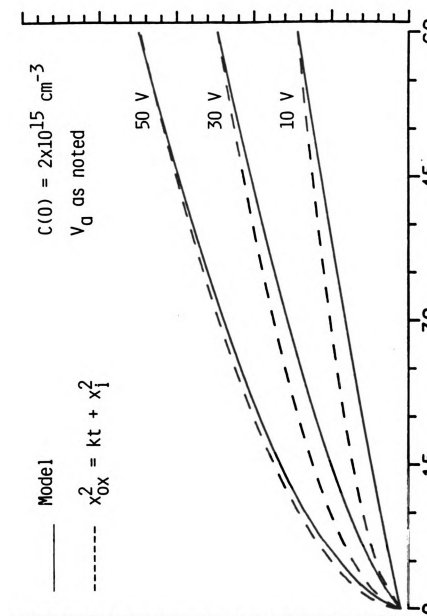

Figure 6.6. Model-generated oxide growth curves compared with calculated parabolic growth curves, at several values of anodization potential.

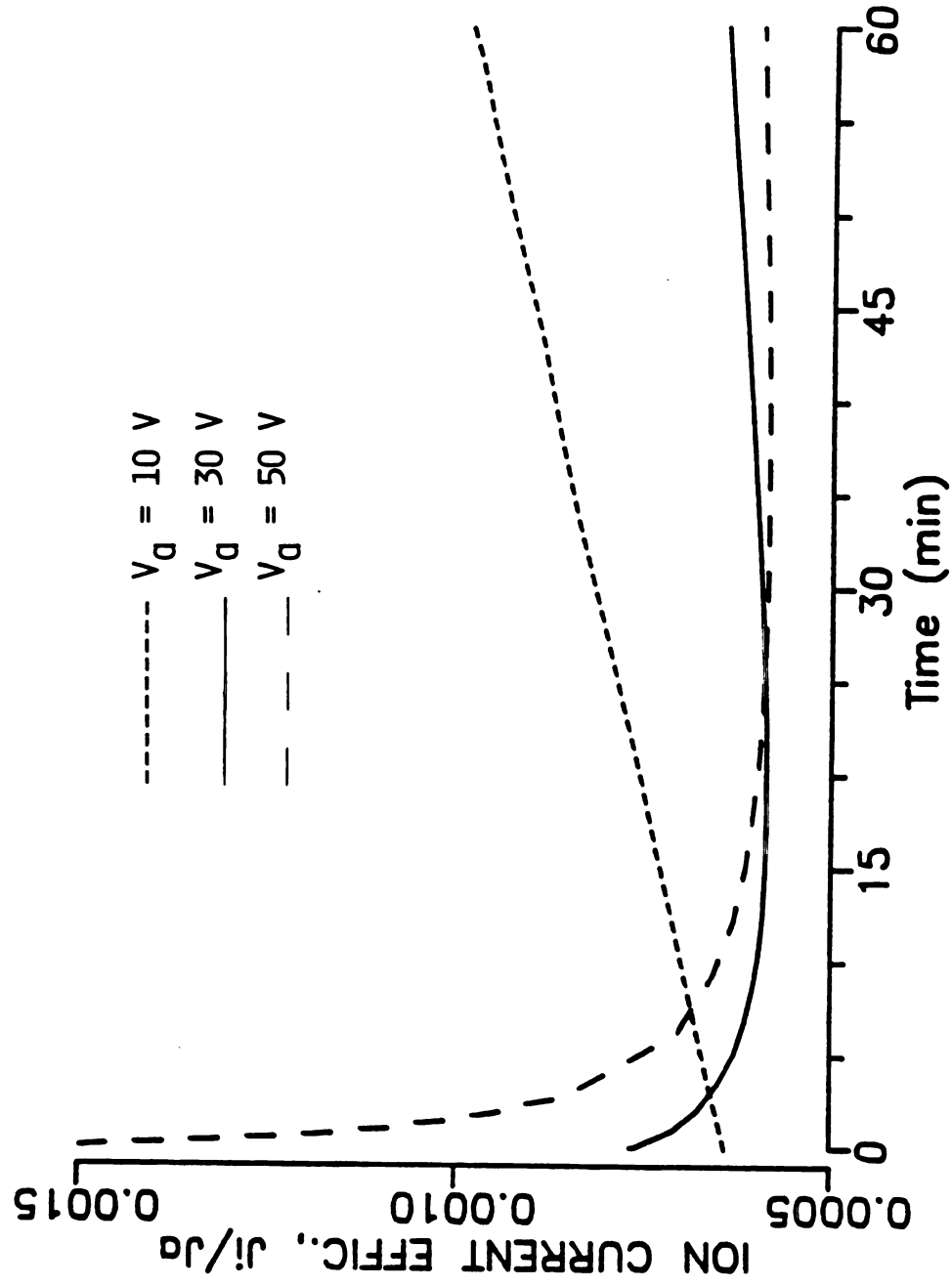

Figure 6.7. Model-generated curves of ion current efficiency vs. time, for several values of anodization voltage.

thermal oxidation given by Equation 2.10. Figure 6.6 shows a comparison of modeled oxide growth curves with calculated parabolic growth curves for V_a = 10 V, 30 V, and 50 V. The parabolic growth curves were computed from $x_{ox}^2 = kt + x_i^2$, where the value used for the initial oxide thickness, x_i, was 50 Å and k was determined from the final oxide thickness (at t = 60 min) generated by the model. Evidently, in each case the initial growth rate predicted by the model is slower than parabolic, but the growth becomes more parabolic in form as V_a increases. The curves for V_a = 10 V and V_a = 30 V bothes show significant deviation from parabolic growth over most of the growth period.

As discussed in Chapter Four, values of the ion current efficiency, η, are in general reported to be very small for plasma anodization. Figure 6.7 shows the modeled ion current efficiency, η, as a function of time for several values of V_a; under all conditions investigated, η was less than 0.002. The modeled values may also be compared with time-averaged values of η reported in [75] for some of the MPDR samples, which ranged from 3.4×10^{-4} to 5.4×10^{-4}.

Chapter Seven

Conclusions and Recommendations

7.1 Summary of the Major Results

7.1.1 Oxide Growth Rate and Plasma Properties

Anodic oxidation of silicon in a microwave plasma disk reactor (MPDR) was studied. Oxidation occurred in oxygen microwave discharges formed in the TE_{211} cavity resonant mode of excitation at f = 2.45 GHz. The discharge confinement region was 118 cm^3, and the surface area of a typical oxide sample was 1.27 cm^2. Substrate temperature was estimated to be in the range 200 - 300 ^oC. Oxygen pressure was in the range from 30 - 150 mTorr, microwave power was in the range from 80 - 140 W, and anodization voltage was in the range from 18 - 50 V.

Oxidation was observed to occur over the entire range of each parameter investigated, although the rate of oxidation depended upon the choice of experimental conditions. Observed parabolic rate

constants were in the range $4.2\times10^3 < k < 8.1\times10^4$ Å^2/min, where k was calculated from the measured value of oxide thickness, x_{ox}, and the oxidation time, t, as $k = x_{ox}^2/t$.

In the range of parameter values studied, the greatest variation of oxidation rate was achieved by varying the anodization voltage, V_a. Varying the oxygen pressure, p, influenced the oxidation rate to a lesser extent, and varying the microwave power P to the plasma had little effect on the oxidation rate. It should be emphasized with regard to the latter observation that the range of power investigated here was rather limited, and that since most plasma properties (e.g., electron density and electron temperature) depend in a highly non-linear manner upon power (or more accurately, power density) it might be that by expanding the range of power explored, more pronounced effects on oxide growth would be observed.

The thickness of oxide films formed in the MPDR during 1 h oxidation experiments were recorded, and the effects of varying the oxidation conditions were studied. Oxide thickness increased approximately linearly with anodization voltage. At 40 mTorr and 100 W, x_{ox} increased from 500 Å at 18 V to 1500 Å at 50 V. A similar dependence was observed at other pressures. At the outset of this study it was hypothesized that the principal effect of increasing the anodization voltage would be to increase the oxide electric field, thereby enhancing the migration of negative oxygen ions to the Si-SiO_2 reaction interface. However, the results of computing the oxide surface potential and oxide electric field for many of the samples (Chapter Four) indicated that the oxide electric field was not very strongly dependent upon anodization voltage, unless V_a was less than a critical value (in the range 20 - 30 V for the conditions

studied). Instead, increasing the anodization voltage caused the oxide surface potential to increase, which in turn probably (a) increased the surface concentration of negatively charged species from the plasma, including electrons as well as oxidant ions, and (b) supplied energy for surface reactions, such as electron attachment to adsorbed oxygen, which are known to play an important role in plasma oxidation kinetics.

The measured oxide thickness was maximum at an oxygen pressure of about 70 mTorr. At 40 V and 100 W, x_{ox} at 70 mTorr was 1900 Å, about 50 percent greater than its value at 30 mTorr or 150 mTorr. Pressure is expected to affect the oxidation process in two ways: (1) plasma density varies with pressure, changing the concentration of electrons and ions in the plasma and thereby changing the concentration gradients across the oxide film, and (2) as the neutral gas pressure varies, the mean free paths and collision rates in the plasma and at the oxide surface are modified.

In order to further investigate the effect of plasma properties on oxide growth in the MPDR, plasma density was measured as function of oxygen pressure and microwave power using a double Langmuir probe. Values of measured plasma density were on the order of 10^{12} cm^{-3}, ranging from 4×10^{11} cm^{-3} (80 W, 150 mTorr) to 1.5×10^{12} cm^{-3} (110 W, 30 mTorr). Plasma density was observed to decrease with increasing pressure over the entire pressure range investigated; therefore, a direct correlation between oxide thickness and plasma density (e.g., due to an increased surface concentration of active species) of the unperturbed plasma was ruled out. However, another series of probe experiments was carried out using a gold-coated silicon substrate. The surface area of this probe was the same as that of the substrates

used in the oxidation experiments, and about 20 times that of the total exposed area of the double Langmuir probe. The typical current drawn by the large area gold probe was on the order of 100 mA, three orders of magnitude larger than that drawn by the double Langmuir probe. The variation of plasma properties with pressure measured using this probe was qualitatively different than that measured using the double Langmuir probe. In particular, the probe saturation current density exhibited a peak at around 50 mTorr, in a manner similar to the oxide thickness. It was concluded from this that the plasma properties in the MPDR are significantly modified by the presence of a substrate undergoing anodization. It has not been determined whether this modification is due mainly to the extraction of anodization current, or to other factors such as modification of the electric field distribution and/or the gas flow stream, or the presence of an additional surface for electron-ion recombination.

The microwave input power to the plasma affected the measured plasma properties, as well as the oxide surface potential, and the oxide electric field. Plasma density increased (according to both types of probe measurements) with microwave power. The effect on oxide surface potential and electric field was more complicated, as indicated in Figures 4.18 and 4.22. This is perhaps fundamental to understanding the lack of observed correlation between microwave input power and oxide thickness.

The oxide surface potential for a number of samples was deduced by correlating probe measurements with recorded values of anodization current. By assuming a parabolic growth law, $x_{ox}^2 = kt$, as well as related upper and lower bounds on $x_{ox}(t)$, reasonable approximations and bounds were computed for the oxide electric field during growth.

The oxide field was found to be in the range 1 - 2 MV/cm under most of the conditions studied. Exceptions to this occurred mainly during the initial growth period, when the field was larger.

7.1.2 Oxide Characterization

Visual inspection of the samples revealed generally uniform oxide thickness over a region comprising about 95 percent of the sample area; this region was usually surrounded by a series of narrow rings of decreasing thickness extending to the unoxidized substrate. The total oxidized area was always slightly less than the opening in the oxidation mask.

Pinholes were observed on most of the oxide samples. In general, the pinholes were near-perfect circles about 10 μm in diameter, and most had a dark spot in the center. A likely explanation for the pinholes is that the substrate surfaces were contaminated by adhesion of particulates before, or possibly during installation in the MPDR. This might have been caused by atmospheric dust, since the samples were not prepared in a clean-room environment. It is also possible that an undetected source of contamination existed inside the discharge chamber. This problem will be addressed in future investigations.

Some oxide samples were grown on substrates mounted on a pedestal outside the discharge enclosure, below the baseplate. Although oxidation occurred in this configuration at rates similar to those observed for samples mounted in the discharge zone, there was visual evidence of bombardment by large particulates on these

samples. Only a few samples were grown in this arrangement, and the source of this contamination was not be identified. However, this is considered to be a practical problem which can be solved, and it should not deter future investigation of this mode of sample preparation, which may offer significant advantages due to reduced radiation and hot electron damage to the oxide film.

MOS C-V measurements on the plasma oxide samples yielded oxide fixed charge densities, Q_f, in the range of 4×10^{11} cm^{-2} to 1×10^{12} cm^{-2} for as-grown films. On the as-grown sample with lowest Q_f, computation of interface state density from the C-V data yielded a mid-gap minimum value of $D_{it} = 2\times10^{11}$ $cm^{-2}eV^{-1}$.

The effects of annealing were studied on these samples. Devices which underwent a hydrogen (forming gas) anneal (5% H_2, 95% N_2, 1 h) showed marked improvement in both Q_f and D_{it}. For the sample referenced above, Q_f was reduced to 1×10^{11} cm^{-2} and the minimum value of D_{it} was reduced to about 1.8×10^{10} $cm^{-2}v^{-1}$. For state-of-the art thermal oxides, a typical value for Q_{it} plus Q_f is 1.5×10^{11} cm^{-2} [83], about the same as is the case for the plasma oxides reported here.

I-V measurements on the MOS capacitors were used to investigate oxide leakage conduction and breakdown strength. Oxide leakage current was found to be on the order of 10^{-3} A/cm^2 prior to annealing, and was reduced to the order of 10^{-5} A/cm^2 by annealing in forming gas. This post-anneal value is undesirably large, and apparently resulted at least in part from oxide pinholes. Energy will be devoted in future work toward achieving a reduction in this quantity of several orders of magnitude.

The dc breakdown fields measured for devices on as-grown samples were clustered mostly in the range 1 - 2 Mv/cm. After annealing in forming gas, the breakdown field cluster shifted substantially upward to the range 6 - 8 MV/cm, which is about the same as measured for good quality thermal oxides.

7.1.3 Modeling of the MPDR Oxidation Kinetics

Oxidation in the MPDR was modeled using a high-field discrete hopping model. The model predicted qualitatively the dependence of oxide thickness, anodization current, oxide voltage, and oxide electric field upon anodization voltage. In addition, reasonable quantitative results were obtained for the ranges of values covered by each of these parameters.

A linear dependence of oxide thickness upon anodization was predicted by the model, in agreement with the experimental results.

Investigation of the effects of the model parameters C(0), J_{pmax} and V_{pmax} on modeled oxide growth indicated that, while each was correlated to some extent with oxygen pressure in the MPDR, the experimentally observed effects of pressure could not be satisfactorily accounted for by these parameters alone.

Modeled oxide growth curves were compared with calculated parabolic growth curves at several different values of anodization voltage. For each value of anodization voltage the oxide thickness was somewhat lower than that predicted by parabolic growth for the entire 60 min duration investigated, but the oxide growth was found

to become more parabolic in nature with increasing anodization voltage in the range from 10 to 50 V.

The ion current efficiency, η, predicted by the model was found to be very low, ranging from about 6×10^{-4} to 2×10^{-3} for anodization voltages in the range from 10 to 50 V. This range is in agreement with the efficiencies deduced from experimental results and with those reported in the literature.

7.2 Recommendations for Future Work

The following specific recommendations for continuation of various aspects of this work are provided:

(i) An important contribution would be made by investigating selective oxidation through various masks (photoresist, Al, Si_3N_4, etc.) and fabricating FET's with MPDR-grown gate oxides. It might be noted here that in VLSI processing for gate oxides, the oxide growth rate is not the important parameter. Rather, of primary interest is how much control can be exerted over the growth of thin (100 Å), uniform films.

(ii) The range of microwave power investigated should be extended to at least 500 W, and perhaps more. This would allow the regime of very high plasma density to be investigated, and would also permit the investigation of lower pressure discharges.

(iii) The MPDR substrate holder should be redesigned to facilitate monitoring and controlling the substrate temperature. The design should provide for cooling as well as heating, since the substrate temperature will increase as the input power is increased.

(iv) Oxidation with the substrate mounted below the MPDR baseplate could be investigated. There is a possibility for improved oxide properties due to reduced radiation damage.

(v) Oxidation of larger substrates should be investigated, and detailed analysis of the resulting oxide uniformity should be conducted. The growth of large area, uniform films is particularly important in VLSI processing applications.

(vi) A significant experimental challenge would be to design an MPDR oxidation reactor in which x_{ox} could be measured in situ as a function of time. The MPDR cavity could be fitted with optical entrance and exit ports (perhaps movable) to allow the use of an ellipsometer.

(vii) It would be very helpful to develop a comprehensive model, preferably by using a hybrid numerical-analytical approach, for anodic oxide formation on Si. The basis for this work might be found in [45-48,50,84].

(viii) Oxide electrical characterization could be extended by using both low- and high- frequency C-V techniques, and by using

conductance techniques [2] to measure interface state properties. Other oxide properties reported in the literature are measured by a variety of surface analysis techniques, including scanning electron microscopy (SEM), ellipsometery, electron-spin resonance (ESR), IR absorption, and X-ray diffraction, to name a few.

(ix) Many interesting experiments can be devised or have been suggested in the literature, which have to do with investigating oxidation kinetics. Any of these could be applied to oxidation experiments in the MPDR. Examples include ^{18}O tracer experiments [16], rf-biasing the substrate to reduce the negative ion flux to the oxide [29], and the use of thin overlay films on the oxide [37].

LIST OF REFERENCES

LIST OF REFERENCES

1. R. A. Colclaser, Microelectronics Processing and Device Design, Wiley and sons, New York, 1980.

2. E. H. Nicollian and J. R. Brews, MOS (Metal Oxide Semiconductor) Physics and Technology, Wiley and Sons, New York, 1982.

3. J. Nulman, J. P. Krusius, and A. Gat, "Rapid thermal processing of thin gate dielectrics. -Oxidation of silicon," IEEE Electron Device Lett., EDL-6 (5), 1985.

4. I. W. Boyd and J. I. B. Wilson, "CO_2 laser oxidation of silicon," Physica, 117B, 1983.

5. S. A. Schafer and S. A. Lyon, "Optically enhanced oxidation of semiconductors," J. Vac. Sci. Technol., 19 (3), 1981.

6. E. Bassous, H. N. Yu, and V. Maniscalco, "Topology of silicon structures with recessed SiO_2," J. Electrochem. Soc., 123 (11), 1976.

7. V. Q. Ho and T. Sugano, "Selective anodic oxidation of silicon in oxygen plasma," IEEE Trans. Electron Dev., ED-27 (8), 1980.

8. A. G. Revesz, "The defect structure of grown silicon dioxide films," IEEE Trans. Electron Dev., ED-12 (3), 1965.

9. W. A. Tiller, "On the kinetics of the thermal oxidation of silicon II. Some theoretical evaluations," J. Electrochem. Soc., 127 (3), 1980.

10. S. Gourrier and M. Bacal, "Review of oxide formation in a plasma," Plasma Chem. and Plasma Process., 1 (3), 1981.

11. S. Kimura, E. Murakami, K. Miyake, et.al., "Low temperature oxidation of silicon in a microwave-discharged oxygen plasma," J. Electrochem. Soc., 132 (6), 1985.

12. J. Kraitchman, "Silicon oxide films grown in a microwave discharge," J. Appl. Phys., 38 (11), 1967.

13. J. L. Moruzzi, A. Kiermasz, and W. Eccleston, "Plasma oxidation of silicon," Plasma Phys., 24 (6), 1982.

14. J. R. Ligenza and M. Kuhn, "DC arc anodic plasma oxidation- a new vacuum process for solid state device fabrication," Solid State Technol., Dec. 1970.

15. F. Rochet, B. Agius, and S. Rigo, "An $^{18}O_2$ study of the oxidation mechanism of silicon in dry oxygen," J. Electrochem Soc., 131 (4), 1984.

16. J. Perriere, J. Siejka, and R. P. H. Chang, "Study of oxygen transport processes during plasma anodization of Si between room temperature and 600 C," J. Appl. Phys., 56 (10), 1984.

17. R. A. Smith, Semiconductors, 2nd Ed., Cambridge University Press, Cambridge, 1978.

18. D. K. Reinhard, Introduction to Integrated Circuit Engineering, Houghton-Mifflin, Boston, In press.

19. L. M. Terman, "An investigation of surface states at a silicon/silicon oxide interface employing metal-oxide-silicon diodes," Solid State Electron., 5, 285-299, 1962.

20. C. N. Berglund, IEEE Trans. Electron Dev., ED-13, 1966.

21. E. H. Nicollian and A. Goetzberger, "The Si-SiO_2 interface-electrical properties as determined by the metal-insulator-silicon conductance technique," Bell Syst. Tech. J., 46 (6), 1967.

22. P. J. Jorgensen, "Effect of an electric field on silicon oxidation," J. Chem. Phys., 37 (4), 1962.

23. B. E. Deal, "The oxidation of silicon in dry oxygen, wet oxygen, and steam," J. Electrochem. Soc., 110 (6), 1963.

24. B. E. Deal and A. S. Grove, "General relationship for the thermal oxidation of silicon," J. Appl. Phys., 36 (12), 1965.

25. D. O. Raleigh, J. Electrochem. Soc., 113, 1966.

26. W. A. Tiller, "On the kinetics of the thermal oxidation of silicon I. A theoretical perspective," J. Electrochem. Soc., 127 (3), 1980.

27. J. R. Ligenza, "Silicon oxidation in an oxygen plasma excited by microwaves," J. Appl. Phys., 36 (9), 1965.

28. J. L. Miles and P. H. Smith, "The formation of metal oxide films using gaseous and solid electrolytes," J. Electrochem. Soc., 110 (12), 1963.

29. J. F. O'Hanlon and W. B. Pennebaker, "Negative ion extraction from the plasma during anodization in the dc oxygen discharge," Appl. Phys. Lett., 18 (12), 1971.

30. M. A. Copeland and R. Pappu, "Comparative study of plasma anodization of silicon in a column of a dc glow discharge," Appl. Phys. Lett., 19 (6), 1971.

31. A. K. Ray and A. Reisman, "The formation of SiO_2 in an RF generated oxygen plasma II. The pressure range above 10 mTorr," J. Electrochem. Soc., 128 (11), 1981.

32. G. Loncar, J. Musil, and L. Bardos, "Present status of thin oxide films creation in a microwave plasma," Czech J. Phys., B30, 688-707, 1980.

33. L. Bardos, G. Loncar, I. Stoll, J. Musil, and F. Zacek, "A method of formation of thin oxide films on silicon in a microwave magnetoactive plasma," J. Phys. D, 8, 1975.

34. L. Bardos and J. Musil, "Microwave generation of a magnetoactive oxygen plasma for oxidation," Journal de Physique, 40 (C7), 1979.

35. L. Bardos, J. Musil, F. Zacek, and L. Hulyeni, "The negative role of the fast electrons in the microwave oxidation of silicon," Czech J. Phys., B28, 1978.

36. J. Musil, F. Zacek, L. Bardos, et. al, "Plasma oxidation of silicon in a microwave discharge and its specificity," J. Phys. D, 12, 1979.

37. S. Gourrier, P. Dimitriou, and J. B. Theeten, "Enhanced plasma oxidation at low temperature using a thin solid electrolyte," Appl. Phys. Lett., 38 (1), 1981.

38. R. P. H. Chang, C. C. Chang, and S. Darack, "Fluorine-enhanced plasma growth of native layers on silicon," Appl. Phys. Lett., 36 (12), 1980.

39. K. Miyake, S. Kimura, T. Warabisako, et. al, "Microwave plasma stream transport system for low temperature plasma oxidation," J. Vac. Sci. Technol., A2 (2), 1984.

40. A. K. Ray and A. Reisman, "Plasma oxide FET devices," J. Electrochem. Soc., 128 (11), 1981.

41. V. Q. Ho and T. Sugano, "An improvement of the interface properties of plasma anodized SiO_2/Si system for fabrication of MOSFET's," IEEE Trans. Electron Devices, ED-28, 1060-1065, 1981.

42. S. Kimura, E. Murakami, and T. Warabisako, "FET's with gate oxides formed in a low temperature microwave plasma stream," IEEE Electron Device Letters, EDL-7 (1), 1986.

43. D. L. Pulfrey and J. J. Reche, "Preparation and properties of plasma-anodized silicon dioxide films," Solid State Electron., 17, 627-632, 1974.

44. J. F. O'Hanlon, "Plasma anodization of metals and semiconductors," J. Vac. Sci. Technol., 7 (2), 1969.

45. N. Cabrera and N. F. Mott, "Theory of the oxidation of metals," Rept. Prog. Phys., 12 (163), 1949.

46. A. T. Fromhold and E. L. Cook, "Diffusion currents in large electric fields for discrete lattices," J. Appl. Phys., 38 (4), 1967.

47. A. T. Fromhold and J. Kruger, "Space-charge and concentration-gradient effects on anodic oxide film formation," J. Electrochem. Soc., 120 (6), 1973.

48. A. T. Fromhold, "Single carrier steady-state theory for formation of anodic films under conditions of high space charge in very large electric fields," J. Electrochem. Soc., 124 (4), 1977.

49. D. L. Pulfrey, F. G. M. Hathorn, and L. Young, "The anodization of Si in an RF plasma," J. Electrochem. Soc., 120 (11), 1973.

50. P. Friedel, S. Gourrier, and P. Dimitriou, "Kinetics of GaAs plasma anodization," J. Electrochem. Soc., 128 (9), 1981.

51. J. Asmussen, J. Root, and S. Nakanishi, "performance characteristics of a microwave plasma disk ion source," Michigan State University Publication MSU-ENG-82-026, 1982

52. J. Asmussen and J. Root, "The characteristics of a microwave plasma disk ion source," Appl. Phys. Lett., 44 (4), 1984.

53. J. Asmussen and D. K. Reinhard, "Method for treating a surface with a microwave or UHF plasma and improved apparatus," U.S. Patent 4,585,668, April 1986.

54. J. Asmussen, M. Raghuveer, J. R. Hamaan, and H. C. Park, "The design of a microwave plasma cavity," Proc. IEEE, 62 (1), 1974.

55. A. D. McDonald and S. J. Tetenbaum, "Chapter3. High Frequency and Microwave Discharges," in Gaseous Electronics, Vol. I, M. Nattirsh and H. J. Oskem, Ed.'s, Academic Press, New York, 1978.

56. J. Root and J. Asmussen, "Recent work on a microwave ion source," presented at the 17th Int. Electric Propulsion Conf., Tokyo, 1984.

57. M. Dahimene and J. Asmussen, "The performance of microwave ion source immersed in a multicuspstatic magnetic field," J. Vac. Sci. Technol., B4 (1), 1986.

58. S. Whitehair, J. Asmussen, and S. Nakanishi, "Experiments with a microwave electrothermal thruster concept," presented at the 17th Int. Electric Propulsion Conf., Tokyo, 1984.

59. J. Root and J. Asmussen, "Experimental performance of a microwave cavity plasma disk ion source," Review of Scientific Instruments, 56 (8), 1985.

60. J. Asmussen and J. Root, "Ion Generating Apparatus and Method for the use thereof," U.S. Patent 4,507,588, March 1985.

61. J. Asmussen and M. Dahimene, "The experimental test of a microwave ion beam source in oxygen," accepted for publication in J. Vac. Sci. Technol., B5, Jan. 1987.

62. T. Roppel, D. K. Reinhard, and J. Asmussen, U. S. Patent Applied for by Michigan State University, June 12, 1986, Serial Number 873,694.

63. R. F. Harrington, Time-Harmonic Electromagnetic Fields, McGraw-Hill, New York, 1961.

64. C. S. Lee, S. W. Lee, and S. L. Chuang, "Plots of modal field distribution in rectangular and circular waveguides," IEEE Trans. Microwave Theor. Tech., MTT-33 (3), 1985.

65. J. Rogers, Properties of Steady-State, High Pressure Argon Microwave Discharges, Ph.D. Dissertation, Michigan State University, 1982.

66. C. J. Mogab, "Chapter 8: Dry Etching," in VLSI Technology, S. M. Sze, Ed., McGraw-Hill, New York, 1983.

67. L. D. Bollinger, "Ion beam etching with reactive gases," Solid State Technology., 26, 1983.

68. D. K. Reinhard, J. Asmussen, et. al, NSF Grant No. CBT-8413596, work in progress at Michigan State University.

69. A. K. Ray and A. Reisman, "The formation of SiO_2 in an RF generated oxygen plasma I. The pressure range below 10 mTorr," J. Electrochem. Soc., 128 (11), 1981.

70. N. Yokoyama, T, Mimura, K. odani, and M. Fukuta, "Low temperature plasma oxidation of GaAs," Appl. Phys. Lett., 32 (1), 1978.

71. M. Dahimene, private communication, March 1985.

72. E. O. Johnson and L. Malter, "A floating double probe method for measurements in gas discharges," Phys. Rev., 80 (1), 1950.

73. R. H. Huddlestone and S. L. Leonard, Plasma Diagnostic Techniques, Academic Press, New York, 1965.

74. H. Sabadil and S. Pfau, "Measurements of the degree of dissociation in oxygen dc discharges," Plasma Chem. and Plasma Process., 5 (1), 1985.

75. T. Roppel, D. K. Reinhard, and J. Asmussen, "Low temperature oxidation of silicon using a microwave plasma disk source," J. Vac. Sci. Technol., B4 (1), 1986.

76. W. A. Pliskin and E. E. Conrad, "Nondestructive determination of the thickness and refractive index of transparent films," IBM J. Res. and Dev., 8, 43-51, 1964.

77. E. R. Skelt and G. M. Howells, "The properties of plasma-grown SiO_2 films," Surf. Sci., 7, 1967.

78. S. M. Sze, Physics of Semiconductor Devices, 2nd. Ed., Wiley and Sons, New York, 1981.

79. J. M. Andrews and M. P. Lepselter, "Reverse current-voltage characteristics of metal-silicide Schottky diodes," Solid State Electronics, 13, 1011-1023, 1970.

80. G. A. Swartz, "Gate oxide integrity of MOS/SOS devices," IEEE Trans. Electron Dev., ED-33 (1), 1986.

81. M. H. White and J. R. Cricchi, "Characterization of thin-oxide MNOS memory transistors," IEEE Trans. Electron Devices, ED-19, 1280, 1972.

82. D. J. Hamilton and W. G. Howard, Basic Integrated Circuit Engineering, McGraw-Hill, New York, 1975.

83. L. A. Glasser and D. W. Dobberpuhl, The Design and Analysis of VLSI Circuits, Addison-Wesley, Reading, 1985.

84. F. P. Fehlner, "Low temperature oxidation of metals and semiconductors," J. Electrochem. Soc., 131 (7), 1984.

APPENDIX

APPENDIX

DETAILS OF THE EXPERIMENTAL APPARATUS AND PROCEDURES

A.1 Overview

This Appendix contains descriptions of the major equipment systems used in the MPDR oxidation and plasma characterization experiments (Section A.2), details of the experimental procedure for the oxidation experiments (Section A.3), and a list of samples (Table A.1).

A.2 Experimental Apparatus

This section describes the equipment, other than the MPDR, used in the oxidation experiments, including the vacuum system, the gas flow control system, the microwave power system, and the measurement instrumentation. The MPDR assembly is discussed in Section 3.2.

A.2.1 Vacuum System

A diagram of the vacuum system and the gas flow system used in the plasma oxidation experiments is provided in Figure A.1. The

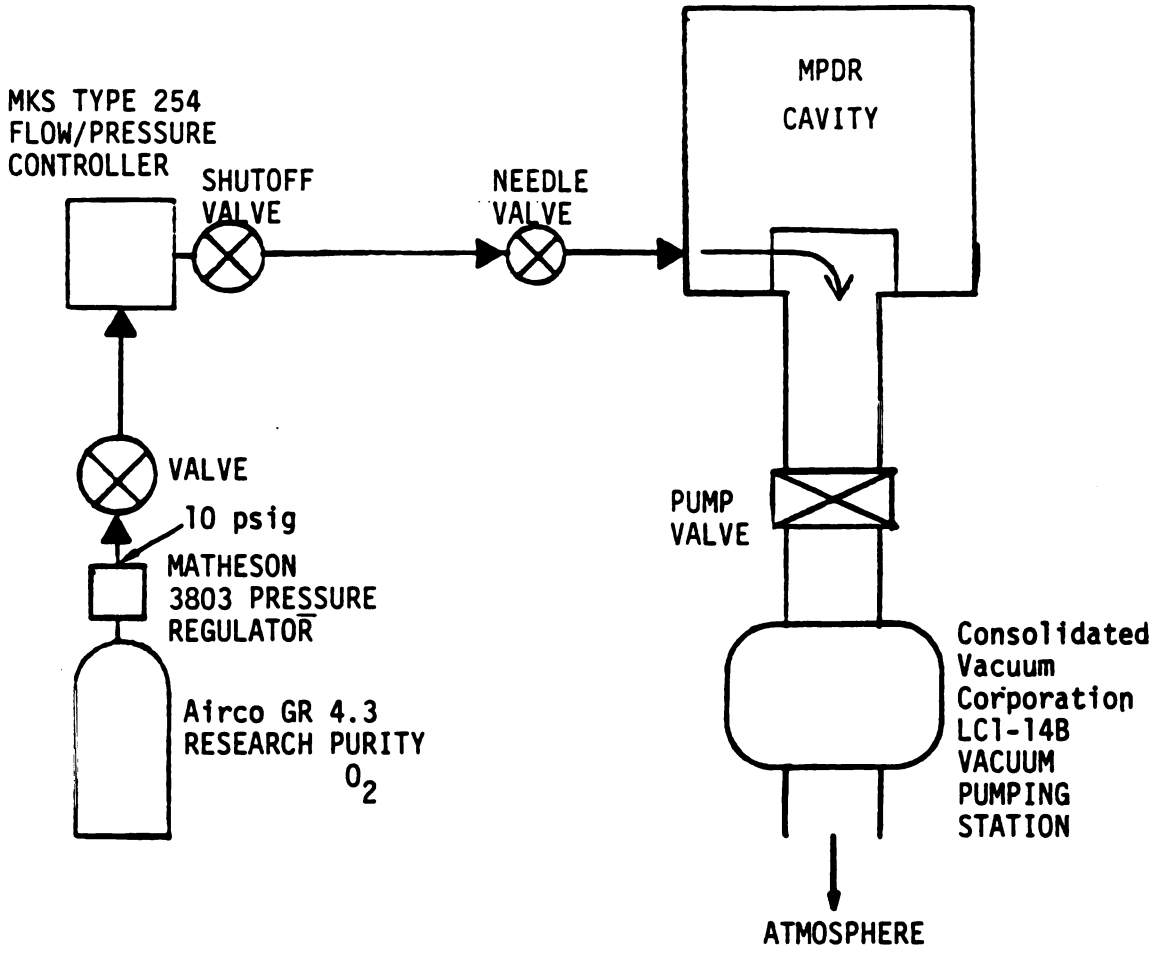

Figure A.1 Gas flow and vacuum systems used in the MPDR oxidation and plasma characterization experiments.

vacuum system was based on a Consolidated Vacuum Corporation Model LC1-14B pumping station, equipped with a 4-inch diffusion pump and a 400 liter/min mechanical pump. The mechanical pump was capable of achieving a base pressure of 10 mTorr. The diffusion pump base pressure was about 5×10^{-3} mTorr. For most of the experiments, only the mechanical pump was used. This pump easily met the flow rate and pressure requirements for the oxidation experiments. The range of pressure was 30 mTorr to 150 mTorr, and the flow rates were less than 100 sccm.

The rest of the vacuum system consisted of a 14 inch diameter, 14 inch tall pyrex cylinder mounted on the stainless steel baseplate of the pumping station, a plexiglass support for the MPDR resting on this cylinder, and the quartz housing and gas feedthrough ring associated with the MPDR. Two low-current electrical feedthroughs were provided to the vacuum system. These were used for biasing the substrate in the oxidation experiments, and for making external connections to a plasma probe in the probe experiments.

A.2.2 Gas Flow System

The purpose of the gas flow system in the oxidation experiments was to control the flow rate of oxygen to the MPDR in order to maintain a constant neutral gas pressure in the discharge chamber. During the course of an experiment, flow adjustments were required due to fluctuations in the pumping speed of the mechanical pump, and due to the effects on the plasma of the varying dc electric field in

the discharge chamber associated with the extraction of anodization current.

A diagram of the oxygen flow system used in the oxidation experiments is shown in Figure A.1. The O_2 source pressure was reduced to working levels by a Matheson Model 3803 two-stage stainless steel regulator. Stainless steel tubing and flexible stainless steel hose were used throughout the flow system to ensure gas purity. The flow control system consisted of an MKS Instruments Type 254 Pressure/Flow Ratio Controller, an MKS Type 251-100 Flow Control Valve, and an MKS Type 256-100 Thermal Mass Flow Transducer. The ouput of the flow controller could be further regulated by a shut-off valve and a needle valve near the MPDR baseplate connection. Flow rate corrected for O_2 was read directly in sccm (standard cubic centimeters per minute) from a digital display on the Type 254 front panel. The maximum flow rate which could be controlled and displayed by this system was 100 sccm. This flow rate resulted in a pressure of 0.2 Torr (measured downstream from the discharge chamber) with the vacuum system operating at maximum pumping speed. However, with all gas input valves fully open, a much higher flow rate was realized; the maximum flow rate resulted in a pressure of about 1 Torr. This high flow rate was used to purge the flow system prior to igniting a discharge, and it was maintained during the ignition process as well since the optimal pressure for igniting an O_2 discharge in this system was found to be between 0.8 Torr and 1 Torr.

A.2.3 Microwave Power System

A diagrams of the microwave power system used in the oxidation experiments is shown in Figure A.2. The microwave power source used for most of these experiments was the Raytheon Model PGM10X1 2.45 GHz source. This source was capable of supplying 100 W indefinitely, and up to 140 W for very short periods of time (<1 min). For oxidation experiments conducted in higher power discharges (up to 140 W) a Holaday Industries Model 2450 source was used.

Output power from the source was directed into either a ferrite isolator or a three-port air-cooled circulator. The purpose of each device was to protect the power source from high levels of reflected power, which might occur during ignition of a discharge in the MPDR, or in case a discharge was unexpectedly extinguished. From the isolator or circulator, power flowed through directional couplers, which allowed a calibrated fraction of both the forward power from the source and the reflected power from the MPDR to be measured by appropriately calibrated power meters. A flexible connection to the movable MPDR power input probe was provided by a 1 m length of high-power, low loss coaxial cable. The transition from flexible coaxial cable to the MPDR power input probe was provided by an Andrews Type 2260B/E507C adaptor. The probe used in the oxidation experiments was designed by J. Root and constructed by the Michigan State University Division of Engineering Research Machine Shop Facility. Further details of the probe assembly and cavity construction are available in the references cited in Section 3.2.

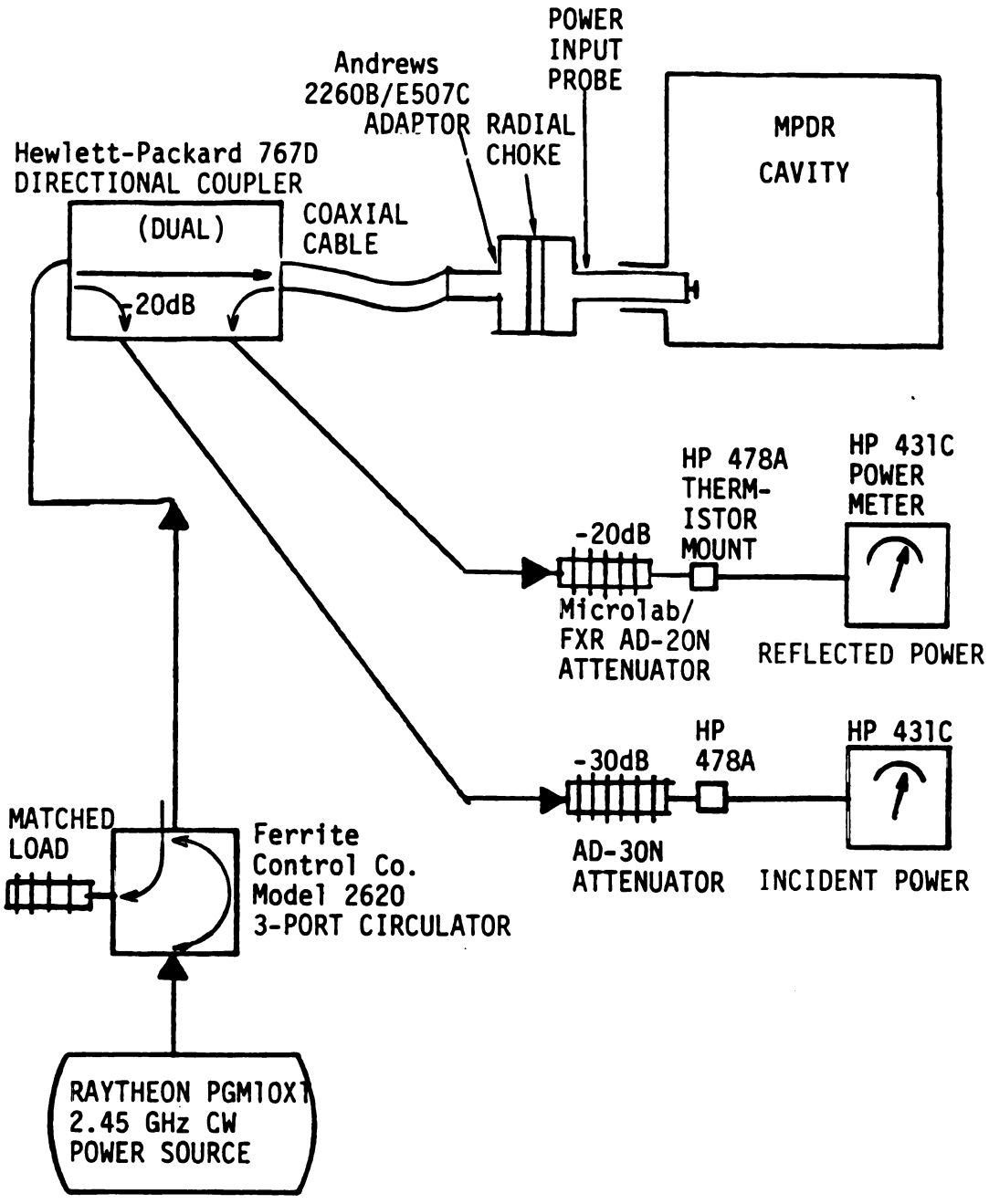

Figure A.2 Microwave power system used in the MPDR oxidation and plasma characterization experiments.

In normal operation with a discharge ignited in the MPDR, the reflected power level measured at the directional coupler could be reduced to nearly zero. This did not mean, however, that the incident power was being coupled entirely into the discharge, as there were losses to the cavity walls and to the coaxial cable. Heating of the coaxial cable to as much as 50 ^{o}C was observed when it was carrying 100 W for 1 h. This heating resulted from the formation of standing waves along the cable and the attendant power loss to the conductors. In addition to losses in the coaxial cable, there were wall losses in the cavity due to joule heating by surface currents, which could amount to more than 15 percent of the total input power. This is discussed further in Section 3.2.

A.2.4 Measurement Equipment

Various instrumentation was used to measure and record incident and reflected microwave power, plasma pressure, bias voltage, and bias current during an oxidation experiment. Data logging was performed using the laboratory computer system: an IBM XT with a DataTranslation 8-channel, 12-bit A/D converter supported by PCLab software. Analog signals proportional to each of the measured quantities were generated by instruments near the experimental set-up, and then transmitted on individual 10 m long coaxial cables to the A/D input board at the computer workstation.

An analog signal proportional to measured microwave power was provided by the DVM or Recorder ouputs on the HP 431C microwave power meters. Substrate bias (anodization) current was measured with a

Hewlett-Packard Model 428B Clip-on dc Milliammeter. This instrument provided a recorder output, but in order to increase the overall resolution of the current measurements, the signal from the recorder output was further amplified by a Keithly Model 610 Electrometer before being transmitted to the A/D input board.

Anodization potential was measured by an electrometer in parallel with the bias circuit, which buffered and attenuated this voltage for input to the A/D board.

Plasma pressure was measured by an MKS Baratron Type 222A capacitance manometer located in the vacuum system below the MPDR baseplate. The manometer had a resolution of 1 mTorr in the range 1 to 10 Torr. The ouput signal from this pressure gauge was displayed and amplified by the Type 254 Pressure/Flow Ratio Controller. The amplified signal was suitable for input to the A/D board. (However, this signal was not used in the experiments reported here since the pressure was maintained at a constant value during each experiment.)

Microwave leakage radiation was measured by a General Microwave Model 481B portable Radiation Hazard Meter (RAHAM), with a resolution of 20 $\mu W/cm^2$. In normal operation, no measurable leakage was detected beyond 2-3 cm from the cavity surface. The most common problem resulting in power leakage was failure of the cavity-sidewall to baseplate seal, and this was usually due to inadequate or uneven tightening of the securing bolts.

A.3 Description of a Typical Oxidation Experiment

A.3.1 Overview

This section provides a detailed description of the oxidation experiments conducted in the MPDR. Topics addressed include sample preparation, sample mounting, start-up and instrument calibration, in-progress monitoring of the experiments, and sample removal, observation, and storage.

A.3.2 Categorization of Samples

Each sample prepared in the oxidation experiments was assigned an identifying label and its history was documented by (i) a manual notebook entry, (ii) a computer-generated listing of the key experimental parameters produced during the oxidation by a BASIC program "OXDATLOG.BAS", and (iii) inclusion in a computerized database, "OXDATA". Samples were labeled sequentially from OX-1 through OX-50. A few experiments were aborted due to difficulties with equipment, instrumentation, or the reactor itself, and in these cases the substrates were labeled and stored in the same way as were good samples, and the source of difficulty was included in the documentation.

Several lists of samples are included in Table A.1(a)-(c). In (a), the samples are listed chronologically, in order of fabrication. In (b), the samples are listed in order of increasing bias voltage,

then increasing pressure. In (c), the samples are listed in order of increasing pressure, then bias, then sample number.

A.3.3 Substrate Preparation and Mounting

In the initial phase of this research, a variety of substrate configurations were considered. The first few substrates processed, labeled Ox-1 through OX-3, were 2 in. diam. Si wafers. Subsequent samples were square pieces of Si, derived from 2 in wafers by scribing and breaking, and were either 19.1 mm × 19.1 mm (OX-4 through OX-10), or 17.8 mm × 17.8 mm (OX-11 through OX-50).

The 2 in Si wafers were manufactured by Monsanto Corporation, and were supplied polished for electronics use on one side. Wafers from this batch were routinely used for MOS device processing in the Michigan State University Integrated Circuits Fabrication Laboratory. The batch specifications provided by the manufacturer are listed below:

Doping: uniform, n-type,
Dopant concentration: 10^{15} to 10^{16} cm^{-3},
Resistivity: 2 to 3 Ω-cm,
Thickness: 11.5 to 12.5 mil (1 mil = 10^{-3} in),
Surface orientation: <100>.

The techniques described below for substrate preparation and mounting were arrived at after several iterations of trial and error. Although they were consistent with the successful preparation of

Table A.1 List of samples fabricated in the MPDR oxidation experiments, sorted (a) chronologically, in order of fabrication, (b) in order of increasing voltage, then increasing pressure, and (c) in order of increasing pressure, then increasing voltage.

The column headings are explained below:

COLUMN HEADING	MEANING
OX	sample number
TOX	oxidation time (in minutes)
PWR	microwave input power (W)
PRESS	oxygen pressure
VB	anodization (bias) voltage (V)
IB0	anodization (bias) current at t=0
IB15	anodization (bias) current at t=15 min
IBF	anodization (bias) current at end of run
DOXCL	oxide thickness determined from color chart
COM	comments

Notes regarding Table A.1:

(1) For samples 1-11, a number of different mounting arrangements were experimented with. In addition, the techniques used for measuring power, pressure, and bias current were not consistent. Therefore, these samples were not used in any of the data discussed in the body of this dissertation.

(2) For samples 18 and above, bias current was recorded as a function of time; values were recorded approximately once per minute.

Table A.1(a) List of Samples fabricated in the MPDR oxidation experiments in chronological order.

OX	TOX	PWR	PRES	VB	IBO	IB15	IBF	DOXCL	COM
1	60	90	150	50	100			0	2-in wafer on pyrex, no mask
2	60	90	100	50	102			700	2-in wafer on pyrex, 1/2-in diam mask opening
3	120	100	75	50	127			1200	2-in wafer, pyrex mask, 1/2-in opening
4	60	100	30	50	152			1000	3/4-in square Si, pyrex mask
5	60	100	30	50	127			1500	3/4-in square, pyrex mask
6	60	100	30	50	64			900	
7	60	100	70	50	152			1500	Below grid 5 cm, with pyrex mask
8	60	100	60	50	152			1500	below grid 15 cm with pyrex mask
9	60	100	60	50	38			1100	above grid, 3/4-in square Si on 2" pyrex, no mask
10	20	250	70	50	152			1000	pyrex mask
11	0								lost bias wire connection
12	105	100	60	50	175.0		60.0	2500	QUARTZ MASK USED 1ST TIME, IV FROM HEATHKIT, PRESS ON MAGNEVAC
13	60	100	70	50	160.0			2000	
14	60	100	70	50	155			2000	FIRST SAMPLE MOUNTED WITH EPOXY. SLIGHTLY ODD SHAPE.
15	60	100	70	35	125.0		50.0	1500	TEMP. OF QUARTZ DISH = 120 C USING RTD THERMOCOUPLE.
16	60	100	70	25	100.0		35.0	1200	
17	60	100	100	50	165.0			2000	LAST OF OLD SILICON. LAST OF HEATHKIT.
18	60	100	150	27		65.0	47.5	1200	
19	60	100	50	36	91.0	66.0	52.0	1100	VB=30 FOR T= 0 TO 20 MIN.
20	60	100	50	30	100.0	62.5	34.6	1000	
21	60	100	40	40	150.0	91.2	37.2	1300	
22	60	100	40	18	52.5	27.0	18.7	500	
23	60	100	40	30	112.0	61.0	30.0	800	
24	60	100	40	46		127.4	33.3	1200	
25	60	100	40	50	136.0	118.6	21.4	1500	VB REDUCED TO 45V AT 43 MIN.
26	60	100	40	35	114.6	69.9	23.0	900	
27	60	100	150	30	62.0	50.2	28.8	700	
28	60	100	100	30	92.4	56.1	23.9	1000	USED TBC-101 FIRST TIME.
29	60	100	30	30	96.2	49.0	18.8	600	
30	60	140	50	40	170.3				LOST BIAS WIRE.
31	60	140	50	30	139.2	68.3	19.7	1050	HOLADAY SOURCE
32	60	120	50	30	132.8	66.6	20.2	900	
33	30	100	50	50	154.2	125.0	100.7	1050	
36	64	100	100	30	110.8	85.4	34.4	1300	
37	52	100	100	30	85	55	21	1000	
38	60	100	150	30	82	60	45	1000	
39	60	100	70	30	94	54	13		
40	60	100	40	30	100	49	24	800	
41	60	100	50	30	104	61	31	1050	
42	60	100	40	40	116	82	39	1250	
43	60	100	50	40	107	98	46	1250	NO GOOD. VACUUM LEAK, MASK SHIFTED.
44	60	100	50	40	154	109	25	1700	
45	36	100	70	40	111	94	56	1200	NO GOOD. VACUUM LEAK.
46	18	100	70	40	155	109	102	1400	BIAS WIRE SHORTED.
47	60	100	70	40	144	110	35	1900	
48	60	100	100	40	128	101	41	1700	DIFFUSION PUMP USED.
49	60	100	150	40	89	89	87	1150	
50	60	100	70	50	151	149	82	2200	

Table A.1(b) List of Samples fabricated in the MPDR oxidation experiments, in order of increasing anodization voltage, then increasing pressure.

OI	TOX	PWR	PRES	VB	IBO	IB15	IBF	DOICL	COM
11	0								lost bias wire connection
22	60	100	40	18	52.5	27.0	18.7	500	
16	60	100	70	25	100.0		35.0	1200	
18	60	100	150	27		65.0	47.5	1200	
29	60	100	30	30	96.2	49.0	18.8	600	
23	60	100	40	30	112.0	61.0	30.0	800	
40	60	100	40	30	100	49	24	800	
20	60	100	50	30	100.0	62.5	34.6	1000	
31	60	140	50	30	159.2	68.3	19.7	1050	HOLADAY SOURCE
32	60	120	50	30	132.8	66.6	20.2	900	
41	60	100	50	30	104	61	31	1050	
39	60	100	70	30	94	54	13		
28	60	100	100	30	92.4	56.1	23.9	1000	USED T6C-101 FIRST TIME.
36	64	100	100	30	110.8	85.4	34.4	1300	
37	52	100	100	30	85	55	21	1000	
27	60	100	150	30	62.0	50.2	28.8	700	
38	60	100	150	30	82	60	45	1000	
26	60	100	40	35	114.6	69.9	23.0	900	
15	60	100	70	35	125.0		50.0	1500	TEMP. OF QUARTZ DISH = 120 C USING RTD THERMOCOUPLE.
19	60	100	50	36	91.0	66.0	52.0	1100	VB=30 FOR T= 0 TO 20 MIN.
21	60	100	40	40	150.0	91.2	37.2	1300	
42	60	100	40	40	116	82	39	1250	
30	60	140	50	40	170.3				LOST BIAS WIRE.
43	60	100	50	40	107	98	46	1250	NO GOOD. VACUUM LEAK, MASK SHIFTED.
44	60	100	50	40	154	109	25	1700	
45	36	100	70	40	111	94	56	1200	NO GOOD. VACUUM LEAK.
46	18	100	70	40	155	109	102	1400	BIAS WIRE SHORTED.
47	60	100	70	40	144	110	35	1900	
48	60	100	100	40	128	101	41	1700	DIFFUSION PUMP USED.
49	60	100	150	40	89	89	87	1150	
24	60	100	40	46		127.4	33.3	1200	
4	60	100	30	50	152			1000	3/4-in square Si, pyrex mask
5	60	100	30	50	127			1500	3/4-in square, pyrex mask
6	60	100	30	50	64			900	
25	60	100	40	50	136.0	118.6	21.4	1500	VB REDUCED TO 45V AT 43 MIN.
33	30	100	50	50	154.2	125.0	100.7	1050	
8	60	100	60	50	152			1500	below grid 15 cm with pyrex mask
9	60	100	60	50	38			1100	above grid, 3/4-in square Si on 2" pyrex, no mask
12	105	100	60	50	175.0		60.0	2500	QUARTZ MASK USED 1ST TIME, IV FROM HEATHKIT, PRESS ON MAGNEVAC
7	60	100	70	50	152			1500	Below grid 5 cm, with pyrex mask
10	20	250	70	50	152			1000	pyrex mask
13	60	100	70	50	160.0			2000	
14	60	100	70	50	155			2000	FIRST SAMPLE MOUNTED WITH EPOXY. SLIGHTLY ODD SHAPE.
50	60	100	70	50	151	149	82	2200	
3	120	100	75	50	127			1200	2-in wafer, pyrex mask, 1/2-in opening
2	60	90	100	50	102			700	2-in wafer on pyrex, 1/2-in diam mask opening
17	60	100	100	50	165.0			2000	LAST OF OLD SILICON. LAST OF HEATHKIT.
1	60	90	150	50	100			0	2-in wafer on pyrex, no mask

Table A.1(c) List of Samples fabricated in the MPDR oxidation experiments, in order of increasing pressure, then increasing anodization voltage.

OI	TOX	PWR	PRES	VB	IBO	IB15	IBF	DOXCL	COM
11	0								lost bias wire connection
29	60	100	30	30	96.2	49.0	18.8	600	
4	60	100	30	50	152			1000	3/4-in square Si, pyrex mask
5	60	100	30	50	127			1500	3/4-in square, pyrex mask
6	60	100	30	50	64			900	
22	60	100	40	18	52.5	27.0	18.7	500	
23	60	100	40	30	112.0	61.0	30.0	800	
40	60	100	40	30	100	49	24	800	
26	60	100	40	35	114.6	69.9	23.0	900	
21	60	100	40	40	150.0	91.2	37.2	1300	
42	60	100	40	40	116	82	39	1250	
24	60	100	40	46		127.4	33.3	1200	
25	60	100	40	50	136.0	118.6	21.4	1500	VB REDUCED TO 45V AT 43 MIN.
20	60	100	50	30	100.0	62.5	34.6	1000	
31	60	140	50	30	159.2	68.3	19.7	1050	HOLADAY SOURCE
32	60	120	50	30	132.8	66.6	20.2	900	
41	60	100	50	30	104	61	31	1050	
19	60	100	50	36	91.0	66.0	52.0	1100	VB=30 FOR T= 0 TO 20 MIN.
30	60	140	50	40	170.3				LOST BIAS WIRE.
43	60	100	50	40	107	98	46	1250	NO GOOD. VACUUM LEAK, MASK SHIFTED.
44	60	100	50	40	154	109	25	1700	
33	30	100	50	50	154.2	125.0	100.7	1050	
8	60	100	60	50	152			1500	below grid 15 cm with pyrex mask
9	60	100	60	50	38			1100	above grid, 3/4-in square Si on 2" pyrex, no mask
12	105	100	60	50	175.0		60.0	2500	QUARTZ MASK USED 1ST TIME, IV FROM HEATHKIT, PRESS ON MAGNEVAC
16	60	100	70	25	100.0		35.0	1200	
39	60	100	70	30	94	54	13		
15	60	100	70	35	125.0		50.0	1500	TEMP. OF QUARTZ DISH = 120 C USING RTD THERMOCOUPLE.
46	18	100	70	40	155	109	102	1400	BIAS WIRE SHORTED.
45	36	100	70	40	111	94	56	1200	NO GOOD. VACUUM LEAK.
47	60	100	70	40	144	110	35	1900	
10	20	250	70	50	152			1000	pyrex mask
13	60	100	70	50	160.0			2000	
14	60	100	70	50	155			2000	FIRST SAMPLE MOUNTED WITH EPOXY. SLIGHTLY ODD SHAPE.
50	60	100	70	50	151	149	82	2200	
7	60	100	70	50	152			1500	Below grid 5 cm, with pyrex mask
3	120	100	75	50	127			1200	2-in wafer, pyrex mask, 1/2-in opening
37	52	100	100	30	85	55	21	1000	
28	60	100	100	30	92.4	56.1	23.9	1000	USED TGC-101 FIRST TIME.
36	64	100	100	30	110.8	85.4	34.4	1300	
48	60	100	100	40	128	101	41	1700	DIFFUSION PUMP USED.
17	60	100	100	50	165.0			2000	LAST OF OLD SILICON. LAST OF HEATHKIT.
2	60	90	100	50	102			700	2-in wafer on pyrex, 1/2-in diam mask opening
18	60	100	150	27		65.0	47.5	1200	
27	60	100	150	30	62.0	50.2	28.8	700	
38	60	100	150	30	82	60	45	1000	
49	60	100	150	40	89	89	87	1150	
1	60	90	150	50	100			0	2-in wafer on pyrex, no mask

oxides in the MPDR, they were not necessarily optimum and therfore they constitute an area for possible improvement in future investigations. A wafer was prepared for use as a substrate by attaching a bias wire to the unpolished (back) side. The bias wire used was Belden 8065, 26 AWG, Heavy Armored Polythermaleze. This wire was selected for its flexibility and small diameter, and for the ability of the insulation to withstand heat. In order to attach the bias wire, the wafer was supported, back side up, on a cleaned quartz plate. The bias wire was cut to length and stripped on both ends, then the end to be connected to the wafer was formed into a small loop, and the wire was bent into position so that the loop rested naturally on the wafer surface. The connection was secured by applying silver epoxy (Epoxy Technology EPO-TEK 415G) to the contact area. The epoxy was built up with two or three applications separated by 3 h, and allowed to dry for 24 h. This technique resulted in a mechanically strong connection which was able to withstand the range of substrate temperatures developed in the oxidation experiments (200-300 ^{o}C).

The only surface preparation performed on the polished (top) surface of a substrate before mounting in the oxidation reactor was a 2 min rinse with deionized distilled water (DI), followed by drying with compressed N_2. The wafer was mounted in the MPDR as shown in Figure 3.1 and Figure 3.2. The substrate was insulated from the grounded baseplate grid by a 1/4-in thick insulating plate of the same shape as the substrate, but having a 1/2-in diameter hole bored vertically through the plate to allow passage of the substrate bias wire. In all of the experiments except OX-1, an identical plate was placed over the substrate to serve as an oxidation mask. For OX-1

through OX-11, plates made of pyrex were used, and for OX-12 through OX-50, plates made of quartz were used. When pyrex was used in the oxygen discharges, heavy deposition was observed on the inside of the discharge region enclosure after each experiment. This deposition ceased when the pyrex was replaced by quartz.

Substrates were mounted in the center of the MPDR discharge region, and for the sake of consistency, square substrates were oriented in the discharge region with an edge perpendicular to the MPDR power input probe.

Care was taken during substrate mounting to avoid contaminating the substrate, the mask, or the interior of the discharge region by contact with sodium-carrying substances. Contact to these pieces was made only with cleaned teflon tweezers, and just prior to installing the quartz housing, the substrate and the surrounding area were sprayed with pressurized N_2 in an attempt to remove larger dust particles. However, since the substrate mounting was performed in un-filtered room air, some degree of surface particulate contamination was unavoidable. (This possibly led to the formation of pinholes through the oxides, as discussed in Section 5.2.3.)

A.3.4 Start-up and Instrument Calibration

After mounting a substrate and installing the quartz discharge housing, the discharge enclosure was evacuated. The base pressure of about 10 mTorr was usually reached within 30 min. During this time, the MPDR cavity shell was bolted into place on the baseplate, cooling water flow to the baseplate was initiated, and the electronic

instrumentation was warmed up and calibrated. To aid in calibration, the data logging computer program provided continuous display of the values actually being recognized on each channel by the computer, so the instrument zero controls could be set to cancel any amplifier offsets or digitizing errors (these were very small, in general). Before each experiment, a trial run of the data logging system was made, using a specially built potentiometer bank as a substitute for the plasma. This potentiometer bank consisted of four 100 Ω, 25 W potentiometers connected in series.

The measurement system was checked for zero accuracy and linearity, and the gain was adjusted on each channel for maximum resolution without overloading.

After the vacuum system reached base pressure, the oxygen supply was initiated and the system was purged with the maximum available flow rate of O_2 (>>100 sccm) for at least 20 min. The pressure measured during this purge was in the range from 800 to 1000 mTorr. During the purge, the MPDR cavity length, L_S, and the probe insertion distance, L_p, (defined in Figure A.3) were adjusted to the values which were determined empirically to provide easiest discharge ignition (these values are listed in Figure A.3. The actual length measured during adjustment was X_s , defined in Figure A.3, and related to L_s by $X_s = L_s - 2.5$ cm.).

A discharge was ignited by alternately increasing the incident microwave power and making tuning adjustments of the cavity length and input probe. A discharge would often ignite at about 80 W incident power with 5 to 10 W reflected power. Discharge ignition was sometimes encouraged by manually pulsing the microwave power output to its maximum value several times, or by applying a Tesla

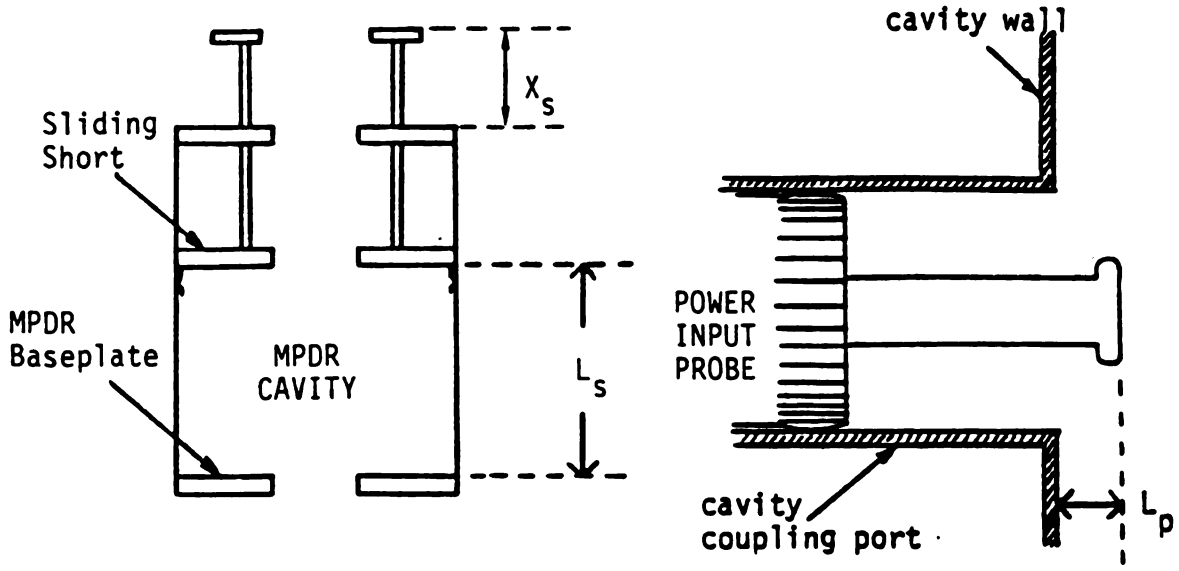

CAVITY MODE	L_s^* (cm)	L_p (cm)
TE_{211}	8.1	0.4
TE_{011}	0.1	3.2
TM_{011}	6.6	-0.1
Discharge Ignition	7.2	0.2

*$X_s = L_s - 2.5$ cm

Figure A.3 The drawings show the definitions of the important tuning dimensions, L_s, L_p, and X_s, in the MPDR. The table gives the values of L_s and L_p which were determined to yield optimal coupling to an oxygen discharge in the MPDR without a substrate installed, with 100 W microwave input power at 100 mTorr pressure.

coil to the outside of the cavity shell. When a discharge ignited, it was generally in the form of a single small lobe clinging to the quartz housing, and in oxygen this lobe was deep red-violet in color. The ignition of a discharge detuned the cavity, so that the measured reflected power increased and was in the range of 40 to 60 W for 80 W input power. In order to establish the desired discharge characteristics, the O_2 flow rate was reduced to the range of study (10-100 sccm) while the cavity length was increased to establish TE_{211}- mode resonance and the incident power was increased to 100 W. The cavity length which was determined experimentally to match the TE_{211}- mode resonance in an unloaded reactor (without a substrate) was L_S = 8.1 cm. This length varied slightly with cavity loading and operating pressure. As the flow rate and pressure decreased, and the cavity approached this resonance, four distinct lobes were established in the discharge, one after another. A convenient reference point for operation was established at 100 W and 100 mTorr. A TE_{211}-mode discharge was established under these conditions, and the entire system was allowed to thermally stabilize for about 5 min. During this time, a microwave radiation detector was used to inspect for power leaks from the MPDR. Several areas were given special attention. These included the cavity shell-to-baseplate connection, the area around the input probe insertion, and the top of the sliding short assembly (where the tuning mechanism was located).

During the reactor warm-up period, some outgassing was usually noticable from the epoxy at the substrate-bias wire connection. Visual evidence for this outgassing took the form of the deposition of dark-colored material on the grid directly below the connection. This deposition was removed after each experiment by polishing the

grid with moistened 600-grit silicon carbide polishing paper, then wiping with methanol followed by deionized distilled water.

A.3.5 In-Progress Monitoring of an Experiment

After a discharge was ignited in the MPDR, about 5 min was allowed for thermal stabilization of all the components. Then data logging was initiated and the substrate bias potential was switched on. The bias potential, bias current, incident microwave power, and reflected power, and time were recorded by a data logging program on the laboratory computer. During the course of an experiment, several aspects of the system required attention. First, it was necessary to make occasional O_2 flow rate adjustments in order to maintain the desired operating pressure. This was particularly true just after the bias was applied because application of the bias caused transient pressure variations in the plasma. Second, it was necessary to make several tuning adjustments during an experiment to optimally match the cavity applicator to the continuously varying load conditions imposed by the oxidizing substrate and the plasma. Finally, as this was an experimental system, it was necessary to be alert to the possibility of unexpected failures. The two types of failures which were most common in the system studied were (i) interruption of the bias circuit due to a failed substrate connection, and (ii) extinguishing of the discharge due to a plasma instability at low pressure or low input power levels.

For a successful run, when the desired oxidation time had elapsed, the substrate bias was switched off, and the plasma was

extinguished by reducing the input power to zero. The system was allowed to cool for about 30 min, then the vacuum was vented and the sample was removed.

After a visual and microscopic inspection to determine oxide color and other general features of interest, the sample was cataloged as described previously, and placed in a sterile plastic petri dish for storage in a vacuum dessicator, pending further analysis (i.e., C-V and I-V characterization).